Vol. 7 No. 1
April 2023

ISSN 2579-5821
e-ISSN 2579-5546

S3
sinta
Science and Technology Index

# Jurnal Geocelebes

Diterbitkan oleh:
Departemen Geofisika
Universitas Hasanuddin
Makassar

JURNAL GEOCELEBES
Geophysics Department | Faculty of Mathematics and Natural Sciences | Hasanuddin University

**Volume 7 Nomor 1, April 2023**

P-ISSN: 2579-5821
E-ISSN: 2579-5546

**Diterbitkan oleh:**
**Departemen Geofisika, FMIPA**
**Universitas Hasanuddin**

JURNAL GEOCELEBES
**Volume 7 Nomor 1, April 2023**

ISSN: 2579 – 5821 (Cetak)
ISSN: 2579 – 5546 (Online)
Alamat URL: http://journal.unhas.ac.id/index.php/geocelebes

Diterbitkan berkala dua kali setahun oleh/ **Published periodically two times annually by** Dept. Geofisika Universitas Hasanuddin/ **Geophysics Dept., Hasanuddin University**

## Dewan Redaksi/ Editor Board



**Sekretariat/ Secretariat**:
Departemen Geofisika, FMIPA Universitas Hasanuddin
Gedung MIPA, Kampus Unhas Tamalanrea - Jalan Perintis Kemerdekaan, Makassar, Sulawesi Selatan, 90245.
*E-mail*: geocelebes@sci.unhas.ac.id

Jurnal Geocelebes adalah jurnal ilmiah yang diterbitkan oleh Departemen Geofisika Universitas Hasanuddin. Jurnal ini diperuntukkan sebagai sarana publikasi ilmiah di bidang geofisika mulai topik teoritik hingga topik topik aplikasi geofisika di berbagai bidang. Artikel yang dimuat merupakan hasil penelitian yang orisinal, tinjauan (*review*) tentang kemajuan terkini dari suatu topik tertentu, studi kasus aplikasi geofisika ataupun resensi tentang perangkat lunak yang berkaitan dengan geofisika. Makalah dapat dikirimkan ke alamat email redaksi dalam bentuk *softcopy* dengan menggunakan template yang telah disediakan. Setiap makalah yang diterima akan ditinjau kelayakannya melalui proses *reviewing* yang ketat oleh Dewan Redaksi.

# DAFTAR ISI

**JURNAL GEOCELEBES**

**Volume 7, Nomor 1, April 2023**

ISSN: 2579 – 5821 (Cetak)
ISSN: 2579 – 5546 (Online)

Alamat URL: http://journal.unhas.ac.id/index.php/geocelebes

# KATA PENGANTAR

Jurnal Geocelebes yang dikelola oleh Departemen Geofisika, Fakultas Matematika dan Ilmu Pengetahuan Alam Universitas Hasanuddin Makassar telah memasuki tahun ke-tujuh. Dewan Redaksi mengucapkan syukur kepada Tuhan Yang Maha Esa atas pencapaian ini serta ungkapan terima kasih atas komitmen Tim Pengelola, Tim Editor Isi dan Layout, dalam menjalankan amanah ini. Secara khusus Dewan Redaksi mengucapkan terima kasih dan penghargaan setinggi-tingginya kepada seluruh penulis yang telah memasukkan karya ilmiahnya dan kepada Tim Mitra Bestari yang telah bersedia meluangkan waktu untuk memberikan saran dan koreksi yang membangun pada setiap artikel di setiap terbitan Jurnal Geocelebes.

Pada edisi Volume 7 Nomor 1 April 2023 terdapat sepuluh artikel. Artikel yang diterbitkan yang secara umum membahas implementasi peran geosains khususnya geofisika dalam ekplorasi sumber daya alam dan bidang lainnya yang sesuai dengan fokus dan cakupan bidang yang diterbitkan oleh Jurnal Geocelebes. Bahasa yang digunakan pada volume ini dan kedepannya adalah Bahasa Inggris yang menunjukkan Jurnal Geocelebes layak menjadi jurnal internasional ke depannya. Jurnal Geocelebes menerima partisipasi dari akademisi, peneliti, praktisi industri, mahasiswa dan lainnya di bidang geosains baik dalam perspektif teoretik maupun aplikasi, baik yang berkaitan tentang bawah permukaan (litosfer) maupun atas permukaan (atmosfer), yang tentunya akan melalui serangkaian proses yaitu *submitting*, *editing*, dan *reviewing*.

Dewan Redaksi Jurnal Geocelebes membuka diri atas saran dan kritikan yang membangun demi perbaikan ke depan. Segala saran dan kritikan dapat dikirimkan melalui email geocelebes@sci.unhas.ac.id

Makassar, April 2023

Dewan Redaksi Jurnal Gecelebes

ISSN: 2579-5821 (Print)
ISSN: 2579-5546 (Online)
URL address: http://journal.unhas.ac.id/index.php/geocelebes
DOI: 10.20956/geocelebes.v7i1.19975

Jurnal Geocelebes Vol. 7 No. 1, April 2023, 1 – 7

# Using Grid Search and Guided Random Search (Simulated Annealing) Methods in Determining the Earthquake Hypocenter in the Majalengka Region, West Java on November 11, 2021

Fachri Aldi Pramudya, Restu Ningsih*, Hayu Nurfaidah, Siska Erna Sephiana, Rahmat Catur Wibowo, Ahmad Zaenudin

Geophysical Engineering Department, Universitas Lampung, Prof. Sumantri Brojonegoro Street, No. 1, Bandar Lampung City, Lampung Province, Indonesia.

*Corresponding author. Email: restu.ningsih100119@students.unila.ac.id

Manuscript received: 8 February 2022; Received in revised form: 27 April 2022; Accepted: 16 August 2022

**Abstract**

Tectonic earthquakes are generally caused by the release of energy produced by a pressure from a moving slab. This study aimed to test the use of grid search methods and guided random search in determining the hypocenter position of the earthquake in the case of the Majalengka regional earthquake, West Java which occurred on November 11, 2021. In this study used earthquake source data with the number of 5 stations, are COCO, KAPI, PALK, MBWA, and NWAO which can be accessed on the IRIS. From the results of determining the earthquake hypocenter using the grid search method, the position of the earthquake hypocenter is obtained with a latitude position of 6.596861°S and for a longitude position of 108.2871°E with a depth of 200 km, while from the processing of the simulated annealing method, the latitude position is 6.501645°S and longitude 108.2252°E with depth of 172.1 km. Meanwhile, if we compare the position of the earthquake hypocenter according to IRIS, are the latitude position of 6.6027°S and for the longitude position of 108.105°E with a depth of 164.41 km, because the hypocenter data from IRIS has been revised by a seismologist so that it is used as a reference, the results that are closest to the position according to IRIS are the results of the simulated annealing method.

**Keywords**: earthquakes; grid search; guided random search; hypocenter; simulated annealing.

**Citation**: Pramudya, F.A., Ningsih, R., Nurfaidah, H., Sephiana, S.E., Wibowo, R.C. and Zaenudin, A. (2023). Using Grid Search and Guided Random Search (Simulated Annealing) Methods in Determining the Earthquake Hypocenter in the Majalengka Region, West Java on November 11, 2021. *Jurnal Geocelebes*, 7(1): 1–7, doi: 10.20956/geocelebes.v7i1.19975.

## Introduction

Indonesia is one of the countries that are prone to natural disasters. This is related to the geographical location of Indonesia, which is located between three large plate tectonics, are the Eurasian Plate, Indo-Australian Plate, and the Pacific Plate; or is also included in the ring of fire area. The movement of three large plates that flank Indonesia, gave significant volcanoes and tectonic activity (Aldiamar, 2007). In general, the tectonic plates in Indonesia are divided into two parts, are the west and the east. The movement of each different plate makes a subduction zone and a transform fault zone. This has an impact on the earthquake disaster which is the most destructive and detrimental natural event in Indonesia (Milson et al., 1992).

West Java is one area that has a high level of seismicity. This condition is caused because the area is a subduction area of the Indo-Australian Plate under the Eurasian Plate and active faults are found in this region. The geological structure that develops in West Java is influenced by the activity of the Indo-Australian Plate which subducts under the Eurasian Plate. The

geological activity of West Java which has been going on for millions of years has produced various types of rocks, both sedimentary rocks, igneous rocks (extrusive and intrusive), and metamorphic rocks with various ages (Hamilton, 1979).

van Bemmelen (1970) divided the western part of Java into several physiographic and structural lines. Majalengka Regency is included in the geological structure of the Bogor Zone which produces an anticlinorium with a west-east direction. In the northern part of the Bogor zone, the geological structure is northward due to pressure from the south (subduction between the Indo-Australian and Eurasian plates). This stress causes folding and faults to appear.

This study uses earthquake data in the Majalengka Regency, West Java with the scope of research being the Majalengka Sub-Basin. In space and time, the research area is limited to Tertiary to Quaternary rocks. The Majalengka sub-basin is part of the back-arc basin which is partly filled with deep-sea sediments.

The occurrence of an earthquake causes a lot of damage which is influenced by several things such as the earthquake magnitude, the characteristics of the ground surface, and ground acceleration. Soft soil layers can cause greater earthquake vibrations compared to harder soil layers when the earthquake waves pass through. This effect is called the amplification of earthquake waves (Solikhin and Suantika, 2008).

The hypocenter is a very important parameter in the seismic field. Based on hypocenter information, it can be estimated that the cause of an earthquake in an area is magma activity or structural activity such as faults. Several methods for determining the hypocenter such as the inversion method and the grid search method (Fauzi, 2010).

Methods of determining earthquake hypocenters have been developed to obtain results rapidly. However, some cases in Indonesia have data processing speed that is inversely proportional to the accuracy of the results obtained (Arimuko et al., 2019).

The use of the grid search method is carried out by calculating each sample point that is formed based on the grid (Grandis and Dahrin, 2014). This method is a development of the neighborhood method. The time required in the calculation, according to the initial parameters in the iteration process. For each grid that has been calculated, the error value will be reviewed. If the new error value is smaller than the previous error value, then the new value is used as the limit. Thus, the calculation will continue until all grids are successfully calculated and will get the smallest RMS (Root Mean Square) value as the best solution (Nurwidyanto and Setiawan, 2011).

This study aims to test the grid search method and guided random search in determining the location of the earthquake hypocenter in the Majalengka area, West Java, in 2021. The calculation is carried out with the help of programming using Matlab software. The results of this study are expected to be a reference in choosing the method of determining the earthquake hypocenter.

## Materials and Methods

This study uses data on the earthquake that occurred on November 11, 2021, in the Majalengka area, West Java. Majalengka Regency is geographically located in the eastern part of West Java Province at 6°32’16.39” S – 7°4’24.75” S and 108°2’30.87” E – 108°24’32.84” E with an area of 1,204.24 $Km^2$. This study uses earthquake source data with a total of 5 stations, are COCO, KAPI, PALK, MBWA, and NWAO (Table 1) which can be accessed on the IRIS page by entering

the date range of occurrence and the desired minimum earthquake magnitude. Earthquake parameters include hypocenter location, origin time of occurrence, region, and magnitude.

**Table 1.** Station Coordinate (sensor).

| Station | Latitude | Longitude | Elevation |
|---|---|---|---|
| COCO | -12.19009° | 96.8348° | 0.001m |
| KAPI | -5.014200° | 119.7517° | 0.3 m |
| PALK | 7.2727999° | 80.7022° | 0.46 m |
| MBWA | -21.15900° | 119.7313° | 0.093 m |
| NWAO | -32.92770° | 117.2389° | 0.2781 m |

*Wadati Diagram*

A simple technique for determining the origin time is the Wadati Diagram. In the Wadati Diagram, the arrival time difference between the P wave and S wave (ts-tp) is plotted against the arrival time of the P wave. The plotting results can determine the origin time by finding the intersect point ts-tp with the x-axis (the arrival time of the P wave). Earthquake time or origin time (OT) was determined using tp and (ts-tp) data from several n stations (Nugraha, 2005).

*Grid Search Method*

The Grid Search method takes time depend on the initial parameters in the iteration process. The Grid Search method is a development of the neighborhood method developed by Sambridge and Gallagher (1993). Each grid that has been calculated will be reviewed for its error value. If the new error value is smaller than the previous value, the new value becomes the limit value. This calculation continues until all grids are successfully calculated and the smallest RMS (Root Mean Square) value will be obtained as the best solution (Rodi and Toksoz, 2000).

In the Grid Search method, each sample point is calculated based on a grid (Grandis, 2009). The Grid Search method requires time which is related to the initial parameters in the iteration process. The wide range used starts from the widest area which will then be narrowed after knowing the wide range that has the smallest error value from the previous calculation. The calculation will continue until the value of the wide range or area limit which has the smallest RMS (Root Mean Square) value is known which is the best solution. It should be noted that when determining a large evaluation step parameter, the RMS (Root Mean Square) value used is too small. The results obtained from this method will be more accurate if the grid is made more tightly but the calculation will take longer.

*Guided Random Search Method*

Each inversion method has its own advantages and disadvantages. The hypocenter solution could be stuck at the local minimum because the initial model is not good. Another inversion method, simulated annealing, can be applied to the global optimization case. Unlike local optimization methods such as iterative least squares, the convergence of the simulated annealing method does not depend on the initial model.

One of the Guided Random Search methods is the Simulated Annealing (SA) method. The Simulated Annealing method (Grandis, 2009) based on the thermodynamic substance crystallization process. At high temperatures a solid substance melts, then the cooling process slowly causes the formation of crystals associated with the minimum system energy.

In this Simulated Annealing process, the model space must be defined first by determining "a priori" the minimum and maximum value intervals for the model parameters. In this study, the model parameter is the earthquake hypocenter. The selection of model parameter values is determined randomly as an arbitrary number in the interval of maximum and minimum values, respectively. The procedure is to take a random number R with a uniform probability between 0 and 1

which is mapped into the model parameter values.

The model perturbation probability is expressed by:

$$P(\Delta E) = \exp\left(-\frac{\Delta E}{T}\right) \quad (1)$$

where ΔE is the change in the objective function or the change in misfit due to the model perturbation. If ΔE<0, then the model change is accepted. However, if ΔE≥0, then the determination is determined probabilistically using a random number R which is uniformly distributed in the interval [0.1]. If R<P(ΔE) then the change is accepted, otherwise if R≥P(ΔE) the change is rejected and returns to the previous one. The iteration process starts with a high enough temperature so that almost all perturbation models are accepted. When the temperature drops slowly, the perturbation of the accepted model will decrease if ΔE≥0.

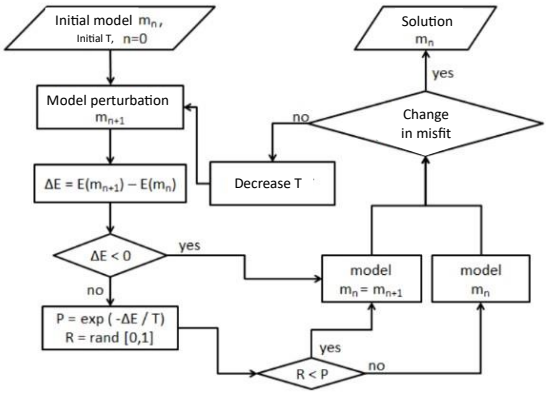


**Figure 1.** Flowchart of the Simulated Annealing inversion method for hypocenter location determination (Ry and Nugraha, 2012).

One of the parameters that shows the solution of the global minimum is the smallest Root Mean Square (RMS) value. RMS does not get the best solution if the initial parameters used are not appropriate so that it is stuck at the local minimum value (Ratchkovsky et al., 1998). One way to avoid local minimum values is to make maximum use of the available "a priori" information to determine the initial parameter model (Grandis, 2009).

The calculations used to test the two methods are the Grid Search method and the Guided Random Search method (Simulated Annealing Method) using the Matlab programming language. The calculation is done by inputting data on the hypocenter location, velocity model, travel time, and station location.

## Result and Discussion

In determining the earthquake hypocenter, first picking the arrival time value of the P wave and S wave respectively at each station that is sampled using SeisGram software. So that from the results of the picking, the parameters needed to determine the origin time are the values of Tp, Ts and the difference between Ts and Tp.

**Table 2.** Ts-Tp data of research earthquake stations.

| Station | Tp | Ts | Ts-Tp |
|---|---|---|---|
| COCO | 18:22:15 | 18:24:34 | 138.5s |
| KAPI | 18:22 :06 | 18:24 :16 | 129.6s |
| PALK | 18:25: 23 | 18:30: 14 | 290.9s |
| MBWA | 18:23: 27 | 18:26: 49 | 201.4s |
| NWAO | 18:24: 57 | 18:29: 26 | 269.7s |

Then determine T0 at 18:22:00 because this time is a round number close to the time of arrival, the goal is to simplify the calculation. Also calculate the value of Tobs, with the value of Tobs can be calculated by subtracting the value of T0 from Tp as in Table 3.

Determination of origin time using the Wadati Diagram, plotting the Tp parameter (x-axis) against Ts-Tp (y-axis) as in Figure 2.

**Table 3.** Tobs value calculation.

| Station | Tp | T0 | Tobs |
|---|---|---|---|
| COCO | 18:22:15 | 18:22:00 | 15.931s |
| KAPI | 18:22 :06 | 18:22:00 | 6.375s |
| PALK | 18:25: 23 | 18:22:00 | 203.088s |
| MBWA | 18:23: 27 | 18:22:00 | 87.671s |
| NWAO | 18:24: 57 | 18:22:00 | 177.123s |

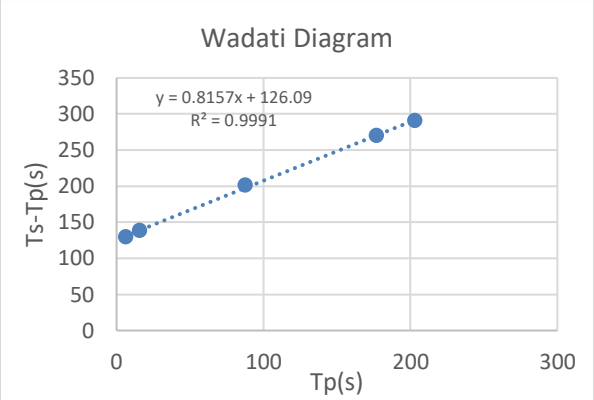


**Figure 2.** Wadati Diagram to determine the origin time value.

The diagram above shows the trendline equation y = 0.8157x+126.09 with an accuracy of 0.9991 (R^2 value). For the determination of the origin time value, the equation is considered equal to zero or the point of the earthquake occurrence is considered equal to zero. Thus, the result of parameter x is equal to -154.579. To get the value of origin time, by adding the value of T0 to x as in Equation (1). And the resulting Origin time value is 18:19:25.421.

$$\text{Origin Time} = T0 + x \quad (2)$$

Then, because the origin time result obtained from the above equation is below the arrival time (Tp), the T0 value is determined at 18:19:00. With known data as well, is in Table 4.

**Table 4.** Origin time calculation results.

| x | y | z | T0 (s) | Tobs |
|---|---|---|---|---|
| 264424 | 8651485 | 1 | | 195.9s |
| 259937 | 9445369 | 300 | | 186.3s |
| 467127 | 803916 | 460 | 25.421 | 383.08s |
| 783639 | 7657816 | 190 | | 267.67s |
| 522344 | 6356702 | 380 | | 357.12s |

Then from these results, the calculation of the hypocenter position using the Grid Search method can be seen in Figure 3. Calculation of the hypocenter position using the Simulated Annealing method can be seen in Figure 4.

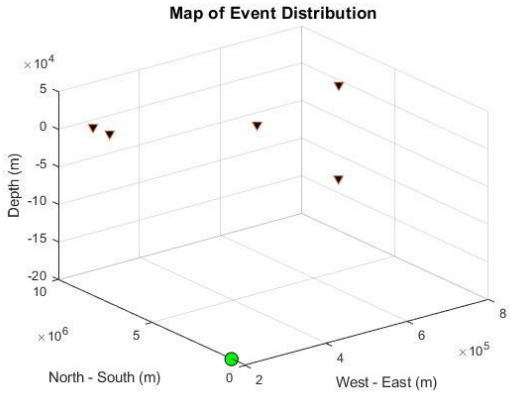


**Figure 3.** Earthquake hypocenter position using the Grid Search method.

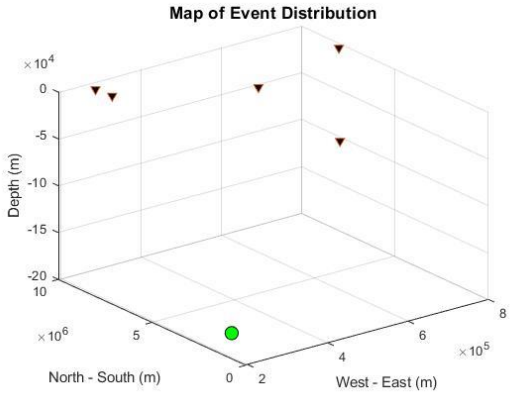


**Figure 4.** Earthquake hypocenter position using the Simulated Annealing method.

The calculation results using both methods are the best results with the smallest RMS value of each method. The results are not too different which can be seen in Table 5.

**Table 5.** Comparison of the hypocenter position of the Grid Search and Simulated Annealing methods.

| Coordinate | | Grid Search | Simulated Annealing |
|---|---|---|---|
| UTM | X | 200000 | 193100 |
| | Y | 730000 | 719500 |
| | Z | -200,000 | -172,100 |
| Lat/Long. | X | 6.596861°S | 6.501645°S |
| | Y | 108.2871°E | 108.2252°E |
| | Z | -200,000 | -172,100 |

Table 5 shows the results of hypocenter calculations using the grid search and simulated annealing methods from a earthquake event using 5 stations. From the results of determining the hypocenter using the grid search method, the position of the earthquake hypocenter was obtained with a latitude of 6.596861° S and a longitude of

108.2871° E with a depth of 200,000 m. Then for the position of the hypocenter from the processing results with the simulated annealing method, the position of latitude 6.501645° S and longitude 108.2252° E with a depth of 172,100 m was obtained. Meanwhile, when compared with the position of the hypocenter according to IRIS, the position of latitude 6.6027° S and longitude 108.105° E with a depth of 164,410 m. The closest result to the position of the IRIS is the result of the Simulated Annealing method. However, these results need to be developed again so that the data becomes better and there is no considerable difference.

## Conclusion

In determining the hypocenter, picking is done first to get the parameters needed to determine the origin time, are the value of Tp, Ts and also the difference between Ts and Tp. The calculation of the hypocenter position in this study uses the Grid Search method and the Simulated Annealing method. The results of the Grid Search method obtained the hypocenter position of the earthquake with a latitude position of 6.59686° S and for the longitude position of 108.287° E with a depth of 200,000 m. Then for the hypocenter position from the processing results with the Simulated Annealing method, the latitude position of 6.501645° S and longitude position of 108.2252° E with a depth of 172,100 m were obtained. The position of the earthquake hypocenter according to IRIS is the position of latitude 6.6027° S nd for the position of longitude 108.105° E with a depth of 164,410 m. The most accurate results or close to the position of the earthquake from IRIS are the results of the simulated annealing method. However, these results need to be developed again so that the data becomes better and there is no considerable difference.

## Acknowledgments

The author would like to thank all those who have helped in carrying out this writing so that it can be completed properly.

## Author Contribution

In compiling this research journal, each writer is divided into several job indexes. For collection of library sources by Restu Ningsih, data processing by Fachri Aldi Pramudya, and drafting of the journal by Siska Erna Sephiana and Hayu Nurfaidah. As for the observers and mentors in the preparation of this journal is Rahmat Catur Wibowo and Ahmad Zaenudin.

## Conflict of Interest

In this study there is no financial or personal relationship between the author and the organization and others so that the results of this study can be "accounted for" by the author.

## References

Aldiamar, F. (2007). *Analisa Resiko Gempa dan Pembuatan Respon Spektra Desain untuk Jembatan Suramadu dengan Permodelan Sumber Gempa 3D.* Master thesis, Institut Teknologi Bandung.

Arimuko, A., Persada, Y. D., & Subakti, H. (2019). Model Kecepatan 1 - D Gelombang P dan Gelombang S dari Data Hasil Relokasi Hiposenter di Wilayah Gunung Sinabung. *Jurnal Meteorologi Klimatologi dan Geofisika*, 5(3), 72–79. https://doi.org/10.36754/jmkg.v5i3.77

Fauzi. (2010). *Analisis Data Seismogram untuk Menentukan Parameter Magnitude Gempabumi.* Bachelor thesis. Universitas Islam Negeri Syarif Hidayatullah.

Grandis, H. (2009). *Pengantar Pemodelan Inversi.* Himpunan Ahli Geofisika

Indonesia. Jakarta 12540, Indonesia.

Grandis, H., & Dahrin, D. (2014). Constrain Two - Dimensional Inversion of Gravity. *Journal of Mathematical and Fundamental Sciences*, 46(1), 1–13. https://doi.org/10.5614/j.math.fund.sci.2014.46.1.1

Hamilton, W. (1979). *Tectonics of the Indonesian Region.* Geol. Surv. Proff. Paper 1078, US Government. Printing Office. Washington, p.114-156.

Milsom, J., Masson, D., Nichols, G., Sikumbang, N., Dwiyanto, B., Parson, L., & Kallagher, H. (1992). The Manokwari Trough and The Western End of The New Guinea Trench. *Tectonics*, 11(1), 145–153. https://doi.org/10.1029/91TC01257

Nugraha, A.D. (2005). *Studi Tomografi 3-D Non Linear untuk Gunung Guntur dengan Menggunakan Waktu Tiba Gelombang P dan S*. Master thesis, Institut Teknologi Bandung.

Nurwidyanto, I.M., & Setiawan, A. (2011). Inversi linier least square dengan Matlab (Studi Kasus Model Gravitasi Bola Berlapis). *Jurnal Berkala Fisika*, 14(3), 93–100. https://ejournal.undip.ac.id/index.php/berkala_fisika/article/view/5009

Ratchkovsky, N.A., Pujol J., & Biswas, N. N. (1998). Relocation of shallow earthquakes in southern Alaska using Joint Hypocenter Determination method. *Journal of Seismology*. 2(1), 87–102. https://doi.org/10.1023/A:1009758721717

Rodi, W., & Toksoz, M. N. (2000). Grid Search Techniques for Seismic Event Location. *Proceedings of the 22nd Annual DoD/DOE Seismic Research Symposium*.

Ry, R. V., & Nugraha, A. D. (2012). Penentuan Hiposenter Gempa Mikro Menggunakan Metode Inversi Simulated Annealing pada Lapangan Geotermal "RR". *Jurnal Geofisika*, 13(1), 23–31.

Sambridge, M., & Gallagher, K. (1993). Earthquake Hypocenter Location Using Genetic Algorithms. *Bulletin Seismological Society of America*, 83(5), 1467–1491. https://doi.org/10.1785/BSSA0830051467

Solikhin, A., & Suantika, G. (2008). *Laporan Penyelidikan Gempabumi Daerah Kabupaten Bandung dan Sekitarnya Jawa Barat.* Pusat Vulkanologi dan Mitigasi Bencana Geologi. Bandung.

van Bemmelen. (1970). *The Geology of Indonesia*, 2nd ed, Netherlands: Hague.

ISSN: 2579-5821 (Print)
ISSN: 2579-5546 (Online)
URL address: http://journal.unhas.ac.id/index.php/geocelebes
DOI: 10.20956/geocelebes.v7i1.20524

Jurnal Geocelebes Vol. 7 No. 1, April 2023, 8 – 16

# Application of Self-Potential Method in Mapping Leachate Flow Around Rasau Jaya Landfills, Kubu Raya Regency

Kaharudin, Yudha Arman, Muhardi*

Department of Geophysics, Universitas Tanjungpura, Pontianak, Indonesia

*Corresponding author. Email: muhardi@physics.untan.ac.id

Manuscript received: 27 March 2022; Received in revised form: 14 July 2022; Accepted: 14 September 2022

**Abstract**

This study uses the self-potential method to map the leachate flow around the Rasau Jaya landfill, Sungai Raya District, Kubu Raya Regency. The study was carried out in 2 areas, the north and south of the landfill. Data acquisition using a fixed base configuration by applying ten lines. Each line has a length of 105 m with 5 m, and the distance between the porous pots is 5 m. The measurement results show that the potential value distribution at the first location is -19.62 mV to 8.44 mV, and the potential value at the second location is -55.50 mV to 23.26 mV. The interpretation shows that leachate accumulation from the landfill in the first area has a potential value of -19.62 mV to -13 mV. The second location has a potential value of -55.50 mV to -36 mV. Based on isopotential contour maps, leachate accumulation in the first location is thought to be in the north to northeast of the landfill, while in the second location, it is thought to be in the southwest to the west of the landfill.

**Keywords**: leachate; self potential; landfill; Rasau Jaya.

**Citation**: Kaharuddin., Arman, Y. and Muhardi. (2023). Application of Self Potential Method in Mapping Leachate Flow around Rasau Jaya Landfills Kubu Raya Regency. *Jurnal Geocelebes*, 7(1), 8–16, doi: 10.20956/geocelebes.v7i1.20524

## Introduction

The existence of landfills will cause problems for the surrounding environment, such as the distribution of waste and leachate. Leachate comes from rainwater that seeps into the waste pile to transport dissolved materials from the waste decomposition process. Leachate spreading is the main problem caused by waste piles in landfills because it can potentially contain heavy metals that can harm the environment. If the treatment is not maximized, leachate can contaminate the groundwater used by the community. (Hartini and Yulianto, 2018). Rasau Jaya District has peatlands with an area of 51,391 ha (Krisnohadi, 2011). Leachate flow will easily seep below the peat soil's surface so that it can contaminate groundwater.

Rasau Jaya landfill is located on peatland, and its waste management applies an open dumping system. Peatlands will quickly absorb water into the soil (Muliadi et al., 2019). In rainy conditions, the leachate discharge into the treatment plant is predicted to be more significant. The infiltration process of rainwater mixed with leachate will quickly seep into the soil. Leachate seepage is highly dependent on the physical properties of the ground, especially porosity and permeability. Peat soils have high porosity and permeability, making them water-saturated soils (Sampurno et al., 2018).

One of the geoelectric surveys that can be used to observe leachate distribution is the self-potential (SP) method. The SP method is a passive geophysical because it utilizes natural electric potential. One of the causes of electric potential at the surface is water

seepage underground (Thanh et al., 2020). The natural electrical potential of the earth is caused by electrokinetic, diffusion, and mineralization processes. This method is effectively used for shallow exploration activities or no more than 100 m (Telford et al., 1990). This method is also often used in environmental studies (Soupios and Karaoulis, 2015), such as detecting fluid flow (Vaidila et al., 2015), identifying groundwater flow (Muhardi et al., 2021), identifying subsurface hot fluid flow (Pratama et al., 2017), leachate distribution mapping (Handoko et al., 2016), and identifying contaminant fluid flow distribution (Bavitra, 2018).

This research aims to map the leachate flow around the Rasau Jaya landfill using the SP method. This method can detect anomalous self-potential values originating from subsurface fluid flow indicated by positive or negative values of less than 100 mV (Telford et al., 1990). Groundwater utilized by some residents around the landfill is potentially contaminated by leachate seepage. Identification of leachate flow can provide initial information for the community and village government to anticipate the impact of leachate on the environment.

## Research Method

The measurement was carried out in 2 locations around the Rasau Jaya Landfill, Sultan Agung Street, Kuala Dua Village, Sungai Raya Sub-district, Kubu Raya Regency, West Kalimantan. The first location is north of the landfill (residential area), while the second is south of the landfill, as shown in Figure 1. Data collection was carried out with as many as five passes at each research location. The track length was 105 m, the distance between tracks was 5 m, and the space between porous pots was 5 m. Thus, potential data was obtained with a grid of 105 m. Thus, the data was obtained with a 5 m x 5 m grid, and the area at each location was 3,300 $m^2$.

The use of porous pot electrodes in SP method measurements is to avoid polarization effects (Siswoyo, 2018). In this study, the electrodes were made using a 1.5-inch paralon with a height of 20 cm. The porous medium used as a base is made of wood with a thickness of 3 cm. The connectors used were copper wires. Copper sulfate (CuSO4) solution was used to increase the sensitivity of the porous pot electrode (Prasetya et al., 2022). An illustration of the porous pot scheme can be seen in Figure 2.

Measurement of potential values in the field using a digital multimeter. The electrode installation applied a fixed base configuration. One electrode was placed at the reference point (base), and the other electrode moved along the measurement path (rover). The electrodes were installed in the ground to a depth of 30-50 cm. Data collection in the field is done by two methods, namely, based on the time function and position function. An illustration of natural potential measurement in fixed base configuration can be seen in Figure 3.

The mapping of leachate flow is based on subsurface water flow, which is relatively shallow. The distribution of potential values shown by the isopotential contour map will be a reference in identifying leachate flow because leachate flows by the flow of subsurface water, from high to low potential. Meanwhile, the presence of leachate is determined by relatively small and negative potential values because leachate is conductive. After all, it contains metal minerals.


**Figure 1.** Research design map.

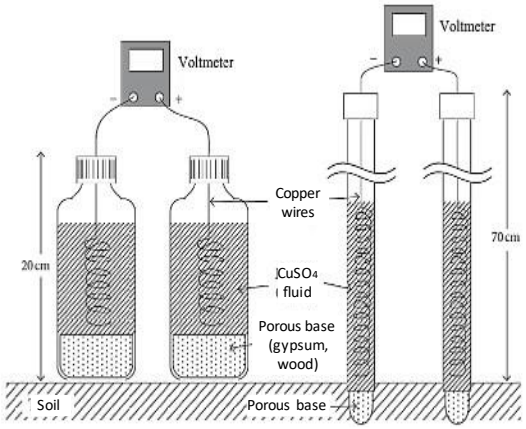


**Figure 2.** Porous pot scheme illustration (Goto et al., 2012).

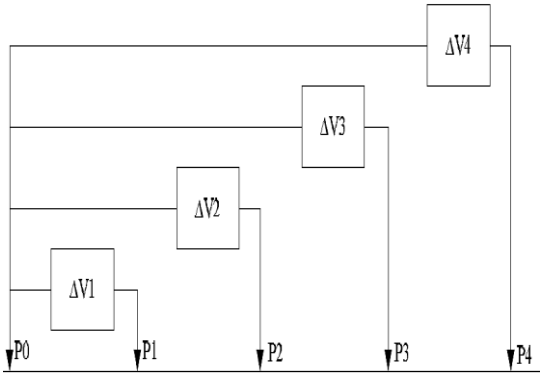


**Figure 3.** Illustration of fixed base configuration (Indriana et al., 2007).

## Result and Discussion

*The First Location*

The distribution of natural potential values at the first location is shown in Figure 4. The values obtained vary from negative to positive, which have -19.62 mV to 8.44 mV. The change in potential value with distance on the five lines does not show a regular pattern. However, lines 1 and 2 generally have more negative values than the other lines, especially in the middle of the line. This is because the first location is in a residential area, so this value is strongly influenced by the activities of residents, especially in water utilization.

The isopotential contour map at the first location was obtained by combining the five lines, as shown in Figure 5. The lower potential values are in the center and the southwest, while the higher values are in the center to the northeast. The potential distribution pattern is thought to be caused by the distribution of leachate from the landfill and community household activities, as this location is in a residential area.

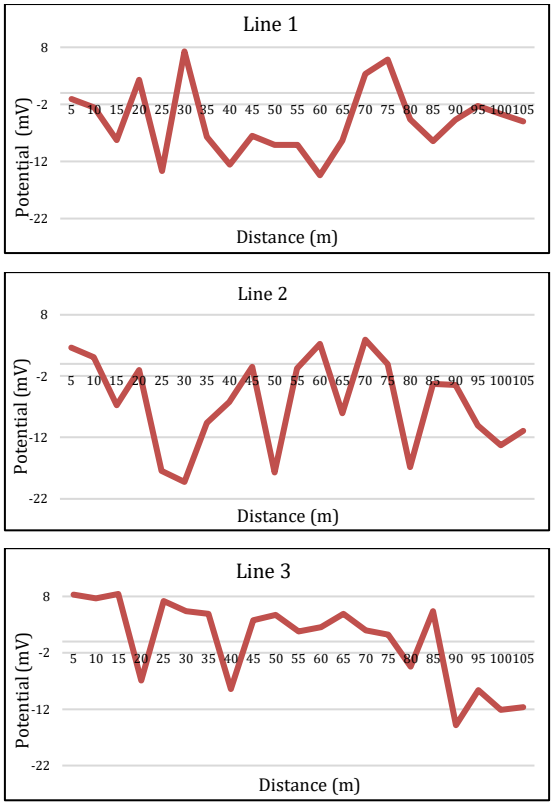


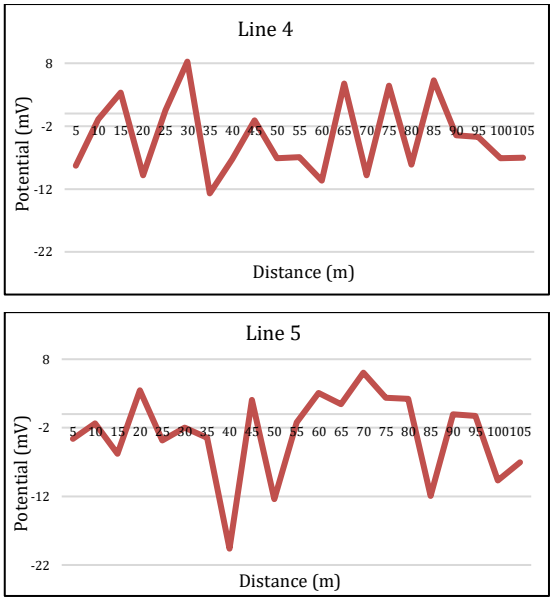


**Figure 4.** Graph of self-potential values on each line of the first location.

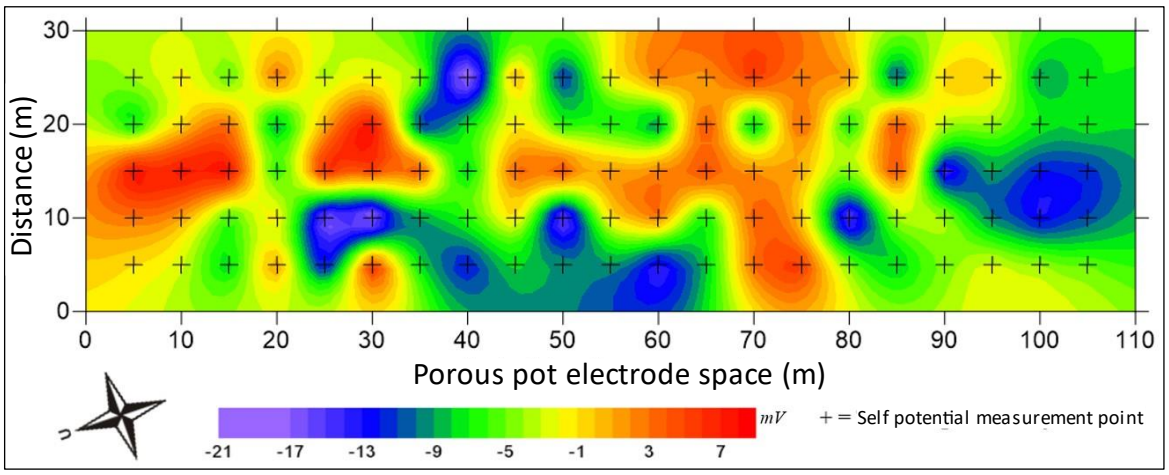


**Figure 5.** Isopotential contour map of the first location.

*The Second Location*

The distribution of natural potential values at the second location is shown in Figure 6. The values obtained vary from negative to positive, which have -55.5 mV to 23.26 mV. In general, there is a decrease in potential value as the distance from the reference point increases. This result shows that the closer to the landfill, the smaller the potential value obtained. The five lines' small and negative potential values are generally located at a distance of 10 - 15 m from the reference point or 90 - 95 m from the landfill. In general, the distribution of potential values in the five lines is negative, with almost the same pattern.

The isopotential contour map at the second location was obtained by combining the five lines, as shown in Figure 7. The lower potential values are located in the northeast, while the higher values are located in the southwest. The potential distribution

pattern is caused by leachate distribution from the landfill.

The natural potential anomalies displayed at the first and second locations are thought to be due to the accumulation of fluid flow below the ground surface. The flow is thought to originate from conductive material mixed with near-surface groundwater and leachate from waste. The fluid flow mechanism is also due to the influence of gravity, as it is in the direction of the topographic slope of the study site. At higher topography, the potential value tends to be greater than at lower topography. The nature of the fluid flows from a high place to a lower place.

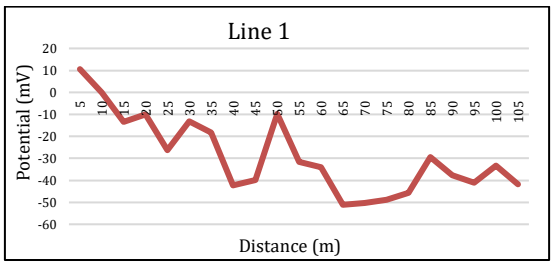


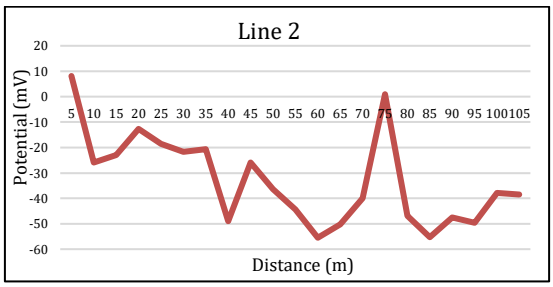


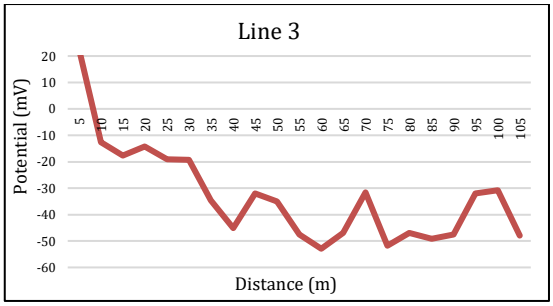


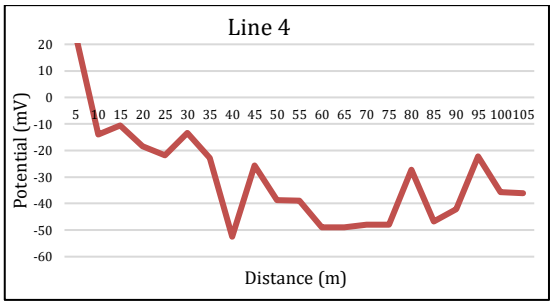



**Figure 6.** Graph of potential values at each line of the second location.

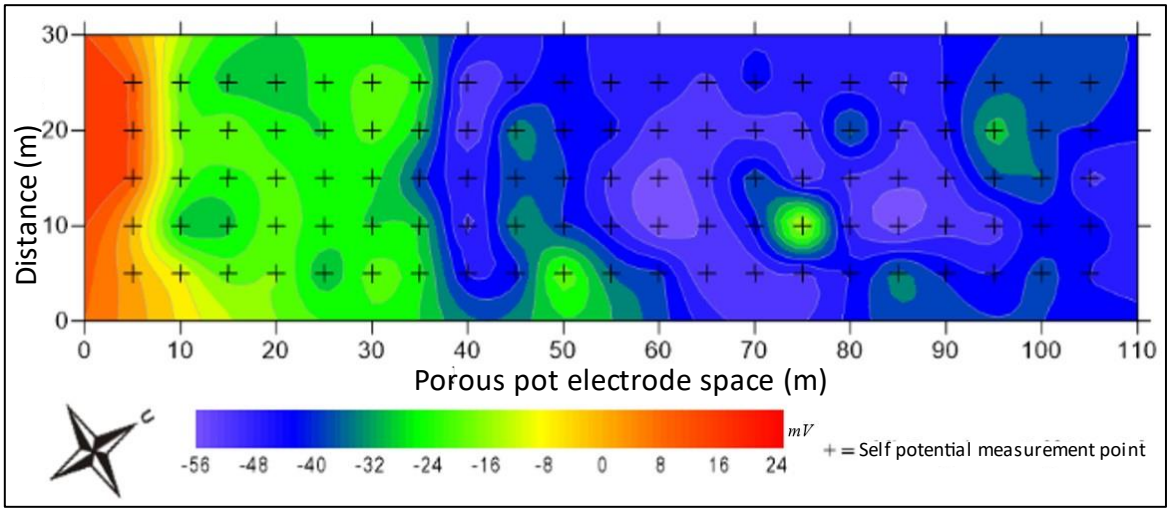


**Figure 7.** Isopotential contour map of the second location.

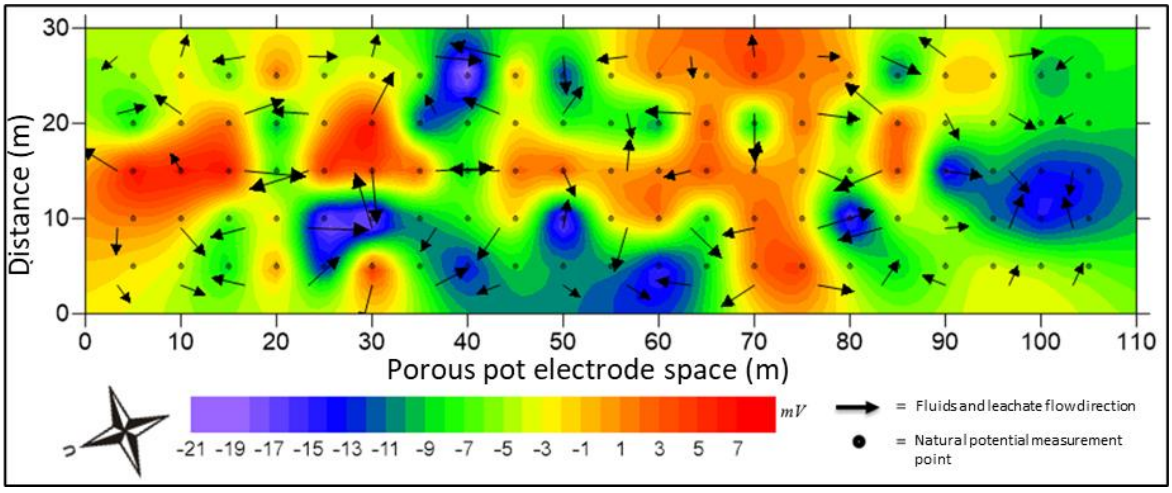


(a)

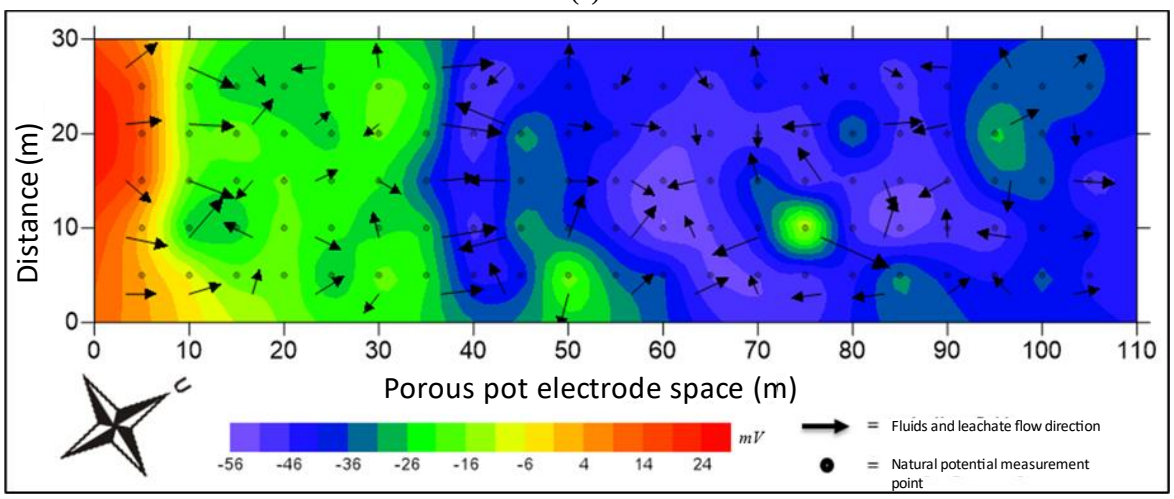


(b)

**Figure 8.** Isopotential and leachate flow contour maps; (a) first location, (b) second location.

The isopotential map and leachate flow direction at the research location can be seen in Figure 8. The qualitative interpretation shows that a black arrow indicates the direction of fluid and leachate flow with a direction perpendicular to the equipotential plane (Rosid et al., 2012). This flow direction results from the difference in potential values as the fluid moves from high potential to low potential. Lower potential values are interpreted as groundwater that is thought to have been contaminated by leachate. Leachate has a relatively lower potential value because it contains metal minerals, so the resistivity value and potential value of leachate become very small. The negative potential value in the measurement area is suspected to be leachate. Leachate flow generally originates from rainwater seepage on waste piles which then spreads to the area around the landfill. The interpretation results show that leachate accumulation from the landfill in the first location has a potential value of -19.62 mV to -13 mV, and in the second location, has a potential value of -55.50 mV to -36 mV.

Fluid flow is affected by electrochemical potential and electrokinetic potential. The movement of electrolytes in leachate water is expected to cause electrochemical potential. The potential value in the leachate area is more negative than in the area that is not contaminated by leachate. Background potentials create electro-chemical processes in the leachate stream so that it can cause anomalous potential values at the identified research location to be more negative. The influence of

electrokinetic potential shows that the accumulation of negative values tends to be at a lower topography. It is due to the nature of fluid flow that flows from a higher place to a lower place.

The natural potential values at the first and second research locations differ significantly. In the first location, the distribution of potential values is more varied, allegedly due to activities in residential areas and the slope of the land tends towards the landfill. In the second location, the distribution of potential values is more negative, up to -55.5 mV, presumably due to the influence of leachate water flow caused by the slope of the land and by the flow of ditches originating from the landfill (Bavitra, 2018).

Fluid flow is also closely related to the topographic conditions of the research location. The landfill with a pile of garbage is at a lower elevation than the surrounding area. It is because the load coming from the pile of waste at the landfill location will cause a decrease in the ground surface. The fluid flow tends to follow the slope direction with a lower elevation due to the influence of gravity. This condition will affect the direction of leachate flow at the research location. When it rains, the leachate that is carried away will flow in the direction of the land slope. It causes leachate to be carried away and collected at locations with lower elevations. The measured potential value is dominantly lower at points with lower elevation. It is due to the influence of leachate transported by the fluid flow in the second location. The fluid flow direction around the residential area in the first location was identified as flowing toward the landfill area.

## Conclusion

The distribution of potential values at the first location is -19.62 mV to 8.44 mV, and the potential value at the second location is -55.50 mV to 23.26 mV. The interpretation results show that the accumulation of leachate from the landfill in the first location has a potential value of -19.62 mV to -13 mV, and in the second location has a value of -55.50 mV to -36 mV. Based on the isopotential contour map, leachate accumulation in the first location is thought to be in the north to northeast part of the landfill, while in the second location, it is thought to be in the southwest to the west part of the landfill.

## Acknowledgements

The authors would like to thank the Laboratory of Geophysics and Geographic Information System (GIS), Universitas Tanjungpura, for facilitating the self-potential equipment in this research.

## Author Contribution

Each author has a job in completing this research. Collection of references, data acquisition in the field, and data processing were carried out by Kaharudin. As for interpreting the results and discussion mentored by Yudha Arman and Muhardi. All authors reviewed this manuscript.

## Conflict of Interest

In this research, all authors have no financial or personal relationships with other people or organizations, so the author can account for the research results.

## References

Bavitra. (2018). Interpretasi Sebaran Aliran Fluida Kontaminan Menggunakan Metode Self-Potential (SP) Pada Tempat Pembuangan Akhir (TPA) Sampah Sarimukti, Kabupaten Bandung Barat. In *Institut Teknologi Bandung*.

Goto, T. N., Kondo, K., Ito, R., Esaki, K., Oouchi, Y., Abe, Y., & Tsujimura, M. (2012). Implications of Self-Potential Distribution for Groundwater Flow System in a Nonvolcanic Mountain

Slope. *International Journal of Geophysics*, 1–10. https://doi.org/10.1155/2012/640250

Handoko, A. W., Darsono, & Darmanto. (2016). Aplikasi Metode Self Potential untuk Pemetaan Sebaran Lindi di Wilayah Tempat Pembuangan Akhir (TPA) Putri Cempo Surakarta. *Indonesian Journal of Applied Physics*, *6*(1), 13–22. https://doi.org/10.13057/ijap.v6i01.1792

Hartini, E., & Yulianto, Y. (2018). Kajian Dampak Pencemaran Lindi Tempat Pemrosesan Akhir (TPA) Ciangir terhadap Kualitas Air dan Udara. *Jurnal Sains dan Teknologi*, *4*(1), 27–32.

Indriana, R. D., Nurwidyanto, M. I., & Haryono, K. W. (2007). Interpretasi Bawah Permukaan dengan Metode Self Potential Daerah Bledug Kuwu Kradenan Grobogan. *Berkala Fisika*, *10*(3), 155–167.

Krisnohadi, A. (2011). Analisis Pengembangan Lahan Gambut untuk Tanaman Kelapa Sawit Kabupaten Kubu Raya. *Jurnal Tek. Perkebunan & PSDL*, *1*, 1–7. https://doi.org/10.1016/j.appet.2016.05.021

Muhardi, Kaharudin, & Anwar, M. (2021). Application of Self-Potential Method to Observe Groundwater Flow in Tanjungpura University Area, Pontianak. *Indonesian Review of Physics*, *4*(2), 17–22. https://doi.org/10.12928/irip.v4i2.4020

Muliadi, Zulfian, & Muhardi. (2019). Identifikasi Ketebalan Tanah Gambut Berdasarkan Nilai Resistivitas 3D: Studi Kasus Daerah Tempat Pembuangan Akhir Batu Layang Kota Pontianak. *Positron*, *9*(2), 86–94. https://doi.org/10.26418/positron.v9i2.34821

Prasetya, I. N., Putra, Y. S., Muhardi, Muliadi, & Perdhana, R. (2022). Interpretasi Sebaran Lindi di Sekitar TPA Salatiga Kabupaten Sambas Menggunakan Metode Self-Potential. *Jurnal Fisika Unand*, *11*(4), 523–530. https://doi.org/10.25077/jfu.11.4.523-530.2022

Pratama, A. A., Bahri, A. S., & Warnana, D. D. (2017). Pemodelan Pola Aliran Fluida Panas Manifestasi Hidrotermal Songgoriti, Kota Batu Menggunakan Metode Self-Potential. *Jurnal Teknik ITS*, *6*(2), 233–236.

Rosid, S., Koesnodo, R. N., & Nuridianto, P. (2012). Estimasi Aliran Air Lindi TPA Bantar Gebang Bekasi Menggunakan Metoda SP. *Jurnal Fisika Unnes*, *1*(2), 54–59. https://doi.org/10.15294/jf.v1i2.1640

Sampurno, J., Muid, A., Zulfian, & Latief, F. D. E. (2018). Characterization The Geometry of The Peat Soil of Pontianak Using Fractal Method. *Journal of Physics: Conference Series*, *1040*(1). https://doi.org/10.1088/1742-6596/1040/1/012044

Siswoyo, H. (2018). Penyelidikan Potensi Air Tanah pada Lahan Pertanian di Desa Bono Kecamatan Pakel Kabupaten Tulungagung dengan Menggunakan Metode Potensial Diri. *Dinamika Rekayasa*, *14*(2), 112–118. https://doi.org/10.20884/1.dr.2018.14.2.219

Soupios, P., & Karaoulis, M. (2015). Application of Self-Potential (SP) Method for Monitoring Contaminants Movement. *8th Congress of the Balkan Geophysical Society*, 1–5. https://doi.org/10.3997/2214-4609.201414147

Telford, W. M., Geldart, L. P., & Sheriff, R. E. (1990). *Applied Geophysics* (Second Edi). Cambridge University Press.

Thanh, L. D., Thai, N. C., Hung, N. M., Thang, N. C., & Huong, L. T. T. (2020). Self-Potential Method for Detection of Water Leakage Through Dams. *Earth Science Malaysia*, *4*(2), 152–155.

https://doi.org/10.26480/esmy.02.2020.152.155

Vaidila, N., Rini, F. P., & Afrari, I. (2015). Survei Struktur Bawah Permukaan Dengan Metode Self Potential Untuk Mengetahui Potensi Panas Bumi (Studi Kasus Obyek Wisata Guci, Jawa Tengah). *Sainteknol: Jurnal Sains dan Teknologi*, *13*(2), 135–142. https://doi.org/10.15294/sainteknol.v13i2.5246

ISSN: 2579-5821 (Print)
ISSN: 2579-5546 (Online)
URL address: http://journal.unhas.ac.id/index.php/geocelebes
DOI: 10.20956/geocelebes.vxix.xxxx

Jurnal Geocelebes Vol. 7 No. 1, April 2023, 17 - 28

# The Significance Relationship between Palynomorph Fossil Preservation and Grain Size in Rock: Case Study of Walat and Batuasih Formations, Sukabumi, West Java

Rizki Satria Rachman[1]*, Winantris[2]

[1]Pusat Sumber Daya Mineral, Batubara, dan Panas Bumi, Jl. Soekarno Hatta No.444, Pasirluyu, Kota Bandung, Jawa Barat, Indonesia.
[2]Teknik Geologi, Universitas Padjadjaran, Jl. Raya Bandung – Sumedang Km.21, Kabupaten Sumedang, Jawa Barat, Indonesia.

*Corresponding author. Email: rizkisatriarachman@gmail.com

Manuscript received: 15 September 2022; Received in revised form: 20 January 2023; Accepted: 30 January 2023

**Abstract**

Palynomorph is dust-sized material that is resistant to acids and can be preserved as fossils in sedimentary rocks. Fossil content in rocks is very diverse which is influenced by various factors, one of this factors is the texture of rock in form of grain size. The Walat and Batuasih Formations are sedimentary rock formations that have variety of grain sizes. This research aims to examine relationship or correlation between grain size and palynomorph preservation in rocks with case studies in the Walat and Batuasih Formations. 42 samples were taken from measured stratigraphic section and analyzed both grain size and palynomorph content. Statistical analysis with Normality Test using Shapiro Wilk and Liliefors; Homogeneity Test using Levene Test; and Non-Parametric Associative Test using Spearman Rank was conducted to see the relationship of these variables. Result, the Walat and Batuasih Formations have conglomerate, sandstone, mudstone and coal lithologies with quite variety of palynomorphs. Statistical results show that all variables have data that are not normally distributed with tendency to be non-homogeneous. Moreover, it was found that the grain size of rock had significant effect on the preservation of palynomorphs in the rock. Clay grains has positive correlation of 0.613 and sand grains has negative correlation of -0.653. This shows that the finer the grain size, the more effective the preservation of palynomorphs is.

**Keywords**: Batuasih Formation; Grain Size; Palynomorph; Relationship; Walat Formation.

**Citation**: Rachman, R.S. and Winantris. (2023). The Significance Relationship between Palynomorph Fossil Preservation and Grain Size in Rock: Case Study of Walat and Batuasih Formations, Sukabumi, West Java. *Jurnal Geocelebes,* 7(1), 17–28, doi: 10.20956/geocelebes.v7i1.22746

## Introduction

Palynomorph is dust-sized material that is resistant to acids (Dutta et al., 2013; Vernal, 2015). These materials include pollen, spores, dinocyst, foraminifera lining test, acritarch, and chitinozoa (Traverse, 2007). Basically, these materials can be deposited and preserved in rocks and turned into fossils (Suedy et al., 2011; Setijadi et al., 2011). Sedimentary rock is one of the rocks that stores fossil content both palynomorphs and other materials. However, these fossils are not preserved evenly in the rock (Mander & Punyasena, 2018). The number of preserved palynomorph fossils in the rock is influenced by various aspects, one of these factors is the texture of sedimentary rock (Havinga, 1967; Li et al., 2005; Delcourt & Delcourt, 1980).

Several previous studies stated that the texture of rock grain size does affect the preservation of fossil in the rock (Schoeninger et al., 1989; Dashtgard et al.,

2008; Gardner et al., 2016; Evans et al., 2020). The finer the grain size of sedimentary rock, the better the rock will store fossil content (Evans et al., 2020). Previous research has been carried out on macrofossils and some have also discussed them from microfossil aspect (Schopf, 1975; Holland, 2016). However, the level of significance of influence or relationship between rock grain size and palynomorph preservation has not become the study of previous research. Therefore, this research is aimed to see how strong the effect of sedimentary rocks texture in form of grain size on the preservation of palynomorphs in the rock. This study took the Walat Formation and Batuasih Formation as a case study.

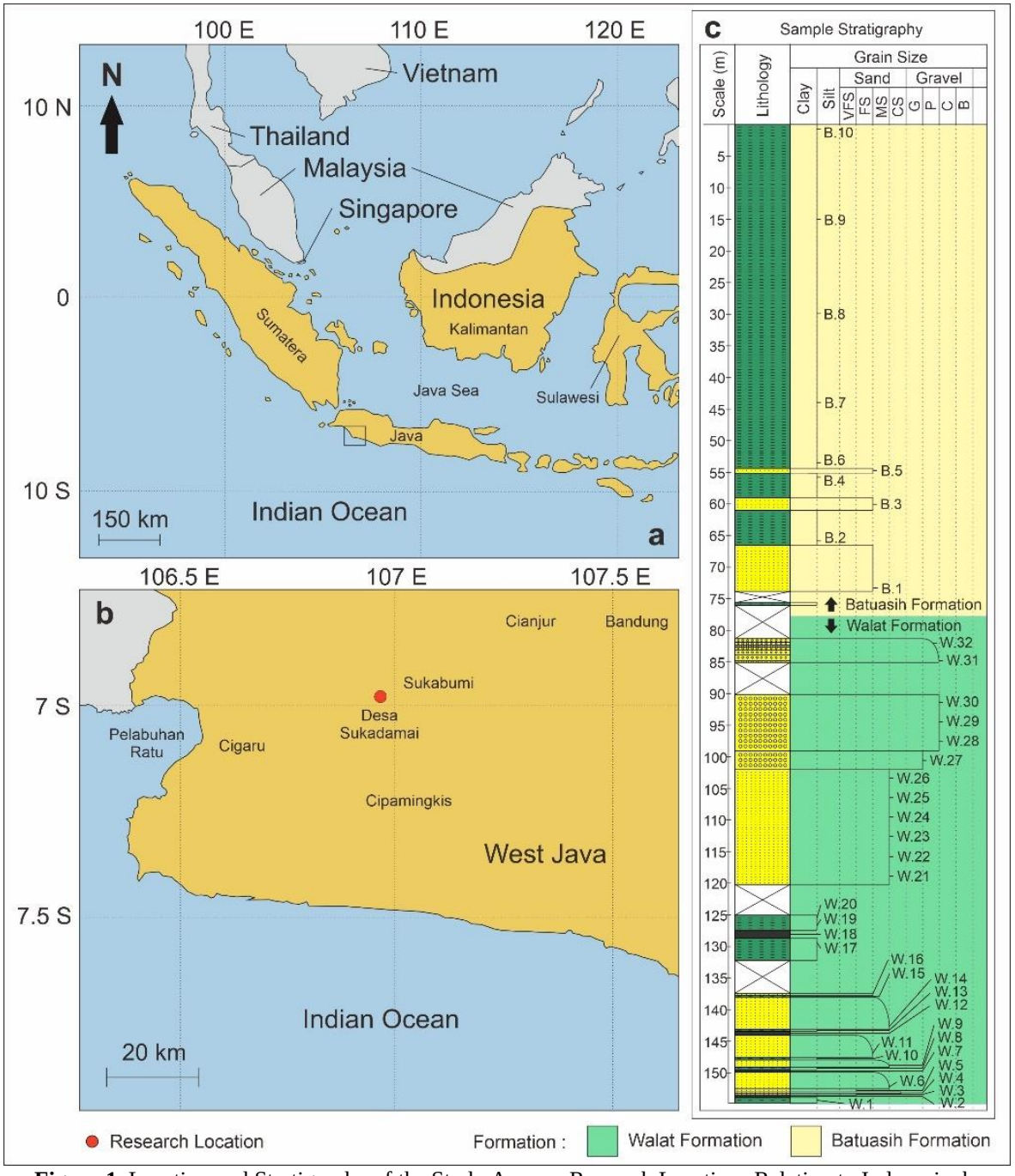


**Figure 1**. Location and Stratigraphy of the Study Area; a. Research Locations Relation to Indonesia; b. Research Location Relation to West Java; c. Stratigraphy of Study Area and Rock Sampling Points (Modification from Rachman et al., 2021).

The Walat and Batuasih Formations are rock formations exposed in Sukabumi area, West Java (Effendi et al., 1998; Martodjodjo, 2003). Rocks in the Walat and Batuasih Formations are very diverse, ranging from mudstone, sandstone, conglomerate, to coal as insert in several parts (Praptisih et al., 2009; Irawan, 2019). At least, Walat and Batuasih Formations have layer thickness up to 1400 m with Late Eocene - Late Oligocene age and terrestrial depositional environments to be precise in the fluvial to transition sections. (Schiller, 1991; Clements, 2007; Hendrizan et al., 2012; Wibowo & Kapid, 2014; Kurniawan et al., 2016). Seeing that these rock characteristics of Walat and Batuasih Formations are quite diverse. It is interesting to see how the relationship between different sedimentary rock types based on grain size and the preservation of palynomorph content in these formations (Martodjodjo, 2003).

## Method

This research is divided into four basic steps, from field activities to laboratory analysis. The research sample was taken from the Walat and Batuasih Formation outcrops in Pasir Pogor mining area and Cibatu River in Sukadamai Village, Cicantayan, Sukabumi, West Java (Figure 1).

### *Sampling*

Fieldwork was carried out to collect research samples along with general characteristics of the Walat and Batuasih Formations. Rock samples were taken using measured stratigraphic section method and taken for each lithology to obtain the diversity of rock lithology (Bellian et al., 2005; Yasin et al., 2017). There were 42 rock samples of various types from the Walat and Batuasih Formations. The sample was then prepared for rock and palynomorph preparation in the laboratory.

### *Palynomorph and Grain Size Preparation*

Palynomorph preparation is carried out using basic method, which is the acid treatment method by reacting rock samples with various chemicals (HF, HCl, KOH, HNO3, and Alcohol) then filtered with a size of 5-200 microns (Dutta et al., 2013; Traverse, 2007). Residual results for each sample then identified its palynomorph content. The rock grain size preparation was carried out by homogeneous crushing method so that the sedimentary rock could decompose in each sediment grain. This is done to identify the grain size in the next step (Israwaty, 2013).

### *Palynomorph and Grain Size Identification*

Palynomorph identification was carried out using binocular microscope CX-22 with 1000x magnification. The names and abundance of palynomorph fossils were identified in each rock formation sample (Winantris et al., 2012). The abundance of palynomorphs was obtained by dividing between the number of identified palynomorphs (P) and the number of residues in the palynomorph preparations (ml). Grain size identification was analyzed by Beckman Coulter LS 13320 Dry Powder System and Universal Liquid Module method to identify how the grain size distribution of rock samples from very fine (0.1 µ) to very coarse (1000 µ) grain size (Blott & Pye, 2006; Suckow, 2013; Schulte et al., 2018). The grain size was further classified according to the sedimentary rock grain size classification (Wentworth, 1922).

### *Palynomorph and Grain Size Statistical Analysis*

Statistical analysis was carried out to see the relationship between palynomorph preservation in rock and grain size of sedimentary rocks from the Walat and Batuasih Formations. Statistical tests were carried out including several tests with their respective statistical test formulas and flows (Figure 2). Statistical analysis was

performed using several tests: Normality Test using Shapiro Wilk and Liliefors; Homogeneity Test using Levene Test; Parametric Associative Test using Product Moment Correlation; and Non-Parametric Associative Test using Spearman Rank. Normality Test and Homogeneity Test were carried out to determine the Associative Test used in this research. From the results of this statistical test, research conclusions can be drawn to see the relationship between these two variables (Sugiyono, 2019).

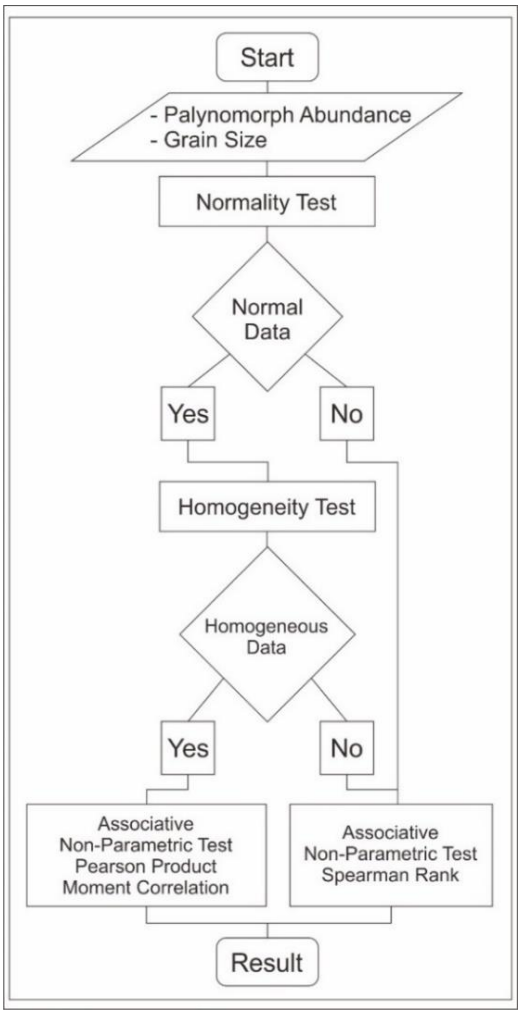


**Figure 2**. Flow of Research Statistical Analysis (Sugiyono, 2019).

## Result and Discussion

*Result*

Results from measured stratigraphic sections show that in the Walat Formation, lithology is found in form of alternating among sandstones, mudstones and coal with several conglomerates found at the top section. While the Batuasih Formation lithology is dominated by mudstone and few sandstones. The Batuasih Formation is stratigraphically located above the Walat Formation (Figure 1c & 3).

Palynomorphs from study area were quite diverse, as found pollen from the Proxapertites group, Spores from Verrucatosporites, and in some samples other palynomorphs from dinocyst and foraminifera lining test were found (Figure 3). Palynomorph content in the study samples varied widely, many of study samples did not show the presence of palynomorphs. However, several samples contain very abundant palynomorphs. From this diversity results, the abundance of palynomorphs was calculated in each study sample. The abundance of palynomorphs in this study ranged from 0 P/ml in some samples to 70 P/ml in sample W.2 (Table 1).

Results from individual palynomorphs and grain size were subjected to statistical tests to see if there was relationship between these two aspects. First statistical test carried out with Normality Test using Shapiro Wilk and Liliefors. Result, all variables analysed, both abundance, clay, silt, and sand, has data types that were not normally distributed. This can be seen from the significance value of 0 (<0.05), it means that the analysed data has an abnormal distribution (Table 2). This causes associative statistical analysis to be carried out with the non-parametric associative analysis.

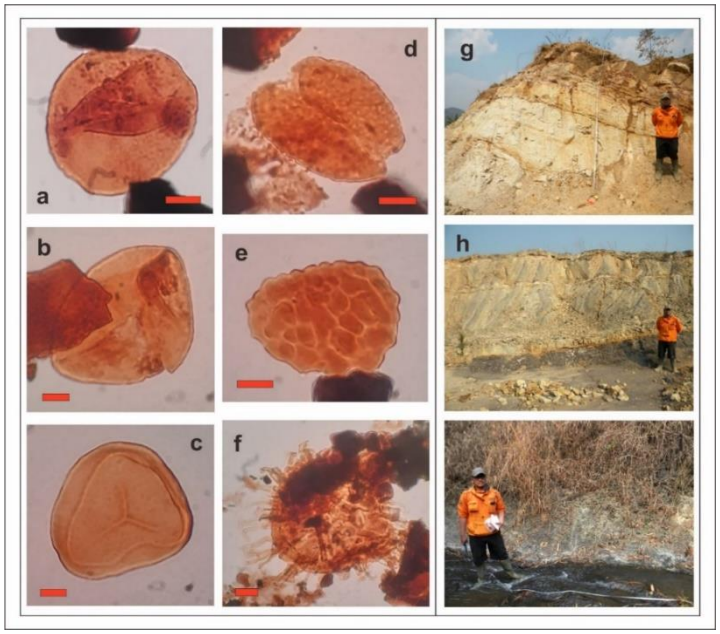


**Figure 3**. Left; Palynomorph of Research Sample; a. *Proxapertites operculatus*; b. *Eucalyptus type*; c. *Lycopodium cernuum type*; d. *Dicolpopollis sp*; e. *Verrucatosporites usmensis*; f. Dynocyst, Right; Rock Outcrop of Research Area; g. Conglomerate from Walat Formation; h. Alternating among sandstones, mudstones and coal from Walat Formation; i. Mudstone from Batuasih Formation.

**Table 1**. Grain size and abundance of palynomorphs.

| Sample Code | Number of Palynomorphs | Residue Amount | Abundance (P/ml) | Clay (%) | Silt (%) | Sand (%) |
|---|---|---|---|---|---|---|
| W.1 | 31 | 15 | 2.07 | 100 | 0.00 | 0.00 |
| W.2 | 210 | 3 | 70.00 | 100 | 0.00 | 0.00 |
| W.3 | 50 | 9 | 5.56 | 100 | 0.00 | 0.00 |
| W.4 | 1 | 9 | 0.11 | 4.68 | 18.23 | 77.09 |
| W.5 | 8 | 9 | 0.89 | 100 | 0.00 | 0.00 |
| W.6 | 0 | 9 | 0.00 | 3.06 | 10.37 | 86.57 |
| W.7 | 205 | 6 | 34.17 | 100 | 0.00 | 0.00 |
| W.8 | 3 | 9 | 0.33 | 53.01 | 46.99 | 0.00 |
| W.9 | 0 | 9 | 0.00 | 2.73 | 11.24 | 86.03 |
| W.10 | 0 | 9 | 0.00 | 100 | 0.00 | 0.00 |
| W.11 | 0 | 9 | 0.00 | 3.60 | 15.84 | 80.56 |
| W.12 | 55 | 9 | 6.11 | 100 | 0.00 | 0.00 |
| W.13 | 0 | 9 | 0.00 | 49.77 | 50.23 | 0.00 |
| W.14 | 0 | 9 | 0.00 | 2.61 | 10.15 | 87.24 |
| W.15 | 0 | 9 | 0.00 | 100 | 0.00 | 0.00 |
| W.16 | 0 | 9 | 0.00 | 3.67 | 12.96 | 83.37 |
| W.17 | 0 | 9 | 0.00 | 100 | 0.00 | 0.00 |
| W.18 | 203 | 6 | 33.83 | 6.45 | 26.96 | 66.59 |
| W.19 | 222 | 6 | 37.00 | 47.63 | 52.37 | 0.00 |
| W.20 | 41 | 15 | 2.73 | 100 | 0.00 | 0.00 |
| W.21 | 20 | 9 | 2.22 | 100 | 0.00 | 0.00 |
| W.22 | 0 | 9 | 0.00 | 4.99 | 11.75 | 83.26 |
| W.23 | 0 | 9 | 0.00 | 4.56 | 15.65 | 79.79 |
| W.24 | 0 | 9 | 0.00 | 0.93 | 7.82 | 91.25 |
| W.25 | 0 | 9 | 0.00 | 3.84 | 8.26 | 87.90 |
| W.26 | 0 | 9 | 0.00 | 3.8 | 10.78 | 85.44 |
| W.27 | 0 | 9 | 0.00 | 3.53 | 9.72 | 86.75 |
| W.28 | 0 | 9 | 0.00 | 4.07 | 24.47 | 71.45 |
| W.29 | 0 | 9 | 0.00 | 2.59 | 8.04 | 89.37 |
| W.30 | 0 | 9 | 0.00 | 2.86 | 9.42 | 87.72 |
| W.31 | 0 | 9 | 0.00 | 5.55 | 13.64 | 80.81 |
| W.32 | 0 | 9 | 0.00 | 1.95 | 10.97 | 87.08 |

| | | | | | | |
|---|---|---|---|---|---|---|
| B.1 | 1 | 9 | 0.11 | 100 | 0.00 | 0.00 |
| B.2 | 3 | 9 | 0.33 | 4.59 | 21.08 | 74.33 |
| B.3 | 0 | 9 | 0.00 | 100 | 0.00 | 0.00 |
| B.4 | 30 | 9 | 3.33 | 100 | 0.00 | 0.00 |
| B.5 | 0 | 9 | 0.00 | 7.63 | 29.91 | 62.46 |
| B.6 | 43 | 9 | 4.78 | 100 | 0.00 | 0.00 |
| B.7 | 50 | 9 | 5.56 | 27.23 | 72.77 | 0.00 |
| B.8 | 10 | 9 | 1.11 | 100 | 0.00 | 0.00 |
| B.9 | 34 | 9 | 3.78 | 100 | 0.00 | 0.00 |
| B.10 | 2 | 9 | 0.22 | 100 | 0.00 | 0.00 |

**Table 2**. Normality test results with Shapiro Wilk and Liliefors.

| Variable | Significance | Conclusion |
|---|---|---|
| Abundance (A) | 0 | Distribution data is Not Normal |
| Clay (C) | 0 | Distribution data is Not Normal |
| Silt (Si) | 0 | Distribution data is Not Normal |
| Sand (Sa) | 0 | Distribution data is Not Normal |

Next, statistical analysis was the homogeneity test using the Levene Test. Results were mixed, non-homogeneous data were obtained in comparison of Abundance and Clay; Abundance and Sand; Clay and Silt; Silt and Sand. Meanwhile, homogeneous data were obtained in the comparison of Abundance and Silt; Clay and Sand. This can be seen from the significance value of 0.15 and 0.19 (>0.05), which means that the data is homogeneous data (Table 3). Although some data show homogeneous data, the normality test conducted previously showed that all data were not normally distributed. This causes associative statistical analysis to be carried out with the non-parametric associative analysis and is not affected by the homogeneity of data.

**Table 3**. Homogeneity test results with the Levene Test

| Variable | Significance | Conclusion |
|---|---|---|
| Abundance and Clay | 0 | Non-Homogeneous data |
| Abundance and Silt | 0.15 | Homogeneous data |
| Abundance and Sand | 0 | Non-Homogeneous data |
| Clay and Silt | 0 | Non-Homogeneous data |
| Clay and Sand | 0.19 | Homogeneous data |
| Silt and Sand | 0 | Non-Homogeneous data |

Last, statistical analysis is the Associative Test using Spearman Rank. Result, palynomorph preservation (abundance) has a significant relationship or correlation with clay and sand. This can be seen from the significance value of 0 (<0.05), which means the two variables have relationship with certain level of correlation (Table 4). Abundance and clay obtained positive correlation of 0.613 which is classified as strong correlation based on Sugiyono (2019). This means that palynomorph preservation in rock will be more effective when there is more clay grain size content in the rock. Abundance and sand obtained negative correlation of -0.653 which is classified as a strong correlation based on Sugiyono (2019). This means that palynomorph preservation in rock will be less effective when there is more sand grain size content in the rock. Whereas Abundance and Silt did not have significant correlation. This means that the amount of silt grain size in the rock does not affect abundance of palynomorph preservation in the rock.

**Table 4**. Associative test results with Spearman Rank

| Variable | Significance | R | Conclusion |
|---|---|---|---|
| Abundance and Clay | 0 | 0.613 | Correlated |
| Abundance and Silt | 0.097 | 0.26 | Uncorrelated |
| Abundance and Sand | 0 | -0.653 | Correlated |

*Discussion*

Results from associative test show the effect of grain size on preservation of palynomorphs in the rock (Table 4). Palynomorphs are more dominant in fine-grained sedimentary rocks, both in clay and coal. However, some rock samples with sand grain size can still contain palynomorph. Palynomorphs that are present in mudstone and coal come from all species with various distributions that have size range of 10 – 99 µ. Whereas in the sandstones, palynomorphs that are present only come from certain species which have size range of 10 – 89 µ.

In the Table 5, the lithology of coal, mudstone and sandstones contains palynomorphs that range from small to large species sizes. But in sandstones, palynomorphs come from species *Crassoretitriletes vanraadshoveni, Dipterocarpus intricatus, Laevigatosporites, Lycopodiumsporites semimuris, Malvacipollis diversus, Palmaepollenites kutchensis, Proxapertites cursus,* and *Proxapertites operculatus*. These palynomorphs have large species size which is higher when compared to other species. Thus, in sandstones, palynomorphs can be preserved in small amounts. But, this palynomorph must have sufficiently large species size. Batten (1974) suggests that small and medium sized palynomorphs increase in silt-clay grain size and decrease closer to the sand grain size. Meanwhile, large palynomorphs increased closer to the silt-sand grain size and then decreased to grain size, which is larger than sand. The result is consistent with this study, large palynomorphs tend to be preserved in sandstone lithology in several species.

**Table 5**. Palynomorph relations and grain size.

| Fossil Name | Quantity | Size (µ) | Lithology |
|---|---|---|---|
| *Acritarchs* | 4 | 20 – 49 | L, MS |
| *Acrostichum type* | 84 | 20 – 69 | L, MS |
| *Apocynaceae type* | 1 | 30 – 49 | L |
| *Cicatricosisporites dorogensis* | 2 | 40 – 89 | L, MS |
| *Chepalomappa malloticarpa* | 7 | 30 – 59 | MS |
| *Clavifera triplex* | 1 | 20 – 29 | MS |
| *Crassoretitriletes vanraadshoveni* | 2 | 40 – 69 | MS, SS |
| *Dicolpopollis sp* | 16 | 10 – 89 | L, MS |
| *Dipterocarpus intricatus* | 3 | 40 – 69 | SS |
| *Distaeverrusporites simplex* | 1 | 30 – 39 | MS |
| *Eucalyptus type* | 1 | 40 – 49 | L |
| *Foraminifera Test Lining* | 2 | 30 – 69 | MS |
| *Indeterminate* | 4 | 10 – 39 | MS |
| *Laevigatosporites* | 29 | 30 – 69 | L, MS, SS |
| *Ligaria cuneifolia* | 1 | 10 – 29 | L |
| *Lycopodium cernuum type* | 2 | 20 – 39 | L, MS |
| *Lycopodiumsporites semimuris* | 47 | 20 – 69 | L, MS, SS |
| *Malvacipollis diversus* | 12 | 20 – 89 | L, SS |
| *Palmaepollenites kutchensis* | 8 | 10 – 89 | L, MS, SS |
| *Podocarpidites marwickii* | 2 | 30 – 99 | MS |
| *Podocarpidites otagoensis* | 1 | 30 – 49 | L |
| *Polyadopollenites microreticulatus* | 1 | 30 – 39 | L |
| *Proxapertites cursus* | 116 | 20 – 89 | L, MS, SS |
| *Proxapertites operculatus* | 780 | 20 – 89 | L, MS, SS |
| *Proxapertites psilatus* | 61 | 20 – 89 | L, MS |
| *Spiniferites pseudofurcatus* | 1 | 70 – 89 | MS |
| *Spiniferites ramosus* | 1 | 20 – 39 | MS |
| *Trichotomosulcites subgranulatus* | 1 | 20 – 39 | MS |
| *Tricolpites confessus* | 2 | 30 – 49 | MS |
| *Tricolpites reticulatus* | 4 | 30 – 59 | L, MS |
| *Verrucatosporites usmensis* | 24 | 20 – 69 | L, MS |

Figure 4, shows that the whole rock sample (coal, mudstone, and sandstone) dominated by individual palynomorphs of 30 - 59 µ size. Palynomorphs with 10 - 59 µ size have higher content in coal and claystone than sandstones. However, larger individuals (60 - 89 µ) palynomorphs are higher preserved in sandstones than in coal and mudstones. From Figure 4, it can also be seen that lithology of coal and claystone has plot points that are always higher than sandstones for small individual sizes (10 - 59 µ). Whereas at the transition size 59 - 60 µ, the crossover occurs so that sandstone lithology has a higher plot point than coal and claystone for large individual sizes (60 - 89 µ). From this description, palynomorph fossils can be preserved in sandstones but with lower abundance compared to coal and claystone. As for sandstones, larger individual palynomorph sizes are easier to preserve than for coal and claystones. So that large palynomorphs such as *Proxapertites* group can be well preserved in sand grain size (Hesse & Zetter, 2007). Due to its abundance and large species size, *Proxapertites* became the most dominant palynomorph from this study.

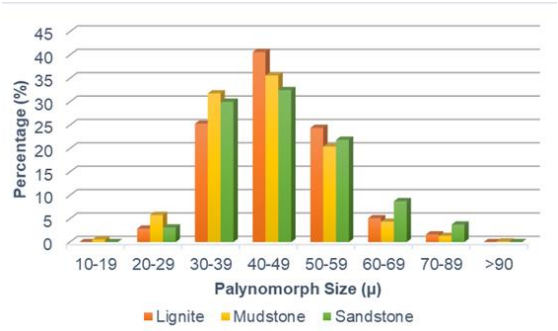


**Figure 4**. Bar diagram showing percentage of each palynomorph size from rock sample

Results showed that palynomorphs were more abundant in rocks with fine grain size (clay) and less in rocks with coarse grain size (sand). It happens because the sand grain size tends to have pores that have potential to flow air into the rock. So that the rocks are not in anoxic conditions (no oxygen) which is one of conditions for fossils to be formed. When air enters the rock, palynomorphs are immediately destroyed. Whereas in clay grain size, air tends not to enter the pores of rock and can better preserve fossils. Consistent with the literature, this research found that the preservation of fossils in rocks is greatly influenced by the texture of the rock itself so that fossils can avoid destructive factors such as oxygen.

Several studies of palynomorphs suggest that the condition of rock grain size affects the level of palynomorph preservation in these rocks. Delcourt & Delcourt (1980) states that palynomorphs tend not to be preserved at coarse grain size for two reasons. First, it is caused by oxidation of palynomorphs due to rock pores that are large enough for oxygen to enter, second is the possibility that palynomorphs in the coarse grain size area have high enough energy level so that the palynomorphs are not deposited in that area and are carried away to areas with lower energy. This is what causes the rock grain size in this study to affect palynomorphs. Rock samples that have coarse grain size tend to be very little and do not even show palynomorph in them. Li et al. (2005) states that depth, age, and depositional environment affect preservation of palynomorphs in the rock. In this research, age and environment are interpreted in same condition because these samples are taken in the same formation and are similar both in terms of age and depositional environment. So that the effect of grain size on palynomorph preservation here is not influenced by changes in age and depositional environment.

Results of this study are also in line with Schoeninger et al. (1989) dan Evans et al. (2020) who found that fossils in rocks are greatly affected by the rock grain size. Fossils are more effective for preservation in rocks with finer grain sizes. It happens because the grain size of rock can protect the fossil from environmental influences that can destroy the fossil. While Batten (1974) states that palynomorphs are very sensitive to changes in rock grain size, many

palynomorphs are preserved in rocks with fine grain sizes, so that fossils can be preserved in anoxic conditions.

Several studies have found that the preservation of palynomorphs is also influenced by the composition and characteristics of palynomorphs themselves. Campbell (1999) found that the preservation of palynomorphs in rocks is influenced by the exine composition of each palynomorph. Basically, the exine of each palynomorph has different thickness and sporopollenin content. In this study, the effect of sporopollenin was not significant because the same palynomorphs were present and randomly distributed in the rock samples. There is no grouping as particular genus is present only in fine grain size and another genus is present at coarse grain size indicating that sporopollenin composition does not affect palynomorph preservation in this study. Therefore, palynomorph preservation in this study is strongly influenced by grain size distribution compared to other influences. However, the effects described in previous studies still influence the preservation of palynomorphs with their respective aspects.

From the description above, rock grain size is one of the significant influences in palynomorph preservation of rock from certain formation. Palynomorphs are more effectively preserved in finer grain sizes than coarse grain sizes. As for coarse grain size, palynomorphs with large sizes tend to be better preserved than those with fine grain sizes. Therefore, in palynomorph analysis, the research sample used as best as possible has fine grain size so that interpretation can be carried out properly because of enough palynomorphs.

## Conclusion

The Walat and Batuasih Formations have various lithologies in form of conglomerates, sandstones, mudstone, and coal. Palynomorph of research sample was quite diverse with the discovery of pollen in form of *Proxapertites* groups, Spores from *Verrucatosporites*, as well as dinocysts and foraminifera lining tests. The abundance of palynomorphs in this study ranged from 0 P / ml in some samples to 70 P / ml in sample W.2.

The statistical results show that all variables have data that are not normally distributed with a tendency not to be homogeneous. In addition, it was found that the rock grain size had significant effect on palynomorph preservation. The clay grain size has positive correlation of 0.613 and the sand grain size has negative correlation of -0.653. This indicates that the finer the grain size, the more effective palynomorph preservation will be. In addition, lithology with coarse grain size (sandstone) contains palynomorphs with large individual sizes higher than fine grain sizes (coal and claystone).

## Acknowledgements

Thank you to the Chancellor of Padjadjaran University for funding research through the HIU-RKDU program, Paleontology laboratory team of the Faculty of Geological Engineering UNPAD, and all parties who have helped and provided encouragement in this research.

## Author Contribution

The author is a researcher who carries out activities from sampling to completing paper writing with guidance from the author's lecturer.

## Conflict of Interest

No potential conflict of interest was reported by the authors. This research was carried out entirely by the author under the guidance of author’s lecturer. The research fee was provided by author’s lecturer through research fees from the university.

**References**


Batten, D.J. (1974). Wealden Palaeoecology from the Distribution of Plant Fossils. *Proceedings of the Geologists' Association*, 85(4), 433–458. https://doi.org/10.1016/S0016-7878(74)80068-4

Bellian, J.A., Kerans, C., & Jennette, D.C. (2005). Digital Outcorp Models: Applications of Terrestrial Scanning Lidar Technology in Stratigraphic Modeling. *Journal of Sedimentary Research*, 75(2), 166–176. https://doi.org/10.2110/jsr.2005.013

Blott, S.J. & Pye, K. (2006). Particle size distribution analysis of sand-sized particles by laser diffraction: an experimental investigation of instrument sensitivity and the effects of particle shape. *Sedimentology*, 53(3), 671–685. https://doi.org/10.1111/j.1365-3091.2006.00786.x

Campbell, I.D. (1999). Quaternary pollen taphonomy: examples of differential redeposition and differential preservation. *Palaeogeography, Palaeoclimatology, Palaeoecology*, 149(1-4), 245–256. https://doi.org/10.1016/S0031-0182(98)00204-1

Clements, B. (2007). Cretaceous to Late Miocene Stratigraphic and Tectonic Evolution of West Java. *Proceedings Indonesian Petroleum Association Thirty-First Annual Convention and Exhibition* (pp.1-18). American Association of Petroleum Geologists.

Dashtgard, S.E., Gingras, M.K., & Pemberton, S.G. (2008). Grain-size controls on the occurrence of bioturbation. Palaeogeography, Palaeoclimatology, Palaeoecology, 257(1-2), 224–243. https://doi.org/10.1016/j.palaeo.2007.10.024

Delcourt, P.A. & Delcourt, H.R. (1980). Pollen preservation and quaternary environmental history in the Southeastern United States. Palynology, 4(1), 215–231. https://doi.org/10.1080/01916122.1980.9989209

Dutta, S., Hartkopf-Froder, C., Witte, K., Brocke, R., & Mann, U. (2013). Molecular characterization of fossil palynomorphs by transmission micro-FTIR spectroscopy: Implications for hydrocarbon source evaluation. *International Journal of Coal Geology*, 115, 13–23. https://doi.org/10.1016/j.coal.2013.04.003

Effendi, K. & Hermantos. (1998). *Peta Geologi Lembar Bogor, Jawa skala 1:100.000*. Pusat Penelitian dan Pengembangan Geologi, Bandung.

Evans, S.D., Dzaugis, P.W., Droser, M.L., & Gehling, J.G. (2020). You can get anything you want from Alice's Restaurant Bed: exceptional preservation and an unusual fossil assemblage from a newly excavated bed (Ediacara Member, Nilpena, South Australia). *Australian Journal of Earth Sciences*, 67(6), 873–883. https://doi.org/10.1080/08120099.2018.1470110

Gardner, E.E., Walker, S.E., & Gardner, L.I. (2016). Palaeoclimate, environmental factors, and bird body size: a multivariable analysis of avian fossil preservation. *Earth Science Review*, 162, 177–197. https://doi.org/10.1016/j.earscirev.2016.07.001

Havinga, A.J. (1967). Palynology and Pollen Preservation. *Review of Palaeobotany and Palynology*. 2(1-4), 81–98. https://doi.org/10.1016/0034-6667(67)90138-8

Hendrizan, M., Praptisih., & Putra, P.S. (2012). Depositional Environment of the Batuasih Formation on the Basis of Foraminifera Content: A Case Study in Sukabumi Region, West Java Province, Indonesia. *Indonesian Journal of Geology*, 7(2), 101–112. https://doi.org/10.17014/ijog.v7i2.139

Hesse, M. and Zetter, R. (2007). The fossil pollen record of Araceae. *Plant Systematics and Evolution*, 263(1), 93–115. https://doi.org/10.1007/s00606-006-0468-z

Holland, S.M. (2016). The non-uniformity of fossil preservation. *Philosophical Transactions of the Royal Society B: Biological Sciences*, 371, 1–11. https://doi.org/10.1098/rstb.2015.0130

Irawan, P. (2019). Eksplorasi Air Tanah di Kampung Tajur Desa Pemagasari Kecamatan Parung Kabupaten Bogor. *Jurnal Siliwangi*, 5(1), 14–25.

Israwaty, I. (2013). The Separation Study of Poboya Ore Gold (Central Sulawesi) with Flotation and Sink Tehniques with TBE (Tetrabromoethane) as a Media. *Jurnal Chemica*, 14, 84–90.

Kurniawan, E., Syahrulyati, T., & Syaiful, M. (2016). Geologi Dan Sumberdaya Batubara Daerah Lebaktipar Dan Sekitarnya Kecamatan Cilograng Kabupaten Lebak Provinsi Banten. *Jurnal Online Mahasiswa (JOM) Bidang Teknik Geologi*, 1(1), 1–14.

Li, Y.C., Xu, Q.H., Yang, X.L., Chen, H., & Lu, X.M. (2005). Pollen-vegetation relationship and pollen preservation on the Northeastern Qinghai-Tibetan Plateau. *Grana*, 44, 160–171. https://doi.org/10.1080/00173130500230608

Mander, L. & Punyasena, S.W. (2018). Fossil Pollen and Spores in Paleoecology. In: Croft D., Su D., Simpson S. (eds) *Methods in Paleoecology. Vertebrate Paleobiology and Paleoanthropology* (pp.215-234). Springer International Publishing, Cham. https://doi.org/10.1007/978-3-319-94265-0_11

Martodjojo, S. (2003). *Evolusi Cekungan Bogor, Jawa Barat*. Bandung: Institut Teknologi Bandung.

Praptisih, P., Kamtono, K., Putra, P., & Hendrizan, M. (2014). Karakteristik Batuan Sumber (Source Rock) Hidrokarbon pada Formasi Batuasih di daerah Sukabumi, Jawa Barat. *Indonesian Journal on Geoscience*, 4(3), 167–175. http://dx.doi.org/10.17014/ijog.vol4no3.20092

Rachman, R.S., Winantris., & Muljana, B. (2021). Age and Depositional Environment of Walat Formation Based on Palynological Analysis in Sukabumi Regency, West Java, Indonesia. *Pakistan Journal of Geology*, 5(1), 1–7. https://doi.org/10.2478/pjg-2021-0001

Schiller, D.M. (1991). Eocene Submarine Fan Sedimentation in Southwest Java. *Proceedings Indonesian Petroleum Association 20th Annual Convention and Exhibition*, 125–181. American Association of Petroleum Geologists.

Schoeninger, M.J., Moore, K.M., Murray, M.L., & Kingston, J.D. (1989). Detection of bone preservation in archaeological and fossil samples. *Applied Geochemistry*, 4, 281–292. https://doi.org/10.1016/0883-2927(89)90030-9

Schopf, J.M. (1975). Modes of Fossil Preservation. *Review of Palaeobotany and Palynology*, 20, 27–53.

https://doi.org/10.1016/0034-6667(75)90005-6

Schulte, P., Sprafke, T., Rodrigues, L., & Fitzsimmons, K.E. (2018). Are fixed grain size ratios useful proxies for loess sedimentation dynamics? Experiences from Remizovka, Kazakhstan. *Aeolian Research*, 31, 131–140. https://doi.org/10.1016/j.aeolia.2017.09.002

Setijadi, R., Widagdo, A., & Suedy, S.W.A. (2011). Climate Change Bioprediction Method used Pollen and Spore Fossil at Pliocene Age in Banyumas. *Dinamika Rekayasa*, 7(1), 14–16. http://dx.doi.org/10.20884/1.dr.2011.7.1.42

Suckow, A. (2013). A new database sub-system for grain-size analysis. *EGU General Assembly Conference Abstracts*, 14026.

Suedy, S.W.A., Qayim, M.I., Sabiham, S., & Setijadi, R. (2011). Biodiversitas Paleoflora Banyumas Kala Pliosen Berdasarkan Bukti Palinologi. *Berkala Penelitian Hayati*, 7A, 69–73.

Sugiyono. (2019). *Statistika Untuk Penelitian.* Bandung: Alfabeta.

Traverse, A. (2007). *Paleopalynology 2nd edition*. Netherlands: Springer.

Vernal, A.D. (2015). Palynology (Pollen, Spore, etc.). *Encyclopedia of Marine Geosciences*, 1–9. https://doi.org/10.1007/978-94-007-6644-0_87-1

Wentworth, C.K. (1922). A scale of grade and class terms for clastic sediments. *The Journal of Geology*, 30(5), 377–392. https://doi.org/10.1086/622910

Wibowo, U.P. & Kapid, R. (2014). Biostratigrafi Nannoplankton Daerah Rajamandala. *Jurnal Geologi Sumber Daya Mineral*, 15(4), 185–194. https://doi.org/10.33332/jgsm.geologi.v15i4.57

Winantris., Syafri, I., & Rahardjo, A.T. (2012). Oncosperma Tigillarium Merupakan Bagian Palino Karakter Delta Plain di Delta Mahakam, Kalimantan. *Bionatura*, 14(3), 228–236.

Yasin, M., Shahzad, A., Abbasi, N., Ijaz, U., & Khattak, Z. (2017). The Use of Stratigraphic Section in Recording Quagmire of Information for the Fluvial Depositional Environment - A Worked Example in District Poonch, Azad Jammu and Kashmir, Pakistan. *Pakistan Journal of Geology*, 1(2), 1–2. http://doi.org/10.26480/pjg.02.2017.01.02

ISSN: 2579-5821 (Print)
ISSN: 2579-5546 (Online)
URL address: http://journal.unhas.ac.id/index.php/geocelebes
DOI: 10.20956/geocelebes.vxix.xxxx

Jurnal Geocelebes Vol. 7 No. 1, April 2023, 29 – 36

# Susceptibility of the Surrounding Soil and Rock by the Electrical Resistivity Method

Ratna Husain*, Sultan

Department of Geology, Faculty of Engineering, Hasanuddin University, Makassar, Indonesia

*Corresponding author. Email: ratna7geologi@gmail.com

Manuscript received: 7 November 2022; Received in revised form: 26 January 2023; Accepted: 14 February 2023

**Abstract**

The research area is located in Banga, Soppeng Regency, South Sulawesi Province. The purpose and intent of this research is to determine the resistivity value of the material layer, identify the characteristics of the slip plane and its relationship to the plasticity properties and the characteristics of the clay minerals contained in the soil. The method used to collect field data includes surface geological data and subsurface geology, which are the electrical resistivity data and surface soil data, then interpreted by combining topographiccross-sectional data and subsurface geoelectrical data along the measurement path. The first slip plane is curved as well as the second slip plane is the residual soil resulting from weathering of limestone which is still above the less dense and thick parent rock (in situ). The geochemistry of the soil samples showed that the mineral content in each layer had the largest percentage of illite 54.4% - 69.9%, and montmorillonite 6.1% - 13.6%, these two clay minerals have large shrinkage properties. Plasticity Index 29.8% - 35.8%, causing vulnerability to the soil, so that the mass movement on the sliding plane is moderate and active in slow motion. The mass movement in the slip plane can be categorized into creep type.

**Keywords**: plasticity index; resistivity; slip plan; XRD.

**Citation**: Husain, R. & Sultan. (2023). Susceptibility of the Surrounding Soil and Rock by the Electrical Resistivity Method. *Jurnal Geocelebes*, 7(1), 29-36, doi: 10.20956/geocelebes.v7i1.23889

## Introduction

The Banga area is a place for sampling soil and geoelectric data, mostly steep topography, which is traversed by connecting roads from Makassar to Soppeng Regency and from Soppeng Regency to Makassar. This road section often suffers from cracks and damage to the road body and certain parts collapse, so attention is needed from the local government, so that landslide – prone locations can be anticipated so as not to cause a disaster.

Several studies to determine the slip plane using the geoelectric method have been carried out such as Permanasari et al. (2020) and Tejakusuma (2020), but this study tries to relate the soil and mineral content contained as a result of weathering of the bedrock whether it plays an important role in the occurrence of landslide both on a large and small scale.

One of the factors that influence the cause of ground motion is the presence of a sliding plane or a shear plane. Generally, avalanches will occur above the slip plane so that the layers of soil or rock above it can move. Several methods can be used to identify slip planes, one of which is the resistivity geophysical method. The geoelectric method has the advantage that it is safe for the environment, low cost, and the type of soil layer can be recorded to great depths (Aweda et al., 2023; Bamerni and Mohammed, 2023), so this method is used in surveys to obtain subsurface data. The thickness of soil and clay minerals,

which have expansive properties, also contributes to the soil becoming plastic (Husain, 2015).

In addition to the presence of slip planes, weathering of bedrock factors can produce different minerals contained in the soil, so that soil properties can be determined depending on the minerals formed during the weathering process of the original rock (Husain et al., 2015).

Limestone (Figure 1) is the main constituent rock of the Banga area (Sukamto, 1982), is widely distributed and occupies the high-altitude area of the study site. The megascopic appearance of fresh grayish white color and blackish brown weathered color, consisting of grain, sparite, micrite in the form of calcite minerals is called Packstone (Dernaika et al., 2023).

**Figure 1.** Limestone outcrop.

Soil derived from weathered rocks that have undergone chemical and physical weathering, which does not undergo displacement in the parent rock, is called residual soil (Sudarsono and Hasibuan, 2011), showing a dry brown color and a blackish brown color when wet.

## Methods

The location for collecting geoelectric data (Figure 2), as well as for soil samples is carried out at coordinates between 04°29'49" S – 04°31'18" S and 119°49'53" E – 119°51'23" E.

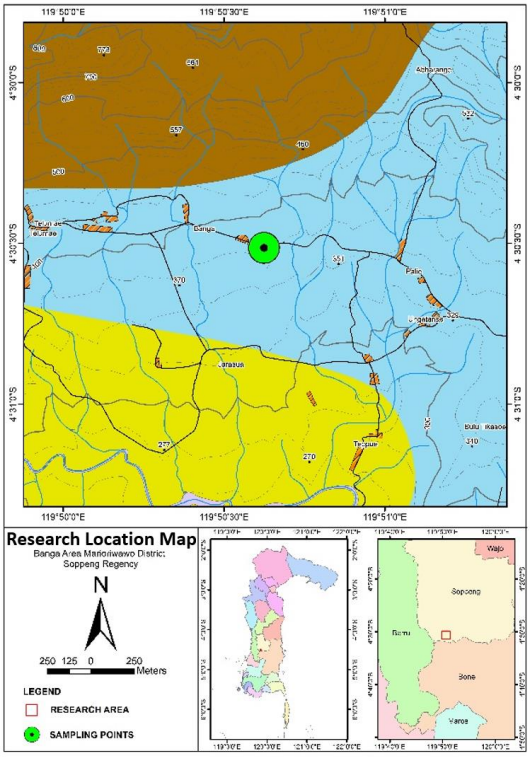


**Figure 2**. Location of sampling.

Preparation of equipment used in GPS surveys, a Brunton compass, a unit of resistivity meter and its accessories, and application program software, GIS (ArcGis 9.3 MapsSource Garmin, Surfer 11 and Global Mapper 13) and resistivity application program (GeoRes v3. b14) and Res2DInv.

The analyzed data is correlated between rock resistivity and geological factors, then converted from subsurface rock resistivity, so that the mineral resistivity value can be known (Martorana and Capizzi, 2023; Shanshal and Al-Mashhadany, 2023) and the type of subsurface material (Adam et al., 2023; Almeida et al., 2023). The resistivity measurement results are analyzed to obtain subsurface rocks, based on these values produce a two-dimensional profile image.

Soil samples were taken using a hand auger at a depth so shallow that it could not be taken by the tool. Then the soil was analyzed using the XRD method to determine the mineral composition

contained in the soil. Soil samples were taken using a hand drill at a depth so shallow that it could not be taken by the tool. Then the soil was analyzed using the XRD method to determine the mineral composition contained in the soil.

## Results and Discussion

Data collection using a multichannel geoelectric device with a Wenner configuration (Bundang et al., 2022; Amsah and Umar, 2020), measurements were carried out using a stretch length of 150 m, electrode distance of approximately 10 m. In this area there is evidence of ground movement, there are cracks above the highway and the road body is partially broken, the dimensions of the cracked road are 25 meters long, 5 meters high, 18o slope and 1-meter-thick soil. Dry brown soil and blackish brown wet soil, medium plant vegetation and crushed limestone.

The data obtained after the apparent resistivity calculation is inverted with the Res2Dinv program. The result of the program inversion is a 2-dimensional resistivity cross-section (Aryadi, 2014), which can be seen in Figure 3. The interpretation of the lithological cross section based on the resistivity value.

The data analysis produces variations in the resistivity value from 0.1 m to 274 m, it can be interpreted that there is an accumulation of water mixed with residual soil with a resistivity value of 0.1 m - 45.5 m. Located on the 15th to 135th meters with a depth of 2.5-31.9 meters. The reason for the existence of the layer below is an impermeable rock layer where the nature of this layer is very difficult for water to pass. Furthermore, there is a second layer which has a resistivity value of 45.6 m - 100 m, which is interpreted as a layer of non-resistant limestone and mixed with clay-sized soil (clays). This layer also contains water caused by the lack of water in the soil layer because the rock layers below are not impermeable to water. Located at the 23rd to 60th meters and 58th to 125th meters at a depth of 2.5 to 10 m.

The lowest layer is the rock layer with the highest resistivity value of 100.1 Ωm - > 274 Ωm. The resistivity value can be interpreted as a layer of limestone (Azis et al., 2023; Rahmaniah et al., 2021). Located at 74 – 112 meters with a depth of 12.5 – 31.9 meters.

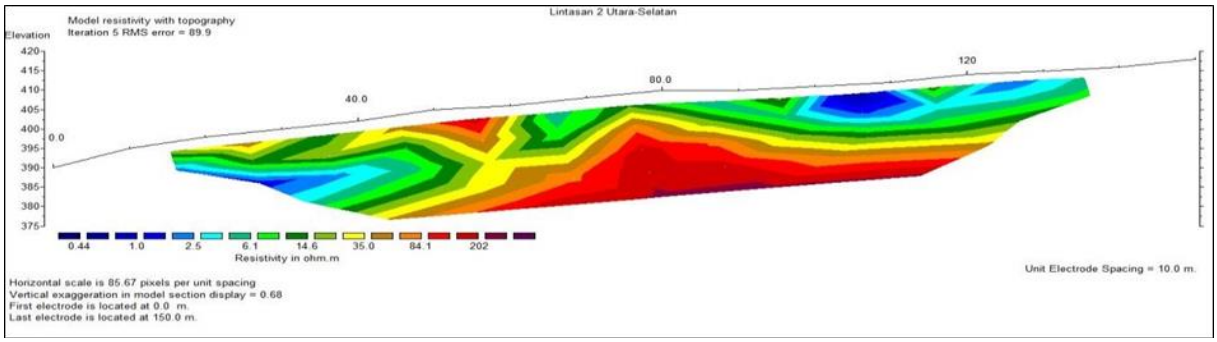


**Figure 3.** Geoelectric inverse section.

*Slip plan analysis*

Analysis of landslides that may occur above the slip plane can be determined based on field data processing in the form of surface data which is then combined with subsurface data from the results of geoelectrical analysis. Field data and geoelectrical data in an area are used to determine the direction of the avalanche slip plane. Field data and geoelectrical data in an area are used to determine the direction of the avalanche slip plane. Before carrying out the analysis of

determining the slip plane, it must first be known that places that are prone to ground motion can be seen from the slope, geomorphology, and constituent rocks.

The interpretation of the geoelectrical resistivity inversion section shows the presence of a slip plane on this line. The low resistivity value is between the higher resistivity values to form a slip plane. This layer is easy to flow and erodes, layers with low resistivity values (0.1 m - 45.5 m) are residual soil as a result of weathering of sedimentary rocks, which is limestone with resistivity values of 100.1 m - 274 m as source rock (in situ). less dense and thick.

The first slip plane was found at the 85th meter to the 43rd meter with a depth of 2.5 meters to a depth of 20 meters. The direction of the slip plane relative to North to South is in the direction of the slope of the rock layers.

*XRD analysis test*

The weathering process will change the rock or dissolve some minerals so that it becomes soil, then transported and deposited as unconsolidated sedimentary rock. Some minerals dissolve completely and form new minerals. Soil composition does not only depend on the source rock (origin), they are all influenced by nature, intensity, and duration (length of time), weathering and the soil type depend on weathering process (Vieira et al., 2020). In chemical weathering water and dissolved gases play a very important role, while chemical weathering itself has the most important role in all types of weathering. This is why in the study of soil or clastic rock it has a mineral composition that can be very different from the rock of origin.

The results of the XRD analysis on the top layer contained the following minerals (Figure 4):

- Illite ($Al_4KO_{12}Si_2$): 69.9%
- Vermiculite ($H_2Mg_3O_{12}$) 14.6%
- Chlorite ($H_4Mg_3O_9Si_2$) 9.4%
- Montmorillonite ($Al_2CaO_{12}Si_4$) 6.1%
- Kaolinite ($Al_2H_4O_9Si_2$) 0.0%
- Aluminium silicate hydroxide ($Al_2H_8O_{11}S_{i2}$) 0.0%

The results of the XRD analysis on the middle layer contained the following minerals (Figure 5):

- Illite ($Al_4KO_{12}Si_2$): 54.4%
- Vermiculite ($H_2Mg_3O_{12}$) 18.3%
- Chlorite ($H_4Mg_3O_9Si_2$) 13.7%
- Montmorillonite ($Al_2CaO_{12}Si_4$) 13.6%
- Kaolinite ($Al_2H_4O_9Si_2$) 0.0%
- Aluminium silicate hydroxide ($Al_2H_8O_{11}S_{i2}$) 0.0%

The results of the XRD analysis on the bottom layer contained the following minerals (Figure 6):

- Illite ($Al_4KO_{12}Si_2$): 65.5%
- Vermiculite ($H_2Mg_3O_{12}$) 22.6%
- Montmorillonite ($Al_2CaO_{12}Si_4$) 9.1%
- Chlorite ($H_4Mg_3O_9Si_2$) 2.5%
- Kaolinite ($Al_2H_4O_9Si_2$) 0.0%
- Aluminium silicate hydroxide ($Al_2H_8O_{11}S_{i2}$) 0.0%

*Atterberg analysis test*

Classification of plasticity index and soil type, according to Table 1:

**Table 1.** Plasticity index value and soil type (Chen, 1988; Keskin et al., 2023).

| PI | Property | Soil Type |
|---|---|---|
| 0 | Non plastics | Sand |
| < 7 | Low plasticity | Silt |
| 7 – 17 | Medium plasticity | Silty clay |
| > 17 | High plasticity | Clay |

The results of data processing to determine the Atterberg test on the upper layer have a liquid limit value (LL) of 82.80%; plastic limit (PL) 50.02%; Plasticity index (PI) 32.78%. The Atterberg test on the middle layer has a liquid limit value (LL) of 82.80%. plastic limit (PL) 53%; Plasticity index (PI) 29.8%. The Atterberg test on the lower layer has a liquid limit value (LL) of 79.56%; plastic limit (PL) 43.76%, plasticity index (PI) 35.8%.

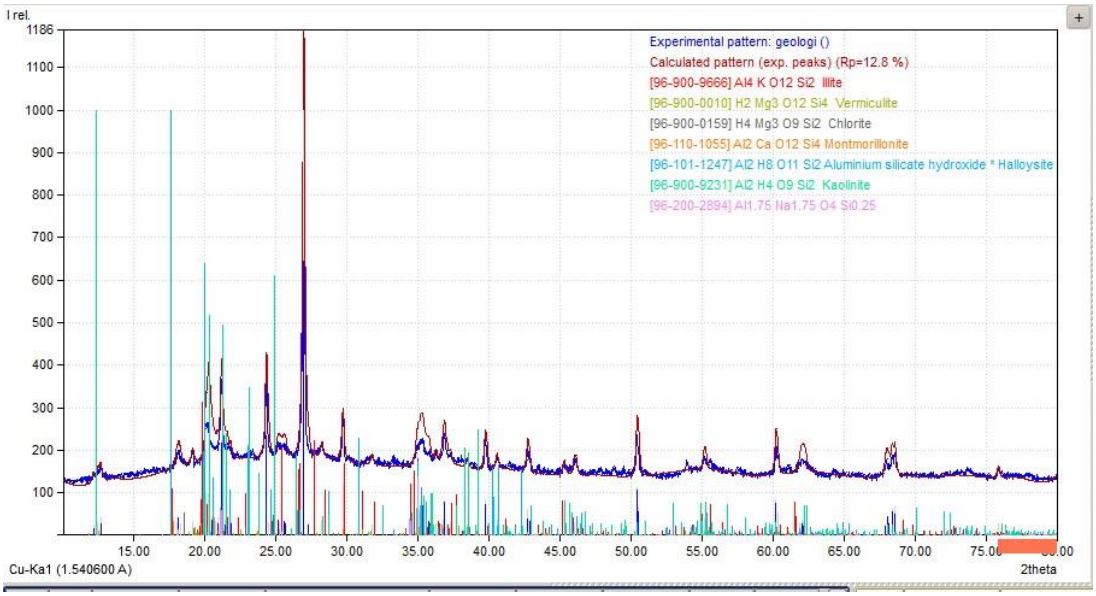


**Figure 4.** Diffractogram the residual soil of the top layer.

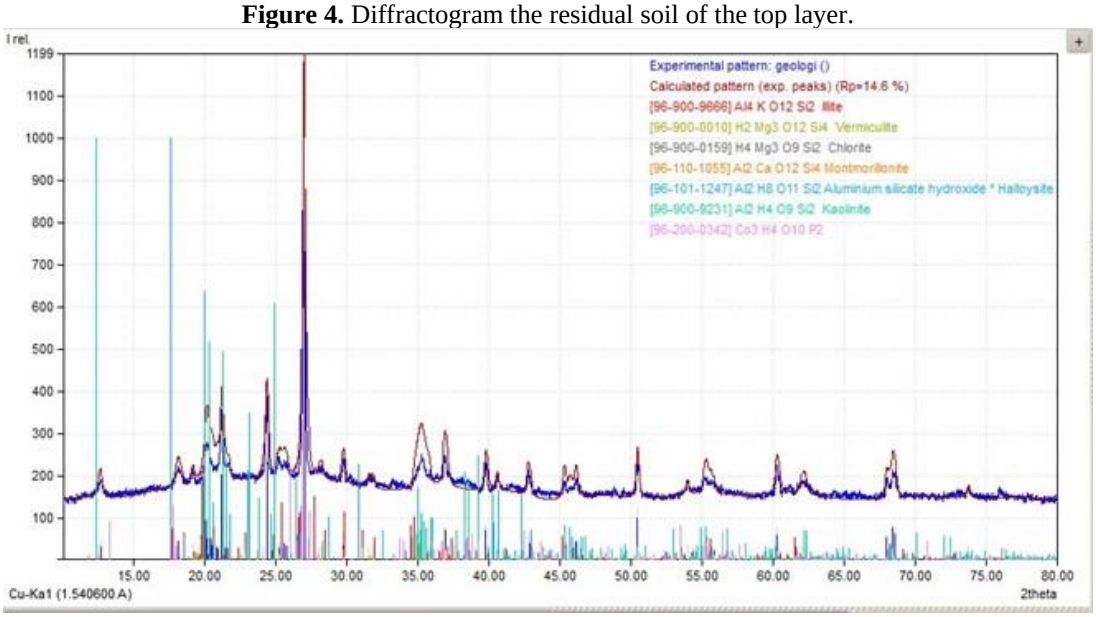


**Figure 5.** Diffractogram the residual soil of the middle layer.

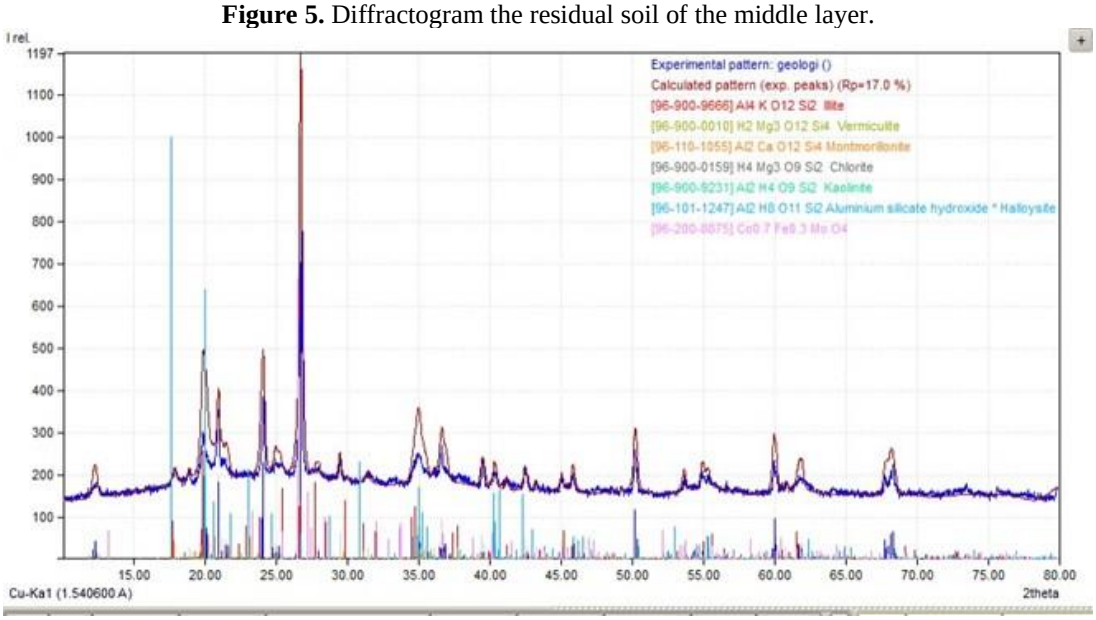


**Figure 6.** Diffractogram the residual soil of the bottom layer.

The results of the calculation of the plasticity index can be concluded that the type of soil found in the study area is clay with high plasticity> 17% (classification of soil types based on high plasticity index, (Chen, 1988; Keskin et al., 2023)). The stability of the soil or rock that forms a downward slope can cause shear stress to develop intensively so that a slip plane is formed (Guo et al., 2023), explains that the movement occurs along the slip plane asynchronously. Rock fractures as the most influential factor in the process of forming the slip plane in these measurements. This can cause weathering that forms soil. Based on the XRD (X-Ray Diffraction) results on the sample, it shows that clay minerals are the dominant soil component so that a layer of clay is formed. The clay layer will be the infiltration boundary (discontinuous plane), which is the areas in the rock layers that are not continuous.

The clay layer can form an impermeable layer that absorbs a lot of water when there is high rainfall. The accumulation of water will cause the clay layer to expand. (Swelling Potential), if evaporation occurs in the dry season, due to reduced water supply, the clay layer becomes dry, so that the soil layer shrinks (Shrinkage Potential), then the material above it is susceptible to shifting.

## Conclusion

The clay minerals contained in the soil with the highest percentage values were Illite ($Al_4KO_{12}Si_2$) 32.3% - 55.6%, Vermiculite ($H_2Mg_3O_{12}$) 14.6% - 22.6%, Montmorillonite ($Al_2CaO_{12}Si_4$) 6.1% - 18.9%. These clay minerals will cause the soil to become expansive; the soil has a plasticity index value of 21.86% - 26.44%, is a high plastic type of soil.

From the observation of the geoelectric stretch, the slip plane is found at the 85th meter to the 43rd meter with a depth of 1 meter to a depth of 2.5 meters to a depth of 20 meters. Curved shape with residual soil (0.1 m - 45.5 m) which is the result of weathering of limestone (100.1 m - 274 m) and remains on top of the parent rock (in situ). Mass movement will occur on a small-scale sliding plane and is actively moving slowly. Such mass movements are categorized into creep types.

## Acknowledgements

This research was assisted by laboratory staff on the Atterberg test which was carried out in the geotechnical laboratory, Civil Department and XRD analysis was carried out in the laboratory of the Department of Geology, Faculty of Engineering, Hasanuddin University, also thanks to the editors and reviewers for help, correction, and suggestion for our manuscript.

## Author Contribution

Ratna Husain designed and conducted all the experiments and wrote the manuscript. All authors have read and approved of the final manuscript.

## Conflict of Interest

The authors declare that they hold no competing interests.

## References

Adam, M., Wang, L., Kheiralla, K., Wadi, D., & Ngata, M.R. (2023). Foundation assessment using integrated geophysical techniques for natural gas pipeline route in Al-Sabaloka area, Sudan. *Arabian Journal of Geosciences*, 16(1), 1–16. https://doi.org/10.1007/s12517-022-11162-7

Almeida, H.D., Marques, M.C.G., Sant'Ovaia, H., Moura, R., & Marques, J.E. (2023). Environmental Impact Assessment of the Subsurface in a Former W-Sn Mine: Integration of Geophysical Methodologies.

*Minerals*, 13(1), 55. https://doi.org/10.3390/min13010055

Amsah, L.O.M.Y. & Umar, E.P. (2020). Identifikasi Zona Mineralisasi Emas Menggunakan Metode Resistivitas dan Induksi Polarisasi (IP) di Desa Lintidu Kabupaten Buol. *Jurnal Geocelebes*, 4(2), 144–149. https://doi.org/10.20956/geocelebes.v4i2.11126

Aryadi, A. (2014). *Identification of the slip plane with the geoelectric method of resistivity in the Gattareng area, Kec. Marioriwawo Kab. Soppeng, South Sulawesi Province*. Universitas Hasanuddin.

Aweda, A.K., Jatau, B.S., Goki, N.G., Bashir, I.Y., & Obaje, N.G. (2023). Application of VES and 2D Resistivity Methods for Groundwater Exploration in Kutigi-Enagi Region, Northern Bida Basin, Nigeria. *Saudi Journal of Engineering and Technology*, 8(2), 29-40. https://doi.org/10.36348/sjet.2023.v08i02.001

Azis, A., Irfan, U.R., & Alimuddin, I. (2023). Geoelectrical resistivity and geochemical method for groundwater investigation in the coastal sediment. *IOP Conference Series: Earth and Environmental Science*, 1134(1), 012020. https://doi.org/10.1088/1755-1315/1134/1/012020

Bamerni, K.D. & Mohammad, R.J. (2023). 2D Resistivity Technique in Exploring Soil Contamination Zones, Kwashe Area, Duhok, North of Iraq. *The Iraqi Geological Journal*, 56(1A), 253–264. https://doi.org/10.46717/igj.56.1A.19ms-2023-1-31

Bundang, S., Massinai, M.F.I., Firman, F., & Hidayat, W. (2022). Subsurface Profile Analysis for Aquifer Layer Identification. *Jurnal Geocelebes*, 6(2), 194–202. https://doi.org/10.20956/geocelebes.v6i2.21911

Chen. F.H. (1988). *Foundation on Expansive Soils*. Elsevier Scientific Publishing, New York.

Dernaika, M.R., Masalmeh, S., Mansour, B., Al Jallad, O., & Koronfol, S. (2023). Modeling Permeability in Different Carbonate Rock Types. *Petrophysics*, 64(01), 18–37. https://doi.org/10.30632/PJV64N1-2023a2

Guo, Z., Huang, Q., Liu, Y., Wang, Q., & Chen, Y. (2023). Model experimental study on the failure mechanisms of a loess-bedrock fill slope induced by rainfall. *Engineering Geology*, 313, 106979. https://doi.org/10.1016/j.enggeo.2022.106979

Husain, R. (2015). *Geochemistry of Clay Mineral and Its Implication Toward landslide*. Hasanuddin University.

Husain, R., Imran, A.M., Irfan, U.R., & Harianto, T. (2015). Nature and Plasticity of Residual Soil in Relation to the Landslide Susceptibility at Marioriwawo, South Sulawesi. *International Journal of Engineering and Science Applications*, 2(1), 61–67. http://pasca.unhas.ac.id/ojs/index.php/ijesca/article/view/148

Keskin, İ., Salimi, M., Ateyşen, E. Ö., Kahraman, S., & Vakili, A.H. (2023). Comparative Study of Swelling Pressure in Expansive Soils considering Different Initial Water Contents and BOFS Stabilization. *Advances in Civil Engineering*, 2023 2023, Article ID 4823843, 11 pages, 2023. https://doi.org/10.1155/2023/4823843

Martorana, R. & Capizzi, P. (2023). Evaluation of Artifacts and Misinterpretation in 2D Electrical Resistivity Tomography Caused by Three-Dimensional Resistive Structures of Regular or Irregular Shapes. *Applied Sciences*, 13(3), 2015. https://doi.org/10.3390/app13032015

Purnamasari, I.N.P., Ipmawan, V.L., & Khairuman, E. (2020). Determination

of Slip Surface Using 2D Geoelectric Resistivity Method and Laboratory Analysis for Landslide Prone Area Pesawaran, Lampung. *IOP Conference Series: Earth and Environmental Science*, 537(1), 012011. https://doi.org/10.1088/1755-1315/537/1/012011

Rahmaniah., Wahyuni, A., Massinai, M.F.I., Mun'im, A., & Massinai, M.A. (2021). Resistivity Method for Characterising Subsurface Layers of Coastal Areas in South Sulawesi, Indonesia. *Journal of Geoscience, Engineering, Environment, and Technology*, 6(4), 217–225. https://doi.org/10.25299/jgeet.2021.6.4.6242

Shanshal, Z. M. & Al-Mashhadany, A. Y. (2023). Detection of Soil Contamination Using Electrical Resistivity Tomography and Induced Polarization Methods by Tank Model. *The Iraqi Geological Journal*, 56(1A), 208–220. https://doi.org/10.46717/igj.56.1A.16ms-2023-1-28

Sudarsono, U. & Hasibuan, G. (2011). Engineering Geological Characteristics of the Residual Soil, Lower Quaternary Sediments in Kertajati Region, Majalengka, West Java. *Indonesian Journal on Geoscience*, 6(3), 177–189. https://doi.org/10.17014/ijog.6.3.177-189

Sukamto R. (1982). *Geologi Lembar Pangkajene dan Watampone Bagian Barat, dan Lembar Ujungpandang, Benteng dan Sinjai*. Pusat Survey Geologi, Direktorat Sumber Daya Energi, Mineral dan Pertambangan, Bandung.

Tejakusuma, G.I. (2020). Determination of Landslide Slip Plane Using Geology and Geoelectrical Analysis at Mount Geger Pulus Legok Emo Slope Segment, Cililin, West Java. *Jurnal Sains dan Teknologi Mitigasi Bencana*, 15(1), 63–73. https://doi.org/10.29122/jstmb.v15i1.4114

Vieira, L.V., Rodrigues, F.H., & Abel, M. (2020). Ontological Analysis of Weathering. *Proceedings of the XIII Seminar on Ontology Research in Brazil and IV Doctoral and Masters Consortium on Ontologies (ONTOBRAS 2020) Vitória, Brazil, November 23-26, 2020*, pp.134–147. https://ceur-ws.org/Vol-2728/paper10.pdf

ISSN: 2579-5821 (Print)
ISSN: 2579-5546 (Online)
URL address: http://journal.unhas.ac.id/index.php/geocelebes
DOI: 10.20956/geocelebes.v7i1.22130

Jurnal Geocelebes Vol. 7 No. 1, April 2023, 37 – 43

# Effect of pH and Surfactant Concentration Sodium Lignosulfonate (SLS) towards Reduction of Silica Mass from Geothermal Brine

M. Ridho Ulya[1]*, Suharmanto[2], Saaduddin[3], Didik Supriyadi[4]

[1]Department of Environtmental Engineering, Faculty of Engineering, Universitas Lampung, Indonesia
[2]Department of Public Health, Faculty of Medicine, Universitas Lampung, Indonesia
[3]Department of Geophysics, Faculty of Mathematics and Natural Sciences, Hasanuddin University, Indonesia
[4]Department of Chemical Engineering, Faculty of Engineering, Institut Teknologi Sumatera, Indonesia

*Corresponding author. Email: m.ridhoulya@eng.unila.ac.id

Manuscript received: 16 August 2022; Received in revised form: 2 December 2022; Accepted: 5 April 2023

**Abstract**

Geothermal energy source is one of the wealth of mineral resources that are being widely used. Geothermal Power Plant is a solution to the needs of New Renewable Energy to overcome energy needs and dependence on renewable energy. However, there were important problems that occurred in the geothermal field, namely the formation of silica scaling in the production pipe causing the brine injection process to be disrupted, the injection process aims to maintain the volume of the geothermal reservoir and maintain the quantity of production steam in the long run. Therefore, controlling silica in the brine injection path in geothermal fields is very much needed. This paper discussed the decrease in silica mass influenced by pH and the addition of Sodium Lignosulfonate (SLS) surfactants that studying the changes in pH (7, 8 and 9), and surfactant concentrations (0.05, 0.15 and 0.30% (w/v)). The results showed that the dissolved silica in the geothermal solution was reduced and could be controlled by the addition of SLS surfactants. The greater the surfactant concentration and pH, the more the mass of silica will be taken. The best conditions are at pH 9 and SLS surfactant concentration 0.30%w/v.

**Keywords**: geothermal; silica scaling; sodium lignosulfonate; surfactant.

**Citation**: Ulya, M.R., Suharmanto., Saaduddin., and Supriyadi, D. (2023). Effect of pH and Surfactant Concentration Sodium Lignosulfonate (SLS) towards Reduction of Silica Mass from Geothermal Brine. *Jurnal Geocelebes*, 7(1):37-43, doi: 10.20956/geocelebes.v7i1.22130

## Introduction

Indonesia is blessed with enormous and diverse potential energy resources. Not only fossil energy but renewable energy potential is also spread throughout Indonesia including geothermal energy. Geothermal as an environmentally friendly and renewable natural resource is one alternative energy source that can be developed to generate electricity and support the growth of electricity development in Indonesia.

One of the power plants that utilize the geothermal potential in Indonesia is PT Geo Dipa Energy Dieng Unit. This Dieng geothermal field production fluid has a high silica content of 440 ppm (Setiawan et al., 2015). The high silica content causes scaling problems both in geothermal steam production wells and in the brine injection pathway, as a result, the injection pipes become clogged and the process of distributing brine to the injection wells is disrupted (Haklidir & Haklidir, 2017; Cano et al., 2022). It can be seen in Figure 1.

The injection process aims to maintain the volume of the geothermal reservoir (Mori et al., 2019) and maintain the quantity of steam production in the long run (Sandoval et al., 2018).

**Figure 1.** Silica scaling on geothermal pipes (Pusat Kajian Sumberdaya Bumi Non-Konvensional, FT UGM)

Thus, it is necessary to reduce the mass of silica to reduce scaling in the injection pipe. One of them is by controlling brine pH (Ikeda & Ueda, 2017) and adding Sodium Lignosulfonate (SLS) surfactants. The addition of surfactants will help to reduce surface tension so that silica can be easily controlled. While the research conducted by Setiawan et al. (2015), only added Calcium hydroxide ($Ca(OH)_2$) compounds without surfactant. This study aims to determine the effect of pH and SLS surfactant concentration on decreasing the mass of silica in the brine. So, there is no need to do continuous pipe cleaning which results in a decrease in the production of geothermal steam.

## Materials and Methods

The material used in this study is ammonium hepta-molybdate ($(NH_4)_6Mo_7O_{24}\bullet_4H_2O$) (Servis et al., 2021). This solution is used as a reagent in the analysis of silica monomer concentrations in brines using UV/Vis spectrophotometry with the yellow molybdate method. Sulfuric acid ($H_2SO_4$) 96% was used as a reagent in the analysis of silica monomer concentrations in brines using UV/Vis spectrophotometry (Ito et al., 2017. $Ca(OH)_2$ is used as a reagent and adjusts the reaction pH.

SLS surfactants are used to reduce surface tension and prevent coagulation in geothermal solutions so that the silica content is easy to control. This surfactant is not obtained through this method but comes from waste empty fruit bunches of oil palm. Utilization This waste is used as a surfactant SLS.

Silica content in the geothermal solution was analyzed using UV-Visible spectrophotometer (Dubey & Bende, 2018). This step is used to determine the level of silica dissolved in the solution taken at certain pH conditions.

UV visible spectrophotometer using absorption of wave radiation ranging from UV light to visible light. Based on this principle, UV-visible spectrophotometers can be used to determine the content of inorganic or organic substances in solution. For the relationship between concentration and absorbance at the wavelength (λ), it is necessary to make a standard solution at various concentrations whose absorbance measurement results are expressed by a calibration curve of the relationship between absorbance (Ab) and concentration (C) (Larson et al., 2018).

The spectrophotometry calibration process needs to be done before measuring the absorbance of the solution. According to Tahir (2008), the calibration process has an important role in providing analysis results with maintained precision and accuracy. The instrument calibration process is carried out using a blank solution. The UV visible spectrophotometer process can be seen in Figure 2.

The surfactant used is a natural surfactant that is widely used in the industry. Lignosulfonate is a water-soluble surfactant so it is widely used as an admixture material, which is to assists the stirring process in the cement mill and makes the building construction more robust because lignosulfonate is also a good binding agent (Fitriani, 2016).

One of the potential natural ingredients for making SLS surfactants is an empty fruit bunch (EFB). This material has the potential to be used as a raw material to produce lignosulfonate surfactants because EFB has a high lignin content (Putri et al., 2019). The molecular structure of SLS can be seen in Figure 3.

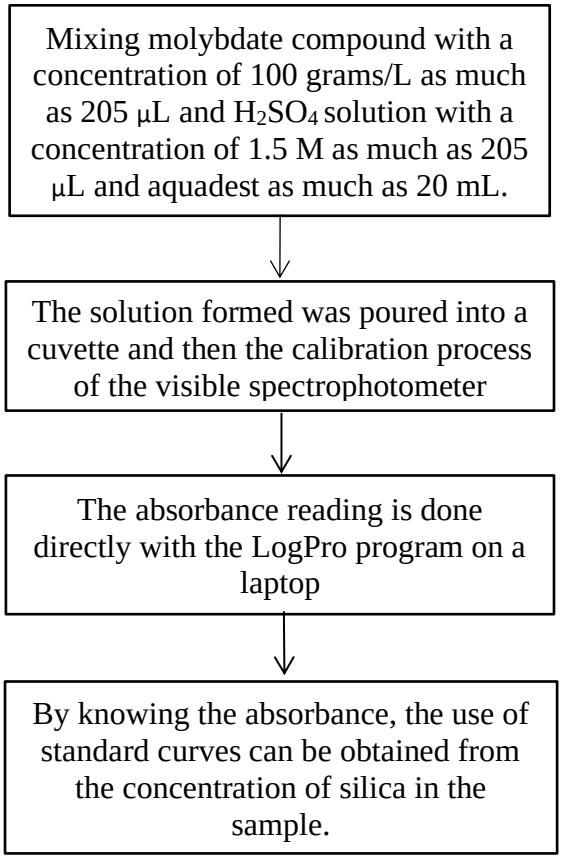


**Figure 2**. The UV visible spectrophotometer process.

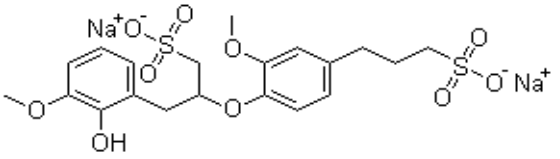


**Figure 3**. Molecular structure of SLS surfactants (Chemblink, MSDS, 2022).

The SLS surfactant molecular structure in Figure 3 shows that SLS is a reaction between sodium bisulfite ($NaHCO_3$) and the lignin molecule, it can be seen from its hydrocarbon chain as a hydrophobic group and $SO_3$ ion as its hydrophilic group. Reactions that occur in the lignin sulfonation process include irreversible and endothermic reactions (Tang et al., 2015). The reaction occurs in a homogeneous phase (Sudarmoyo et al., 2020). Temperature and pH are the most influential factors in the reaction of SLS formation. The higher the acidity, the hydrolysis rate will increase, and the higher the temperature, the reaction rate will be even greater.

The tool used is the hot plate magnetic stirrer, devices are designed in batches equipped with temperature settings and playback scales; the thermometer is mounted on a thermometer to determine the temperature conditions that are set by the temperature control knob. Although there is a temperature control button, researchers still install a thermometer inside the liquid to determine whether the temperature control switch is operating properly and following a predetermined reaction temperature.

In the initial stage, the brine condition is adjusted to the reaction temperature, which is 30$^o$C, so this temperature condition is the optimum condition which shows the lowest silica concentration in the solution (Ulya et al., 2017). After the reaction temperature is reached, the SLS surfactant is added to the concentration adjusted to the concentration of 0.05, 0.15, and 0.30%w/v stirred until homogeneous on a hot plate magnetic stirrer. If the reaction conditions are homogeneous (± for 5 minutes) then base $Ca(OH)_2$ is added to reach pH 7, 8, and 9 conditions using a pH indicator. Because at the pH point conditions the solubility of silica experiences the lowest point in the mother liquor (Eikenberg, 1990). Then from the absorbance obtained it is known that silica is taken by decreasing the amount of silica concentration from the mother liquor.

## Results and Discussion

The mass of silica obtained was then multiplied by the total volume of the solution for each variation of pH and SLS surfactant concentration under the reaction temperature conditions of 30°C. The results obtained can be seen in Figure 4 below.

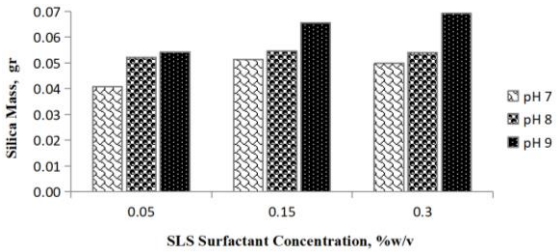


**Figure 4.** Silica Mass and pH at SLS Surfactant Concentrations

The difference in pH and SLS surfactant concentration can affect the amount of mass silica taken (Fig.4). This can be seen at every increase in pH in brine increasing silica mass, as well as the addition of SLS surfactants at every %w/v. When the addition of base $Ca(OH)_2$, Ca compounds can bind Si so that the concentration of silica in the liquid decreases. With the addition of $Ca(OH)_2$ in the geothermal solution, it will decompose into $Ca^{2+}$ ions and $OH^-$ then $Ca^{2+}$ ions will bind Si directly into the micelle and will propagate continuously in the micelle. The formation of this monomer is very dependent on the presence of micelles for the nucleation of the micellar process. The formation of these micelles will continue to experience growth if the SLS surfactant concentration continues to be added until it reaches the saturation point and until the droplet monomers are consumed. At the pH 7 condition with the addition of a 0.05%w/v SLS concentration is the lowest taken silica mass of 0.0408 gr. If this condition is raised to 8 pH, the difference in silica mass taken is 0.0521 gr, more much from pH 8. Similarly, the addition of pH 9 increases the mass of silica that is taken. These results are also consistent with researchers conducted by Eikenberg (1990) with increasing pH the final concentration of silica decreases. So that with the decrease in silica concentration can be seen the mass of silica taken.

Figure 4 shows the change in SLS surfactant concentration which is very significant, as SLS surfactant concentration increases, the mass of silica is also increase. If the mass of silica is converted into the percent of silica taken, then the percent of silica is taken at the best conditions, namely temperature 30°C, pH 9 and the addition of SLS surfactant concentration 0.30%w/v is 11.609%. (Rofi, 2016) using $Ca(OH)_2$ base was only able to take dissolved silica as much as 5.355% at 40°C, pH 9, and without using surfactants.

Differences in SLS surfactant concentrations as dispersing agents also result in differences in the conditions of the geothermal fluid. Ismiyati (2008) suggested that the different in SLS surfactant concentration is very influential on the percentage of flow values obtained to determine the performance of SLS as a dispersing agent. He addition of SLS as a dispersant in a solution causes a decrease in viscosity so that the surface area becomes larger (dispersed). Dispersing agents that work at the interface between two phases will produce an electric barrier to prevent the dispersing of solid particles (Khouw et al., 2021). Therefore, with the increasingly dispersed geothermal solution by SLS surfactants, it is easier to control and even reduce the silica mass (Sudarmoyo et al., 2018).

The influence of SLS surfactants has been investigated by Ulya et al. (2017) by comparing the brine conditions without using surfactants with the addition of SLS surfactants, which shows that in the brine condition without the addition of SLS surfactant at a temperature of 30°C and pH 9, the resulting dissolved silica concentration was 176 ppm. This silica concentration can drop to 156 ppm after adding SLS surfactant with a concentration of 0.05%w/v, then it can go down to 128

ppm after adding SLS surfactant with a concentration of 0.15%w/v. Additional of SLS surfactant with a concentration of 0.30%w/v, the concentration of dissolved silica can drop even further to 119 ppm. With the addition of an SLS surfactant, it was able to reduce the concentration of dissolved silica in the brine. This indicates that the addition of SLS surfactants is very good to do because there are also Na elements from SLS surfactants that can bind silica and can reduce surface tension to prevent coagulation.

## Conclusion

Dissolved silica in the geothermal solution is reduced and can be controlled by the addition of SLS surfactants. The greater the surfactant concentration and pH, the more the mass of silica will be taken. The best conditions were at pH 9 and SLS surfactant concentrations of 0.30%w/v. The addition of base $Ca(OH)_2$ as a pH variable is very influential in decreasing the mass of silica in the geothermal brine. With the addition of $Ca(OH)_2$ in the geothermal solution, it will break down into $Ca^{2+}$ ions and $OH^-$ then $Ca^{2+}$ ions will bind Si causing a decrease in silica mass in the brine. The addition of SLS surfactants is very good to do, because, in addition to being a dispersing agent, SLS surfactants also have the element Na which can bind silica and reduce the mass of silica in the geothermal brine.

## Acknowledgements

Authors thank PT. Geo Dipa Energi Dieng Unit which has helped facilitate research sampling data.

## Author Contribution

MRU led the research and provided the outline of the manuscript. All authors contributed to discussion to form the basis of this paper, and provided feedback on the manuscript.

## Conflict of Interest

The authors declare that they do not have affiliations with or involvement in any institution with either financial or non-financial interest.

## References

Cano, N. A., Céspedes, S., Redondo, J., Foo, G., Jaramillo, D., Martinez, D., Gutiérrez, M., Pataquiba, J., Rojas, J., Cortés, F. B., & Franco, C. A. (2022). Power from Geothermal Resources as a Co-product of the Oil and Gas Industry: A Review. *ACS Omega*, 7(45), 40603–40624. https://doi.org/10.1021/acsomega.2c04374

Chemblink. Material Safety Data Sheet. Accessed on: https://www.chemblink.com/products/8061-51-6.htm, on March 25, 2022.

Dubey, R., & Bende, N., (2018). Estimation of Iron Metal Contents in Natural Samples by UV-Visible Spectrophotometer Method. *World Journal of Pharmaceutical Research*, 7(5): 714-722. https://doi.org/10.20959/wjpr20185-11094

Eikenberg, J. (1990). *On the Problem of Silica Solubility at High* pH. Paul Scherrer Institute. Wurenlingerund Villigen, Germany.

Fitriani. (2016). *Effect of Nyamplung Seed Oil and Co-surfactant Epoxidation on the Performance of Sodium Lignosulfonate (SLS) for Enhanced Oil Recovery (EOR)*. Department of Chemical Engineering. Faculty of Engineering. Universitas Gadjah Mada. Yogyakarta.

Haklidir, F. T. & Haklidir M. (2017). Fuzzy control of calcium carbonate and silica scales in geothermal systems. *Geothermics*, 70: 230-238. https://doi.org/10.1016/j.geothermics.2017.07.003

Ikeda, R. & A. Ueda (2017). Experimental field investigations of inhibitors for controlling silica scale in geothermal brine at the Sumikawa geothermal plant, Akita Prefecture, Japan. *Geothermics*, 70: 305-313. https://doi.org/10.1016/j.geothermics.2017.06.017

Ismiyati. (2008). *The design of the lignin sulfonation process of EFB isolates into sodium lignosulfonate (NLS) surfactant*. Bogor Agricultural Institute. Bogor.

Ito, S., Kasuya, M., Kurihara, K., & Nakagawa, M. (2017). Nanometer-Resolved Fluidity of an Oleophilic Monomer between Silica Surfaces Modified with Fluorinated Monolayers for Nanoimprinting. *ACS Applied Materials & Interfaces*, 9(7): 6591–6598. https://doi.org/10.1021/acsami.6b15139

Khouw, M., Setiati, R., Pramadika, H., & Ridaliali, O. (2021). Analysis of correlation between interfacial tension and salinity in sodium lignosulfonate surfactant. *AIP Conference Proceedings*, 2363(020012). https://doi.org/10.1063/5.0067188

Larson, N. R., Wei, Y., & Middaugh, R. (2018). Label-Free, Direct Measurement of Protein Concentrations in Turbid Solutions with a UV–Visible Integrating Cavity Absorbance Spectrometer. *Analytical Chemistry*, 90(8): 4982–4986. https://doi.org/10.1021/acs.analchem.8b00502

Mori, U., Unami, S., Osaka, Y., Yanaze, T., Yokohama, T., Tsukamoto, K., Kusakabe, M., Marumo, K., & Ueda, A. (2019). Observation of silica nanoparticle growth in saline geothermal brine from the Yamagawa geothermal power station, Japan, using dynamic light scattering. *Geothermics*, 82: 232–242. https://doi.org/10.1016/j.geothermics.2019.06.010

Pusat Kajian Sumberdaya Bumi Non-Konvensional. Fakultas Teknik UGM. Accessed on: https://ugrg.ft.ugm.ac.id/artikel/silica-scaling-sumber-material-dari-limbah-industri-geothermal/ , on Nov 25, 2022.

Putri, N. A., Aziz, M. M., & Purwono, S. (2019). A Comparison of Sodium Lignosulfonate (SLS) Synthesis from Black Liquor Lignin and Commercial Lignin. *Material Science & Engineering*, 948: 206-211. https://doi.org/10.4028/www.scientific.net/MSF.948.206

Rofi, A. F. (2016). *Effect of Temperature and Addition of $Ca(OH)_2$ on Silica Precipitation in Geothermal Fluid Continuous Systems*. Department of Chemical Engineering. Faculty of Engineering. Universitas Gadjah Mada. Yogyakarta.

Sandoval, O. G. M., Trujillo, G. C. D., & Orozco, A. E. L. (2018). Amorphous silica waste from a geothermal central as an adsorption agent of heavy metal ions for the regeneration of industrial pre-treated wastewater. *Water Resources and Industry*, 20: 15–22. https://doi.org/10.1016/j.wri.2018.07.002

Servis, A., Bettinardi, D. J., & Tkac, P. (2021). *Crystallization of Ammonium Heptamolybdate for Reduction to Mo Metal*. United States. https://doi.org/10.2172/1825222

Setiawan, F. A., Pantron, H. P. M., Alfredo, D., Perdana, I. (2015). *Mitigation of Silica Scaling from Dieng's Geothermal Brines using $Ca(OH)_2$*. Proceedings Indonesia International Geothermal Convention &

Exhibition. Jakarta Convention Center. Indonesia.

Sudarmoyo, Widianingsih, I., & Feldza, R. M. (2020). Wettability alteration study in light oil reservoir by sodium lignosulfonate (SLS) as surfactant injection. *AIP Conference Proceedings*, 2245(090001). https://doi.org/10.1063/5.0006995

Sudarmoyo, Swadesi, B., Andini, A. N., Siregar, S., Kurnia, R., Buhari, A., & Budiman, I. G. S. (2018). Wettability alteration study in light oil reservoir by sodium lignosulfonate (SLS) as surfactant injection. *AIP Conference Proceedings*, 1977(030033). https://doi.org/10.1063/1.5042953

Tahir, I. (2008). *Significance of Calibration in Analytical Measurement Processes: Applications in the Use of pH Meters and UV-Vis Spectrophotometers*. Paper Seri Manajemen Laboratorium.

Tang, Q., Zhou, M., Yang, D., & Qiu, X. (2015). Effects of pH on aggregation behavior of sodium lignosulfonate (NaLS) in concentrated solutions. *Journal of Polymer Research*, 22(4): 50. https://doi.org/10.1007/s10965-015-0689-3

Ulya, M. R., Perdana, I. & Mulyono, P. (2017). Effect of Addition of Sodium Lignosulfonate (SLS) Surfactant in the Precipitation Process of Nano Calcium Silicate (NCS) from Geothermal Brine. *Journal of Process Engineering*, 11 (2), 54–61.

ISSN: 2579-5821 (Print)
ISSN: 2579-5546 (Online)
URL address: http://journal.unhas.ac.id/index.php/geocelebes
DOI: 10.20956/geocelebes.v7i1. 23183

Jurnal Geocelebes Vol. 7 No. 1, April 2023, 44 – 52

# Study of Coastline Shifts on the West Coast of Lampung Using Remote Sensing Data

Romi Fadly[1]*, Citra Dewi[1,2], Fajriyanto[1]

[1]Geodesy and Geomatics Engineering, University of Lampung, 35145, Indonesia.
[2]Doctoral Programme of Environmental Sciences, University of Lampung, 35145, Indonesia.

*Corresponding author. Email: romi.fadly@eng.unila.ac.id

Manuscript received: 25 September 2022; Received in revised form: 6 April 2023; Accepted: 27 April 2023

**Abstract**

This study specifically aims to identify coastal abrasion as seen from the coastline shift, from 1989 to 2020 in Pesisir Utara Sub-district and Lemong Sub-district, Pesisir Barat Regency, Lampung Province, by interpreting remote sensing data. The data used are Landsat satellite imagery for 1989, 2000, 2006, and 2020. Landsat satellite imagery are corrected by radiometric and geometric correction. The geometric correction is registered to Landsat imagery in 1989. The corrected satellite imagery is digitized for the coastline. The results of the digitized coastline were then overlaid, then the coastline shift was calculated from 1989 to 2020. The coastline shift calculation was carried out at 16 locations in Pesisir Utara Sub-district and Lemong Sub-district. The results of calculations at 16 sample locations show that there has been a shift in the coastline due to coastal abrasion from 1989 to 2020 of 2.0 m/yr. For areas where the coastal conditions are rocky and there are shallow rocks in front of it, the coastline shift is only small, such as in the cape area before Walur Village. This coastline shift was also evidenced by direct checking of the area and asking local residents, the results showed that the overall shift of the coastline was caused by coastal abrasion.

**Keywords**: abrasion; coastal; geometric correction; landsat.

**Citation**: Fadly, R., Dewi, C. and Fajriyanto. (2023). Study of Coastline Shifts on the West Coast of Lampung Using Remote Sensing Data. *Jurnal Geocelebes,* 7(1): 44–52, doi: 10.20956/geocelebes.v7i1.23183

## Introduction

The coastline is the meeting line between sea water and land whose position changes according to the position during tides, the influence of waves and ocean currents (Setiyarso et al., 2016; Yasir et al., 2021). Coastline changes are sometimes caused by social and natural factors, such as human activities in the coastal zone, long-term and short-term sea level changes, storm events, subsequent recovery, and so on (Alimuddin & Aryanti, 2020; Suniada, 2015; Wang et al., 2017; Xu, 2018). Changes in the coastal environment can occur slowly to quickly, depending on the power balance between topography, rocks and their properties with waves, tides and wind (Harianja et al., 2019). Accretion and abrasion of Coastal occur due to the input of sediment from the mainland to the coastal area and the influence of hydro-oceanographic factors in the form of waves and currents that carry sediment (Astuti et al., 2021; Fuad et al., 2019; Wang et al., 2017). The process of accretion and abrasion results in unbalanced coastal conditions and impacts on coastal areas.

The following are some studies related to coastline changes. The coastline change that occurred in Gianyar Regency based on SPOT satellite imagery in 2009 and 2015 was 22,441 m. The average rate of coastal erosion that occurred in Gianyar Regency based on SPOT satellite images in 2009 and 2015 was 3,202 m/yr (Aryastana et al., 2016). Most of the changes in the coastline in Kendal Regency occurred in the bay area and along the headland, during the period

1972 to 1991 there were abrasion and accretion covering 765.14 acres and 356 acres (Arief et al., 2011). The coastline in Bentenan Village, Pusomaen District, Minahasa Tenggara experienced an average change of 165 m towards the mainland in the period 1985-2008 (Opa, 2011).

The coastal area in Pesisir Utara Sub-district and Lemong Sub-district, Pesisir Barat Regency is a coastal area located on the West Coast of Lampung Province. The geographical condition of the coast of Pesisir Barat Regency which is directly facing the Indian Ocean and the absence of small islands as natural breakwaters, has caused many coastal areas in the Pesisir Barat Regency to experiencing abrasion which has resulted in changes in the coastline. From direct observation in the field, many coastal areas in the Pesisir Barat District experienced abrasion (Fig. 1 to 3) which causes coastline shift. The protection of the coastal areas of the Pesisir Barat Regency requires careful planning. In planning for the development of coastal protection, supporting data will be needed, one of which is the coastline shift. In addition to direct monitoring in the field, another method that can be used to monitor coastline shift due to abrasion is the interpretation of remote sensing data, field monitoring is only to check the results of the interpretation. The development of remote sensing technology is currently leading to an increase in spatial and temporal resolution for information acquisition and monitoring purposes (Lubis D et al., 2017). At present the use of remote sensing image datasets such as Landsat and geographic information systems (GIS) plays a very important role as a cheap and easy method of providing coverage data on coastal areas and the dynamics therein (Avtar et al., 2020; Kasim, 2012).

The aim of this study is to identify coastal abrasion as seen from the coastline shift from 1989 to 2020 in Pesisir Utara Sub-district and Lemong Sub-district, Pesisir Barat Regency, Lampung Province, by interpreting remote sensing data.

**Figure 1.** The condition of the west cross road in Lemong Sub-district has been affected by abrasion.

**Figure 2.** The condition of the coast behind SMAN 1 Lemong.

**Figure 3.** The condition of the coast behind Balam Village.

## Materials and Methods

The location of the study will be specifically on coastal sections, which have experienced abrasion, starting from the Lemong Sub-district to the Pesisir Utara Sub-district in Balam Village, Pesisir Barat Regency, Lampung Province (Fig.4).

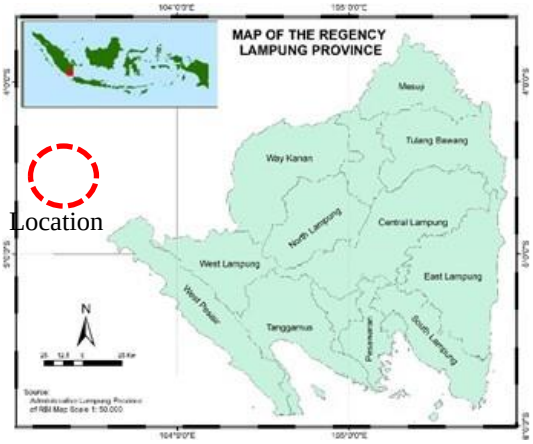


**Figure 4.** Map of the research sites in the West Pesisir Regency (Balai Pelaksanaan Jalan Nasional Lampung, in Sulistyorini, 2021).

The expected result of this research is the rate of coastline change due to coastal abrasion. The satellite imagery used in this study are Landsat TM Satellite Imagery recorded in 1989, Landsat ETM+ Satellite Imagery recorded in 2000, Landsat 7 ETM+ Satellite Imagery recorded in 2006, and Landsat 8 Satellite Imagery recorded in 2020, as well as visual data obtained with direct observation of the field. The method of implementing this research consists of several stages: Collection of Landsat imagery; Landsat satellite imagery correction process; Digitizing the coastline on each Landsat satellite imagery; Analysis of coastline changes.

The flowchart of the research implementation can be seen in Fig. 5. The results of this study were maps of the coastlines for 1989, 2000, 2006, and 2020, along with their shift values from every year. The satellite imagery data used are Landsat satellite imagery for 1989, 2000, 2006 and 2020. These Landsat imagery can be downloaded for free on the web page: https://earthexplorer.usgs.gov/ (Achoh et al., 2021).

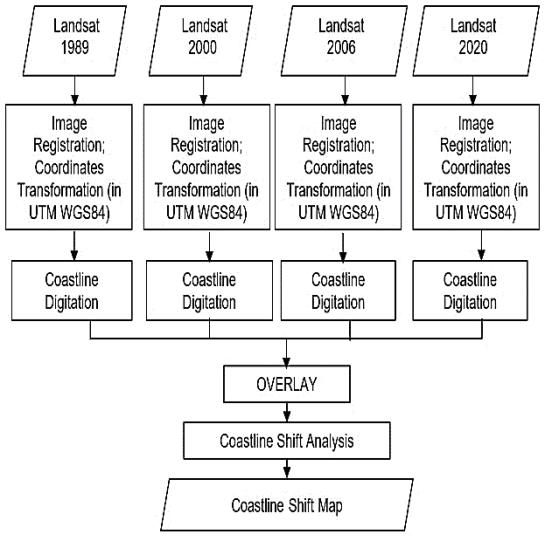


**Figure 5.** Flowchart of research implementation

*Image Enhancement*

Image enhancement is carried out in several stages:

1. Create RGB displays on Landsat imagery for each year (1989, 2000, 2006, and 2020) with the aim of adjusting the brightness of the color pixels in the image. Fig. 6 shows each satellite image after sharpening.
2. Improving image quality by adjusting the RGB histogram to achieve the image quality we want.

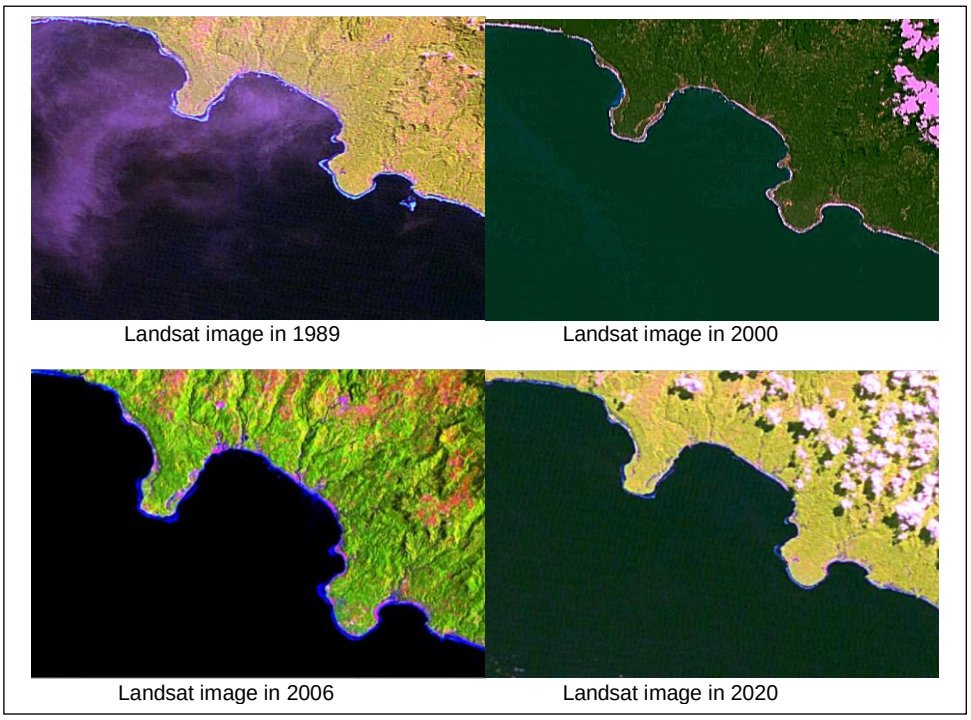


**Figure 6.** Satellite imagery after enhancement (in 1989, 2000, 2006 and, 2020).

*Geometric Correction*

The geometric correction is carried out by registering the 2000, 2006, and 2020 satellites to the 1989 image. The image registration steps are carried out by: Identification of allied points (GCP) and check points. GCPs coordinates are in the form of field observation coordinates with GPS; Digital image processing using the rectification method (Shawal et al., 2014), in this process coordinate transformation is carried out using: the UTM (Universal Transverse Mercator) projection system which refers to the World Geodetic System 1984 reference ellipsoid (ICAO, 2002). The chosen transformation method is polynomial. The geometric correction is carried out using ground control points (image to map rectification).

The results of geometric correction need to be seen for their accuracy. Accuracy is the degree of closeness or accuracy of an information that is on a map or in a digital database with the actual value (Thurston et al., 2003). The magnitude of the error is indicated by the RMSe (root mean square error) value (Chai & Draxler, 2014). RMSe is the value of the difference between the actual value and the measured value (Chai & Draxler, 2014). The greater the RMSe value, the greater the error value of the measurement results against the actual conditions (Simbolon et al., 2017). Here is the formula for calculating RMSe.

$$RMSe = \sqrt{(RMSx)^2 + (RMSy)^2} \quad (1)$$

$$RMSx = \sqrt{\sum Dx^2/n} \quad (2)$$

$$RMSx = \sqrt{\sum Dy^2/n} \quad (3)$$

$$\sum Dx^2 = {dx_1}^2 + {dx_2}^2 + \cdots {dx_n}^2 \quad (4)$$

$$\sum Dy^2 = {dy_1}^2 + {dy_2}^2 + \cdots {dx_n}^2 \quad (5)$$

Satellite imagery contain various geometric distortions that must be corrected. This distortion is generated by factors such as variations in the height of the satellite, the verticality of the satellite and its speed. Random distortions and complex systematic distributions are corrected using field tie point analysis. GCP is an appearance whose location is known and its position can be precisely determined on satellite imagery. A good appearance as a tie point, among others, the intersection of highways, rivers and so on. In the correction process, a large number of tie points are placed according to the image coordinates and field coordinates, the coordinate values are then used for the least quadrant analysis (Lillesand & Kieffer, 1997).

*Coastline Digitization*

The sharpened and geometric corrected imagery are then exported to the Quantum GIS application program. The corrected Landsat satellite imagery for 1989, 2000, 2006 and 2020 were then digitized for the coastline. Digitization is done by on screening. The result of this digitization is then the calculation of the coastline shift with the initial reference to the 1989 image. The digitized coastline of each Landsat image can be seen in Fig. 7. There are 16 (sixteen) locations where the coastline shift is calculated, which are 3 locations in Balam Village, 4 locations in Kerbang Dalam, 2 locations in Kuripan Village, 3 locations in Walur Village, and 4 locations in Penengahan Village. These locations were chosen because the soil structure is sandy beaches which are prone to abrasion due to natural phenomena.

*Coastline Shift Analysis*

Coastline shift were calculated from 1989-2020, 1989-2006, 1989-2000, and 2006-2020, using the Euclidean Distance Method as follows (Mustofa & Suasana, 2020; Pamungkas, 2019)

$$D = \sqrt{(X_{th\ n+1} - X_{th\ n})^2 + (Y_{th\ n+1} - Y_{th\ n})^2} \quad (6)$$

where the value of D is the shift, $X/Y_{(th\ n+1)}$ is value of x/y years to n+1, $X/Y_{(th\ n)}$ is value of x/y years to n.


**Figure 7**. Digitized coastline results from Landsat satellite imagery.

## Results and Discussion

The results of geometric correction using the registration method have an accuracy of range (RMSE) below 2 meters, with a pixel resolution of 30m Landsat satellite imagery, so the accuracy is still below 1 pixel, which is 30 m.

*Coastline Shift Calculation*

The sixteen locations whose coastline shift values were calculated can be presented in Fig. 8 to 13, while the results of the coastline shift calculation from 1989 to 2020 can be seen in Table 1.

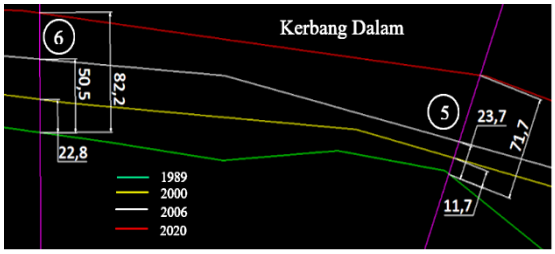


**Figure 10.** Coastline shift on location 5 and 6.


**Figure 11.** Coastline shift on location 7 – 9.

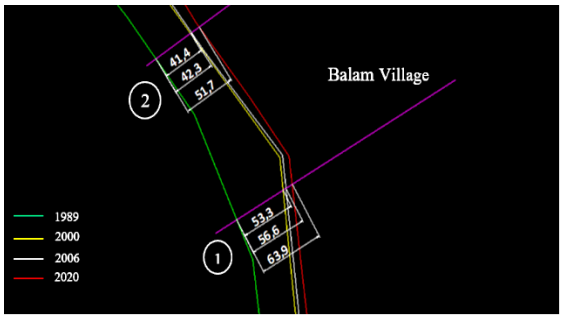


**Figure 8.** Coastline shift on location 1 and 2.

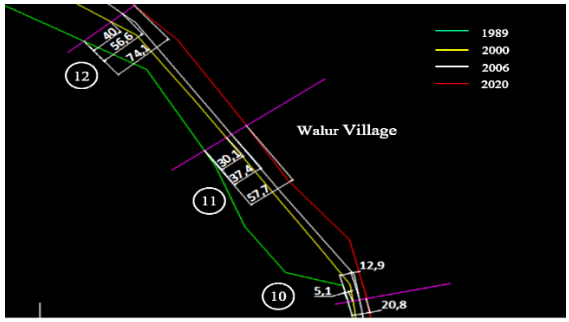


**Figure 12.** Coastline shift on location 10 – 12.

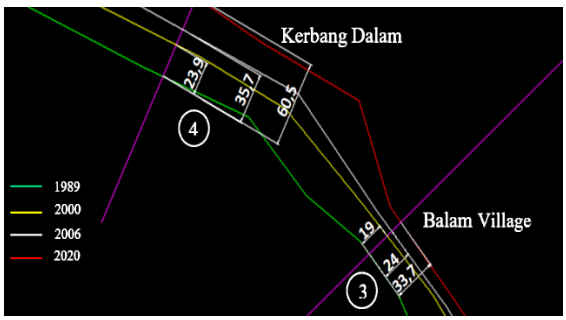


**Figure 9.** Coastline shift on location 3 and 4.

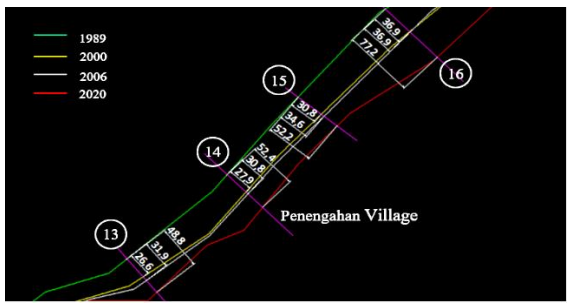


**Figure 13.** Coastline shift on location 13 – 16.

**Table 1.** The results of calculating coastline shift.

| No | 1989-2020 | | 1989-2006 | | 1989-2000 | | 2000-2006 | | 2006-2020 | | Avrg. | Location |
|---|---|---|---|---|---|---|---|---|---|---|---|---|
| | Dist. (m) | Shift m/yr | Dist. (m) | Shift m/yr | Dist. (m) | Shift m/yr | Dist. (m) | Shift m/yr | Dist. (m) | Shift m/yr | Shift m/yr | |
| 1 | 63.9 | 2.1 | 56.6 | 3.3 | 53.2 | 4.8 | 3.4 | 0.6 | 7.3 | 0.5 | 2.1 | Balam |
| 2 | 51.7 | 1.7 | 42.3 | 2.5 | 41.5 | 3.8 | 0.8 | 0.1 | 9.4 | 0.7 | 1.7 | Balam |
| 3 | 33.7 | 1.1 | 24 | 1.4 | 19 | 1.7 | 5.0 | 0.8 | 9.7 | 0.7 | 1.1 | Balam |
| 4 | 60.5 | 2.0 | 35.7 | 2.1 | 23.9 | 2.2 | 11.8 | 2.0 | 24.8 | 1.8 | 2.0 | Krb.Dalam |
| 5 | 71.7 | 2.3 | 23.6 | 1.4 | 11.6 | 1.1 | 12.0 | 2.0 | 48.1 | 3.4 | 2.3 | Krb.Dalam |
| 6 | 82.2 | 2.7 | 50.5 | 3.0 | 22.8 | 2.1 | 27.7 | 4.6 | 31.7 | 2.3 | 2.7 | Krb.Dalam |
| 7 | 87.7 | 2.8 | 55.4 | 3.3 | 25.1 | 2.3 | 30.3 | 5.1 | 32.3 | 2.3 | 2.8 | Krb.Dalam |
| 8 | 90.3 | 2.9 | 50.5 | 3.0 | 31.7 | 2.9 | 18.8 | 3.1 | 39.8 | 2.8 | 2.9 | Kuripan |
| 9 | 45.3 | 1.5 | 22.2 | 1.3 | 13.2 | 1.2 | 9.0 | 1.5 | 23.1 | 1.7 | 1.5 | Kuripan |
| 10 | 20.8 | 0.7 | 12.9 | 0.8 | 5.1 | 0.5 | 7.8 | 1.3 | 7.9 | 0.6 | 0.7 | Walur |
| 11 | 57.9 | 1.9 | 37.4 | 2.2 | 30 | 2.7 | 7.4 | 1.2 | 20.5 | 1.5 | 1.9 | Walur |
| 12 | 74.1 | 2.4 | 56.7 | 3.3 | 39.9 | 3.6 | 16.8 | 2.8 | 17.4 | 1.2 | 2.4 | Walur |
| 13 | 48.8 | 1.6 | 31.9 | 1.9 | 26.6 | 2.4 | 5.3 | 0.9 | 16.9 | 1.2 | 1.6 | Penengahan |
| 14 | 52.4 | 1.7 | 30.8 | 1.8 | 27.9 | 2.5 | 2.9 | 0.5 | 21.6 | 1.5 | 1.7 | Penengahan |
| 15 | 52.2 | 1.7 | 34.6 | 2.0 | 30.8 | 2.8 | 3.8 | 0.6 | 17.6 | 1.3 | 1.7 | Penengahan |
| 16 | 77.2 | 2.5 | 36.9 | 2.2 | 36.9 | 3.4 | 0.0 | 0.0 | 40.3 | 2.9 | 2.5 | Penengahan |
| | **Average** | | | | **27.5** | **2.5** | **10.2** | **1.7** | **23.0** | **1.6** | **2.0** | |

From Table 1 there are several things that can be discussed, related to the coastline shifts that occur:

1. The greatest shift occurred between 1989 and 2000 with an average shift for 16 locations of 2.5 m/yr, then in the period 2000 to 2006, there was a decrease in coastline shift, which is an average for 16 locations of 1.7 m/yr. Furthermore, in the range of 2006 to 2020 there was an increase in the shift of the coastline again, which is with an average shift for 16 locations of 1.6 m/yr.
2. Overall, the magnitude of the average coastline shift from 1989 to 2020 for 16 locations was 2.0 m/yr, with the largest shift occurring in the Kuripan area of 2.9 m/year, while the smallest shift occurred at the Walur Village location that is equal to 0.7 m/yr.
3. The results of this analysis were also proven by asking directly to the elders in the Balam Village area that before 2000 the village road (Fig. 14) was on the talud that was built, whereas currently it is being moved in front towards the land about 50 meters from the talud (Fig. 15).

The local residents also said that from the talud that was visible (Fig. 14) previously there were about 5 rows of coconut trees towards the beach which have now been lost due to abrasion. From the results of the coastline shift analysis, there was a shift from 1989 to 2020 of 42.3 m, if the distance between coconut trees is ± 8 m, then for 5 rows of coconut trees there is a distance of ± 40 m, so the results of analysis using remote sensing data are not significantly different.

**Figure 14.** Condition of the coast in 2020 at Balam Village, at first it was a village road.

**Figure 15.** The condition of the village road was moved about 50 m from the beach.

At the end of the village of Balam Village it can also be seen (Fig. 16) that the condition of the ditch installed has been

destroyed by coastal abrasion, so it is necessary to find a suitable construction solution to tackle coastal abrasion.


**Figure 16.** The Beach conditions at the end of Balam village.

In the Kuripan village area (Fig. 17), it was once a village, but now it no longer exists and has been moved about 2 km from the beach. The results of the analysis used Landsat imagery from 1989 to 2020, there was a shift of 45.3 to 90.3 m.

**Figure 17.** The condition of the village was lost due to coastal abrasion in the Kuripan village.

The results of direct observations in the field show that the condition of the coast is sloping with a stretch of coast in the form of sand and no coast resistance, only in the form of shrubs, this situation allows large abrasion to occur. There needs to be special handling for this kind of area, so that coastal erosion can be controlled.

## Conclusion

Based on the results and discussion there are several conclusions that can be drawn; The first, the geographical conditions of the Pesisir Barat District facing the Indian Ocean with no islands as break water, especially Pesisir Utara and Lemong Sub-districts experienced coastline shift from 1989 to 2020 an average of 2.0 m/yr. The biggest shift occurred in Kuripan Village, which was 2.9 m from 1989 to 2020. Second, for the cape area before the Walur Village the coastline shift is only small, this is because the cape area has a rocky hillside, and in front of the cape there is a natural break water in the form of shallow coral, so the incoming waves are broken up first by the shallow reef. Third, from the results of this study it can also be concluded that remote sensing data is very supportive for making maps of coastline shifts, rapidly and low cost, and if using satellite imagery with better resolution such as GeoEye imagery (0.5 m resolution) it will a more accurate map of coastline shifts can be made.

The last, the average coastline shift of 2.0 m/year can be input for the local government to prevent even greater coastline shifts. Almost along the coast of Pesisir Barat Regency, Lampung Province, has great tourism potential, If it is managed properly, this tourism potential can bring large income to local government.

## Acknowledgements

Many thanks to the Faculty of Engineering-University of Lampung. Acknowledgments are also to residents in the Pesisir Utara Sub-district and Lemong Sub-district who have helped provide information in the field.

## Author Contribution

**Romi Fadly**: Concept and designed the analysis, collected the data, contributed data or analysis tools, performed the analysis, wrote the paper; **Citra Dewi**: Concept and designed the analysis, collected the data, contributed data or analysis tools, performed the analysis, wrote the paper; **Fajriyanto**: Collected the data, contributed data or analysis tools, wrote the paper.

## Conflict of Interest

The authors declare there is no conflict of interest with anyone.

## References


Achoh, M. E., Agadjihouédé, H., Gangbè, L., Aïzonou, R., Akotossodé, C. C., Montcho, S. A., & Chikou, A. (2021). Dynamics of Land Use in the Basin of Ancient Lagoons (Toho, Todougba, Ahouangan, Dati, Djonou) in South Benin from 1990 to 2020 and Their Current Vulnerability to Pollution. *Journal of Geoscience and Environment Protection*, *09*(11), 28–45. https://doi.org/10.4236/gep.2021.911003

Alimuddin, A., & Aryanti, D. (2020). Kajian Perubahan Garis Pantai Muara Gembong, Bekasi. *Rona Teknik Pertanian*, *13*(2), 71–83. https://doi.org/10.17969/rtp.v13i2.17620

Arief, M., Winarso, G., & Prayogo, T. (2011). Kajian Perubahan Garis Pantai Menggunakan Data Satelit Landsat Di Kabupaten Kendal. *Penginderaan Jauh*, *8*, 71–80. https://jurnal.lapan.go.id/index.php/jurnal_inderaja/article/view/1614

Aryastana, P., Eryani, I. G. A. P., & Candrayana, K. W. (2016). Perubahan Garis Pantai Dengan Citra Satelit Di Kabupaten Gianyar. *Paduraksa*, 5(2), 70–81. https://www.ejournal.warmadewa.ac.id/index.php/paduraksa/article/view/379

Astuti, B. I. D., Laksono, A., Muhammad, D. T. N., Nurbaiti, I. F., Hanifah, N. N., Wildiyanti, O. S., Junaedi, R. N., & Marfai, M. A. (2021). Dinamika perubahan garis pantai Kabupaten Kendal tahun 2000-2020. *Majalah Geografi Indonesia*, *35*(1), 75. https://doi.org/10.22146/mgi.62301

Avtar, R., Komolafe, A. A., Kouser, A., Singh, D., Yunus, A. P., Dou, J., Kumar, P., Gupta, R. D., Johnson, B. A., Thu Minh, H. V., Aggarwal, A. K., & Kurniawan, T. A. (2020). Assessing sustainable development prospects through remote sensing: A review. *Remote Sensing Applications: Society and Environment*, *20*. https://doi.org/10.1016/J.RSASE.2020.100402

Chai, T., & Draxler, R. R. (2014). Root mean square error (RMSE) or mean absolute error (MAE)? -Arguments against avoiding RMSE in the literature. *Geoscientific Model Development*, *7*(3), 1247–1250. https://doi.org/10.5194/gmd-7-1247-2014

Fuad, M. A. Z., Yunita, N., Kasitowati, R. D., Hidayati, N., & Sartimbul., A. (2019). Pemantauan Perubahan Garis Pantai Jangka Panjang dengan Teknologi Geo-Spasial di Pesisir Bagian Barat Kabupaten Tuban, Jawa Timur. *Jurnal Geografi*, *11*(1), 48–61. https://doi.org/10.24114/jg.v11i1.11409

Harianja, F. K., Awaluddin, M., & Sudarsono, B. (2019). Analisis Pengaruh Perubahan Garis Pantai Terhadap Batas Pengelolaan Wilayah Laut Daerah Provinsi Sumatera Utara Menggunakan Citra Landsat. *Jurnal Geodesi Undip*, *8*, 205–214. https://ejournal3.undip.ac.id/index.php/geodesi/article/view/25159

ICAO. (2002). *World Geodetic System - 1984 (WGS-84) Manual* (2nd ed., Vol. 1). The Secretary General International Civil Aviation Organization. https://skybrary.aero/articles/world-geodetic-system-1984-wgs84

Kasim, F. (2012). Pendekatan Beberapa Metode dalam Monitoring Perubahan Garis Pantai Menggunakan Dataset Penginderaan Jauh Landsat dan SIG. *Jurnal Ilmiah Agropolitan*, *5*(1), 620–635.

Lillesand, & Kieffer. (1997). *Pengindera-*

*an Jauh dan Interpretasi Citra*. Gadjah Mada University Press.

Lubis, D., Pinem M., & Simajuntak M. A. N. (2017). Analisis Perubahan Garis Pantai Dengan Menggunakan Citra Penginderaan Jauh (Studi Kasus Di Kecamatan Talawi Kabupaten Batubara). *Jurnal Geografi*, *9*(1), 21–31. http://jurnal.unimed.ac.id/2012/index.php/geo

Mustofa, Z., & Suasana, I. S. (2020). Algoritma Clustering K-Medoids Pada E-Government Bidang Information and Communication Technology dalam Penentuan Status Edgi. *Jurnal Teknologi Informasi Dan Komunikasi*, *9*(1), 1–10. https://doi.org/10.51903/jtikp.v9i1.162

Opa, E. T. (2011). Perubahan Garis Pantai Desa Bentenan Kecamatan Pusomaen, Minahasa Tenggara. *Jurnal Perikanan Dan Kelautan Tropis*, *7*(3), 109. https://doi.org/10.35800/jpkt.7.3.2011.187

Pamungkas, C. A. (2019). Longitude Dengan Metode Euclidean Distance. *Jurnal INFORMA Politeknik Indonusa Surakarta*, *5*, 8–13. http://informa.poltekindonusa.ac.id/index.php/informa/article/view/74/68

Setiyarso, B., Muryani, C., & Sarwono. (2016). Analisis Perubahan Garis Pantai Dan Perubahan Penggunaan Lahan Kabupaten Rembang Tahun 2003 - 2014. *GeoEco*, *2*(1), 67–79. https://jurnal.uns.ac.id/GeoEco/article/view/8954

Shawal, S., Shoyab, M., & Begum, S. (2014). Fundamentals of Digital Image Processing and Basic Concept of Classification. *International Journal of Chemical and Process Engineering Research*, *1*(6), 98–108. https://doi.org/10.18488/journal.65/2014.1.6/65.6.98.108

Simbolon, A. B. S., Yuwono, B. D., & Amarrohman, F. J. (2017). Analisis Perbandingan Ketelitian Metode Registrasi Antara Metode Kombinasi Dan Metode Traverse Dengan Menggunakan Terrestrial Laser Scanner Dalam Pemodelan Objek 3 Dimensi. *Jurnal Geodesi Undip*, *6*(4), 285–294. https://ejournal3.undip.ac.id/index.php/geodesi/article/view/18153

Sulistyorini, R. (2021). Peran Infrastruktur Transportasi Dalam Pengembangan Provinsi Lampung. *Jurnal Transportasi*, *21*(1), 55–62. https://doi.org/10.26593/jtrans.v21i1.4829.55-62

Suniada, K. I. (2015). Deteksi Perubahan Garis Pantai Di Kabupaten Jembrana Bali Dengan Menggunakan Teknologi Penginderaan Jauh. *Jurnal Kelautan Nasional*, *10*(1), 13–19. http://ejournal-balitbang.kkp.go.id/index.php/jkn/article/view/8

Thurston. J., Poiker, T. K., & Moore, J. P. (2003). *Integrated Geospatial Technologies. A Guide to GPS: GIS and Data Logging*. John Willey & Sons, Inc.

Wang, X., Liu, Y., Ling, F., Liu, Y., & Fang, F. (2017). Spatio-temporal change detection of Ningbo coastline using landsat time-series images during 1976-2015. *ISPRS International Journal of Geo-Information*, *6*(3). https://doi.org/10.3390/ijgi6030068

Xu, N. (2018). Detecting coastline change with all available landsat data over 1986-2015: A case study for the state of Texas, USA. *Atmosphere*, *9*(3). https://doi.org/10.3390/atmos9030107

Yasir, M., Hui, S., Hongxia, Z., Hossain, M. S., Fan, H., Zhang, L., & Jixiang, Z. (2021). A Spatiotemporal change detection analysis of coastline data in Qingdao, East China. *Scientific Programming*, *2021*. https://doi.org/10.1155/2021/6632450

ISSN: 2579-5821 (Print)
ISSN: 2579-5546 (Online)
URL address: http://journal.unhas.ac.id/index.php/geocelebes
DOI: 10.20956/geocelebes.v7i1.23196

Jurnal Geocelebes Vol. 7 No. 1, April 2023, 53 – 63

# A Study of The Density of Built-Up Land Based on Aerial Photographs in Pasaran Island, Bandar Lampung

Rahma Anisa*, Suyadi

Departement of Geodetic and Geomatics Engineering, University Lampung, 35145, Indonesia.

*Corresponding author. Email: rahma.anisa@eng.unila.ac.id

Manuscript received: 26 September 2022; Received in revised form: 8 April 2023; Accepted: 28 April 2023

**Abstract**

Pasaran Island is a small island connected to the mainland island of Sumatra and located in Bandar Lampung. Pasaran Island is one of the supports for the economy in Bandar Lampung. This is in line with the 2011-2030 RTRW of Bandar Lampung as a strategic minapolitan area (Pasaran and Lempasing) in driving the regional economy and utilizing appropriate technology. Pasaran Island is dominated by fishing villages and seafood processing centers in Lampung. With a population of ± 1,233 people in an area of ± 12 Ha, Pasaran Island has the potential for continued development. A study of the density of Built-up Land on Pasaran Island needs to be carried out so that it can become important information and data in managing the development of Pasaran Island in the future. Remote sensing technology using UAV was carried out to retrieve accurate and precise large-scale mapping information that allows the level of detail of Built-up Land to be mapped according to the original conditions in the field. In this study, the data used to extract Built-up Land was orthophoto which was produced through visual interpretation methods, and to determine the level of density and efficiency of Built-up Land conditions the digitization method and spatial analysis was by calculating the area of Built-up Land and calculating the percentage of Built-up Land density in Pasaran Island. The results of this study consisted of two maps, which are a map of the classification of Built-up and Non-Built-up Land and a map of Built-up Land types. The percentage of Built-up Land density was obtained from the calculation of the area of Built-up Land classes divided by the area of Pasaran Island, which resulted in a built-up density of 87.15% consisting of building classes, open land, public facilities, and road networks. As for the results of the non-built density was 12.84%, which consisted of a vegetation class where the vegetation is in the tree-shaped form, the population density and building density of Pasaran Island are low density.

**Keywords**: Pasaran Island; Built-up Land; UAV; Orthophoto.

**Citation**: Anisa, R. and Suyadi. (2023). A Study of density of Builts-Up Land Based on Aerial Photograps in Pasaran Island Bandar Lampung. *Jurnal Geocelebes*, 7(1): 53–63, doi: 10.20956/geocelebes.v7i1.23196

## Introduction

The addition of urban infrastructure is one indicator of the progress of an area. The phenomenon of growth and development of an area that is not planned is experienced by several cities. There are several factors that underlie the development of an area, such as the rapid growth of the population and the soaring economic growth, of course, both have an impact on the need for a space, land and infrastructure for various community activities and the need to have a place to live. A study conducted by Webster (2002) states that the factor that causes rapid growth in a city is the addition of residential areas as a place for various human activities such as the demand for housing development, industry, and other activities.

Along with the development of cities in Indonesia occurs based on the desire for the availability of land use that serves as a community facility. Mapping the distribution of land use is necessary for several studies such as global monitoring, planning activities, and resource management (Nabawi et al., 2020). The

increase in population from time to time affects business activities that make demands on the survival of the population. So, it is necessary to carry out land management, so that there is no land conservation. According to Suyana & Muliawati (2014) defines as efforts made on land in general.

Bandar Lampung is a city with several tourism destinations, both culinary tourism, cultural tourism, marine tourism, and others. This certainly makes the development of various human activity traffic more advanced and better. Pasaran Island is one of the destinations in Bandar Lampung where Pasaran Island is the closest island to Bandar Lampung located in Teluk Betung with a panoramic view of its natural beauty. Pasaran Island is an artificial island, currently Pasaran Island is inhabited by many residents making Pasaran Island look like a slum island due to the increase in population growth living on the island.

Given that the need for space and land is needed to overcome the rate of population growth so that space and land can be properly distributed as a place for community activities, the study of the density of built-up land is important because it is a variable for urban management so that it can see the benefits of a city (Tiara et al., 2022). According to Wijaya (2013) that built-up land is a physical form that covers the face of the earth which is limited by built-up physical appearance. Many studies have been carried out on land and built-up land, including Nurrohmat (2021) Mapping deep built-up land the 250-meter Lembang fault corridor as a disaster mitigation effort. The combination of vegetation indexes uses world-view 2 satellite imagery (Hidayati et al., 2018). Other studies using NDBI and a combination of NDBI–NDVI transformations with overlay analysis were carried out by Salihin (2018). Alfarizi et al. (2015) research on built-up land using the GIS method. Land cover mapping using Landsat 8 OLI imagery using the MLC method (Sampurno and Thoriq, 2016), a combination of satellite imagery and aerial photographs for mapping the distribution of built-up land along riverbanks (Driptufany et al., 2022). Currently the existence of Unmanned Aerial Vehicle Technology is one of the efforts in accelerating the process of mapping, unmanned aerial vehicles are an alternative technology to replace remote sensing using satellite platforms (Gonçalves, 2016) especially in monitoring the increase in the number of buildings. Photogrammetry activities in general are a series of processes of photographing objects on the surface of the earth, measuring objects on aerial photographs, and processing aerial photographs into a resulting form called a map (Gularso et al., 2013). According to Syauqani et al. (2017), Photo maps can be used for planning on a large scale. Small-format aerial photographs are generally taken with a digital camera using a GPS (Gularso et al., 2015). Aerial photography using UAVs has been widely used in a variety of applications (Rahmad, 2019). The capability of the UAV-based photogrammetry system is that it has similarities with the production of using standard aerial photography images. What is different is the limited coverage area, which means it is adjusted to the ability of the system to reach locations (Andaru and Santosa, 2017). Identification of objects by interpreting aerial photographs (Chaerunnisa et al., 2017) Visual interpretation relies on image composites (Nugraha and Zuharnen, 2015). The on-screen digitization method produces line points and polygons so that they can form digital maps (Pidu et al., 2019). The on-screen digitization method can be easily repaired if there are errors (Fadilla et al., 2017). This research was conducted to determine and map the density of built-up land on Pasaran Island based on aerial Photoshoot with UAVs vehicles through

visual interpretation of aerial photographs and on-screen digitization.

## Materials and Methods

This study was conducted on Pasaran Island, Bandar Lampung (Figure 1). The time of this study began in May 2022 to October 2022. The material used in this study is Aerial Photoshoot data that has become orthophoto data. The equipment used includes Drone brand DJI Phantom 4 (Unmanned Aircraft), Geodetic GPS, Premark, Hardware, which is: Laptop Asus Core i7, Software which are: DJI Go Android application, Agisoft PhotoScan Professional Edition software.

Furthermore, the study implementation procedure consisted of preparation, data collection, measurement of control points and Aerial Photoshoot, processing of Aerial Photoshoot data, interpretation, classification and analysis. It is described as follows.

*1. Preparation Stage*

Conducting surveys to ensure field conditions, Flyway Plans, control point distribution plans, and tool preparation. Meanwhile, the preparation of literature studies is a series of activities related to library data collection methods including scientific journals, articles, books and others that are aligned with this study.

*2. Data Collection*

The data source used in this study was Aerial Photoshoot data obtained from Aerial Photoshoot using a Rotary Wing (Copter) type UAV (Unmanned Aerial Vehicle).

*3. Control Point Measurement and Aerial Photoshoot*

The control point measurement stage was to conduct a survey in advance to ensure that the site to be studied is safe for the distribution of the installed control points. The distribution for measuring control points on Pasaran Island is as follows in Figure 2.

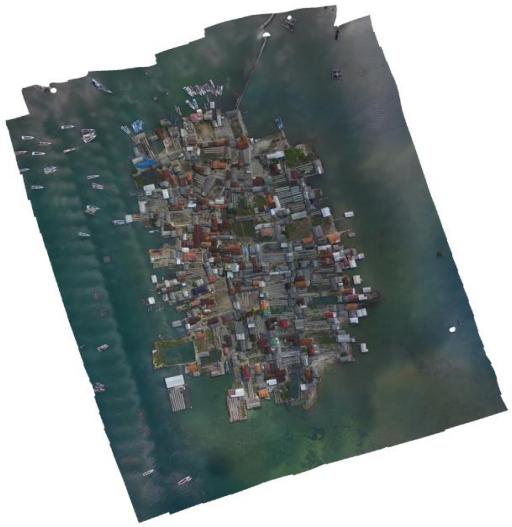

**Figure 1.** Pasaran Island.

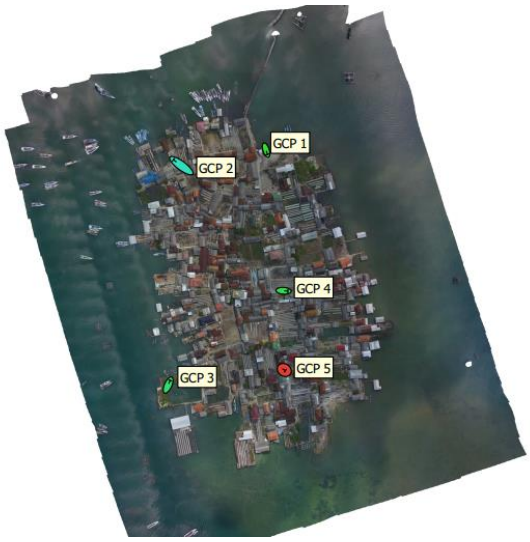


**Figure 2.** Ground Control Point Distribution.

The measurement of ground control points used Geodetic GPS (Figure 3) and performs GPS data processing of ground control points by calculating the results obtained from measurements and comparing with base maps that already have a coordinate system reference.

After determining the distribution of ground control points or GCPs, the Premark was installed (Figure 4), which was used as an identity for the existence of GCPs in the field. So that, when taking aerial photographs, it was seen from above and then measuring ground control points using Geodetic GPS.

**Figure 3**. Ground Control Point Measurement.

**Figure 4.** Installation of Premark.

**Figure 5.** Aerial Photoshoot using UAV.

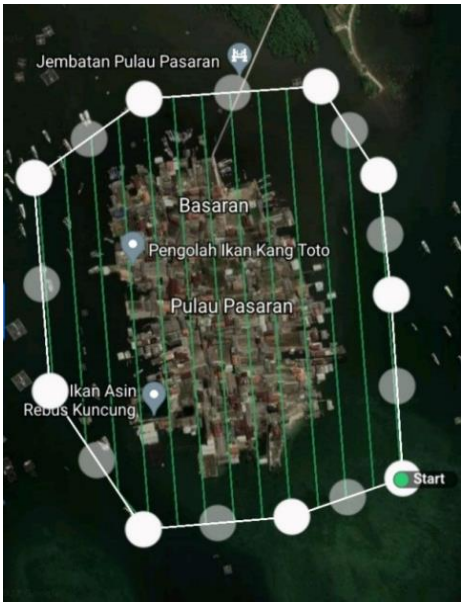


**Figure 6.** Flyway Plan.

The stages of Aerial Photoshoot were to carry out the tool calibration process first to eliminate existing distortions. Next, shooting with the UAV (Figure 5) was carried out in accordance with the Flyway Plan that has been designed. The following is an overview of the Flyway Plan as follows in Figure 6.

*4. Data Analysis*

a. Point matching process, inserting GCPs so that the coordinates in the photo match the coordinates on the ground, point cloud forming, orthophoto data forming and creating a DEM in this case an Aerial Photo DSM.
b. The process of visual interpretation and delineation of Built-up Land on orthophoto According to Sutanto (1994) using 9 elements of image interpretation, such as hue, size, shape, texture, pattern, height, shadow, position and association while Built-up Land Delineation by manually digitizing on screening of aerial photo data (orthophoto). This stage will produce Built-up Land parcels according to the situation in the field. Besides that, other land information can also be identified.
c. The process of Classification of Built-up Land is based on the recognition of

object characteristics spatially using elements of visual interpretation (Kohl et al., 2006). Classification is formed from the process of digitization or delineation. Khorram et al. (2013) that the image classification method involves some information spectral, temporal and spatial. Creating a training area is required before the manual classification process is carried out and divided into classes based on the criteria. the combination of the various selected channels can be the main point in the classification results because it relates to the visualization of the selected channel determine the classification results. Ensuring the extent of Built-up Land class and other classes. The criteria for built-up land are level II, which are: places of worship, settlements, and others. In addition to Built-up Land, other classes also need to be delineated as a complement in the depiction of the Built-up Land map. The classification of Built-up Land in this study is the class of buildings (Figure 7), open land (Figure 8), roads (Figure 9), and public facilities (Figure 10), while for Non-Built-up Land, it is the class of vegetation (Figure 11).

**Figure 7.** Building Class.

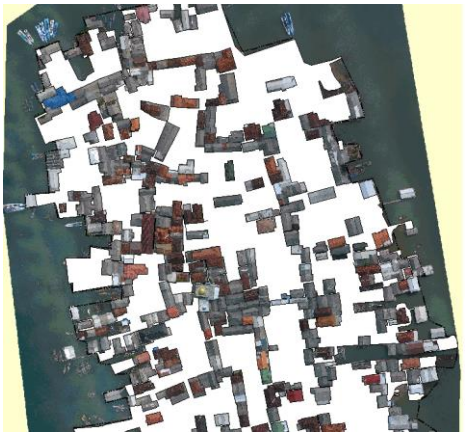

**Figure 8.** Open Land Class.

**Figure 9.** Road Class.

**Figure 10.** Public Facility Class.

**Figure 11.** Vegetation Class.

*5. Density Analysis of Built-up Land*

The analysis of the results was by calculating the area of Built-up and Non-Built-up land areas and then determining the class for the level of Built-up land density, in addition, the analysis was carried out to calculate the percentage of Built-up and Non-Built-up land in Pasaran Islandarea compared to the area so that the current state of Built-up Land and land cover of Pasaran Island was able to be known.

## Results and Discussion

The results of the Aerial Photoshoot that has been carried out are as follows in Figure 12.

*Number of images*: 206
*Flying altitude*: 106 m
*Ground resolution*: 4.25 cm/pix
*Coverage area*: 0.387 km²
*Camera stations*: 206
*Tie points*: 117,043

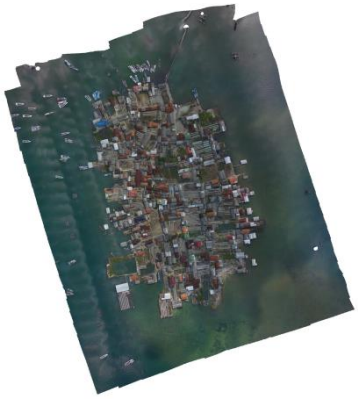

**Figure 12.** Aerial Photoshoot Result.

From the photoshoot, the orthorectification process was carried out using five GCP points. If the RMSe value is large it will cause an error on the actual measurement results (Simbolon et al., 2017). The overall RMSe result is 0.067 with RMSe details as follows in Table 1.

DEM (Digital Elevation Model) results (Figure 13) on Pasaran Island show that elevations range from -60 m to 90 m.

**Table 1.** RMSe Orthorectification.

| No | Point Name | RMS |
|---|---|---|
| 1 | GCP1 | 0.215093 |
| 2 | GCP2 | 0.92053 |
| 3 | GCP3 | 0.078985 |
| 4 | GCP4 | 0.068125 |
| 5 | GCP5 | 0.021074 |
| | **RMSe** | **0.067997** |

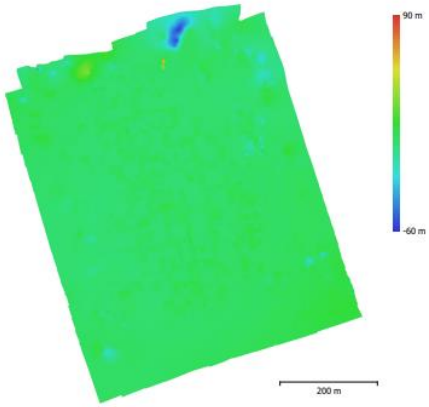


**Figure 13.** Digital Elevation Model Result.

The map of Built-up and Non-Built-up land was obtained from the process of digitizing on screening by means of aerial photo interpretation using image interpretation keys including hue or color where to distinguish land classes, using patterns. The patterns were seen that tend to be regular, shape and size adjust to the identified object. The analysis of Built-up Land Density is obtained by calculating the area of Built-up and Non-Built-up Land, determining the class for the level of built-up land density based on the classification of medium level Built-up Land such as road classes, public facilities, buildings, and open land. Calculating the percentage of Built-up and Non-Built-up Land in the area of Pasaran Island divided by the market island area, the results of the calculation of the area of each type of Built and Non-Built-up Land as follows in Table 2.

Based on the Table 2, the total area of Pasaran Island is 11.52 Ha, then the classification of Built-up and Non-Built-up Land. The Built-up Land class is divided into 4 classes, including 9 types of public

facilities consisting of places of worship such as mosques, village halls, village health centers, to elementary schools with an area of 0.19 Ha, the road network class consists of 1 type of path of 0.38 Ha, the open land class consists of 1 type of salted fish drying place because Pasaran Island is the location of the largest salted fish center in Lampung of 5.05 Ha. Furthermore, the building class consists of 40 types consisting of settlements where the majority of physical buildings are permanent with an area of 4.42 Ha with a total Built-up Land area of 10.04 Ha. The percentage of built-up land density was calculated based on the number of each class divided by the total area as follows in Table 3.

**Table 2.** Built-up and Non-Built-up Land Class Area.

| No | Classification | Area (Ha) |
|---|---|---|
| 1 | Total area of Pasaran Island | 11.52 |
| 2 | Built-up Land Area | |
| | Public Facility Area | 0.19 |
| | Road Network Area | 0.38 |
| | Open Land Area | 5.05 |
| | Building Area | 4.42 |
| | Total | 10.04 |
| 3 | Non-Built-up Land Area (Vegetation) | 1.48 |

**Table 3.** Percentage of Built-up Land Density.

| No | Density Type | Total (%) |
|---|---|---|
| 1 | Density of Built-up Land | 87,15 |
| 2 | Non-Built-up Density | 12,84 |

Based on Table 3 above, the results of Built-up Land Density of 87.15% consist of building classes, open land, public facilities and road networks. While for the results of Non-Built-up density of 12.84% consist of a vegetation class where vegetation is in the form of shady trees. The area of Pasaran Island from the results of Aerial Photography is 11.52 Ha, with a total population of 1,233 people, the population density of Pasaran Island is 107 people / Ha, which is Low Density. As for calculating building density using building data. According to BSN (2004) SNI-03-1733-2004, the formula is as follows in Equation 1.

$$\frac{Number\ of\ Buildings}{Total\ Area} = Building\ Density \quad (1)$$

**Table 4**. Classification of building density.

| No | Building Density | Total (%) |
|---|---|---|
| 1 | > 100 unit/Ha | High |
| 2 | 80 – 100 unit/Ha | Medium |
| 3 | < 80 unit/Ha | Low |

Based on the Concept Guidelines for Identification of Slum Areas Buffering Metropolitan Municipality, the classification of density building is divided into three, which are high, medium and low (Kementerian Pekerjaan Umum dan Perumahan Rakyat Direktorat Jenderal Cipta Karya, 2006) as follows in Table 4.

Based on the calculation formula above and Table 4, the building density is obtained indicating a low building density in Pasaran Island. This study produced three maps, which are Built-up and Non-Built-up Land Map, Land cover map and Built-up Land Type Map in Pasaran Island. The results of this study are as follows in Figure 14 – 16.

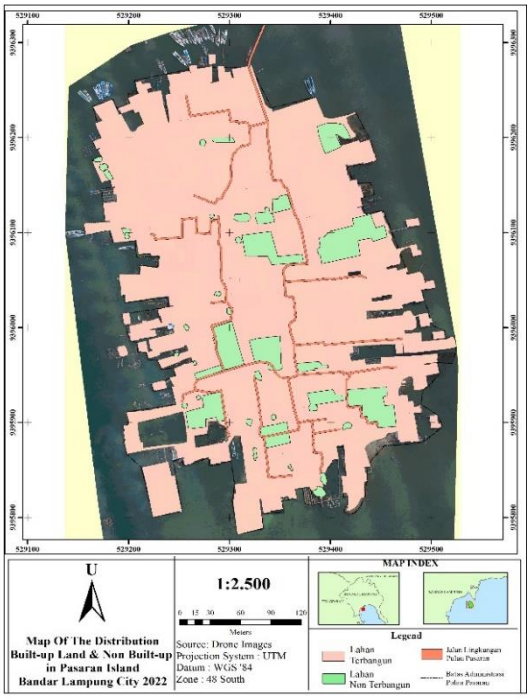


**Figure 14**. Map of Built-up and Non-Built-up Land of Pasaran Island.

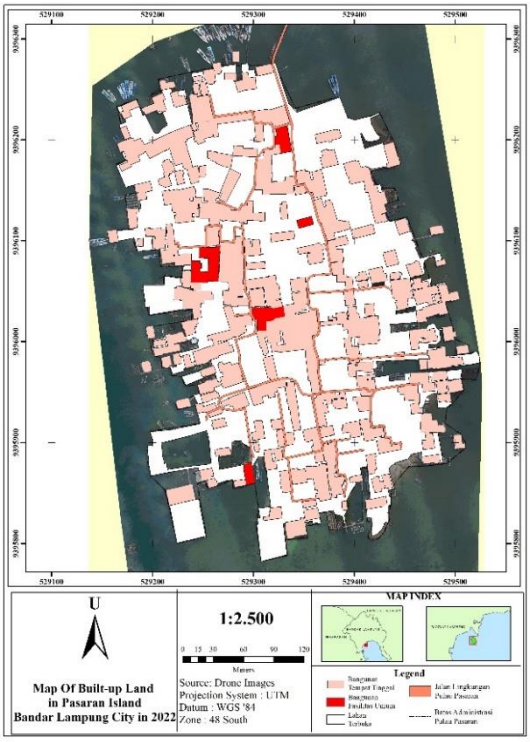


**Figure 15**. Built-up Land Map of Pasaran Island.

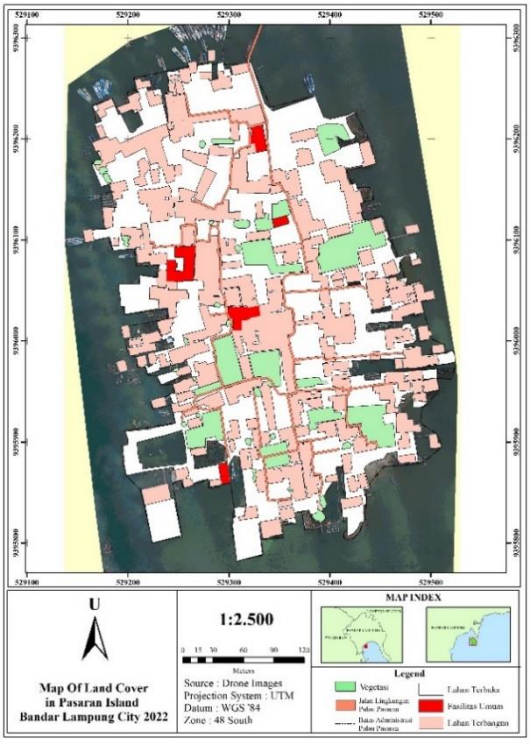


**Figure 16**. Land Cover Map of Pasaran Island.

## Conclusion

The study of Built-up Land was obtained from visual interpretation using the satellite image interpretation keys of hue, shape, size, and pattern. Build-up Land Density Mapping using UAVs (drones) is a solution to get the results of Build-up Land Density Mapping quickly and easily. The percentage of Built-up Land Density of Pasaran Island obtains the results of Built-up Land Density of 87.15% consisting of building classes, open land, public facilities, and road networks. As for the results of non-built density of 12.84% consisting of vegetation classes where vegetation in the form of shady trees, the population density of Pasaran Island is low density and the building density of Pasaran Island is also low.

## Acknowledgements

Thank you, a lot, to Unila for providing the opportunity to conduct research, thanks to the parties involved in helping carry out this research, and thanks to the editors, and reviewers of the Geocelebes journal who have provided criticism and suggestions.

## Author Contribution

Division of tasks authors, the first author the processing of Aerial Photograph Data to Become Orthophoto (Results Analysis), Ground Control Points measurement. The second author did Built-up Land Classification (Introduction), planned Flyway, ground control points distribution (materials and method), Aerial Photography (conclusion and reference).

## Conflict of Interest

In terms of financing there is already a financing agreement through research grants so it is not burdensome for researchers and fellow writers not to claim each other regarding research and article writing because there is already an agreement.

## References

Alfarizi, C. P., Subiyanto, S., & Amarrohman, F. J. (2015). Analisis Arah Pertumbuhan Wilayah Dengan

Menggunakan Metode SIG (Studi Kasus: Kabupaten Bekasi). *Jurnal Geodesi UNDIP*, 4(4), 108–117. https://ejournal3.undip.ac.id/index.php/geodesi/article/view/9936

Andaru, R., & Santosa, P. B. (2017). Analisis Spasial Bencana Longsor Bukit Telogolele Kabupaten Banjarnegara Menggunakan Data Foto Udara UAV. *Jurnal Nasional Teknologi Terapan (JNTT)*, 1(1), 77. https://doi.org/10.22146/jntt.34089

BSN. (2004). *SNI 03-1733-2004 Tata Cara Perencanaan Lingkungan Perumahan di Perkotaan*. Badan Standardisasi Nasional.

Chaerunnisa, C., Munibah, K., & Widiatmaka. (2017). Perubahan Penggunaan lahan dan Potensi Perluasan Lahan untuk Sawah di Kabupaten Cianjur. *Jurnal Tanah dan Lingkungan*, 19(1), 33–40. https://doi.org/10.29244/jitl.19.1.33-40

Driptufany, D. M., Fajrin., Kusuma, A & Guvil, Q. (2022). Pemetaan Sebaran Lahan Terbangun di Kawasan Sempadan Pantai Kota Padang Menggunakan Citra Resolusi Tinggi. *Jurnal El-Jughrafiyah*, 2(2), 87–92. http://dx.doi.org/10.24014/jej.v2i2.18738

Fadilla, L., Subiyanto, S., & Suprayogi, A. (2017). Analisis Arah dan Prediksi Persebaran Fisik Wilayah Kota Semarang Tahun 2029 Menggunakan Sistem Informasi Geografis dan CA Markov Model. *Jurnal Geodesi Undip*, 6(4), 517–525. https://ejournal3.undip.ac.id/index.php/geodesi/article/view/18184

Gonçalves, J. A. (2016). Automatic orientation and mosaicking of archived aerial photography using structure from motion. *The international of the photogrammetry, remote sensing and spatial information sciences*, XL-3/W4, 123–126. https://doi.org/10.5194/isprs-archives-XL-3-W4-123-2016

Gularso, H., Subiyanto, S., & Sabri, L. M. (2013). Tinjauan Pemotretan Udara Format Kecil Menggunakan Pesawat Model Skywalker 1680 (Studi Kasus: Area Sekitar Kampus UNDIP). *Jurnal Geodesi Undip*, 2(2), 78–94. https://ejournal3.undip.ac.id/index.php/geodesi/article/view/2440

Gularso, H., Rianasari, H., & Silalahi, F. E. S. (2015). Penggunaan Foto Udara Format Kecil Menggunakan Wahana Udara Nir-Awak dalam Pemetaan Skala Besar. *Jurnal Ilmiah Geomatika*, 21(1), 37–44.

Hidayati, I. N., Suharyadi, R., & Danoedoro, P. (2018). Kombinasi Indeks Citra untuk Analisis Lahan terbangun dan Vegetasi Perkotaan. *Majalah Geografi Indonesia*, 32(1), 24–32. https://doi.org/10.22146/mgi.31899

Kementerian Pekerjaan Umum dan Perumahan Rakyat Direktorat Jenderal Cipta Karya. (2006). *Konsep Pedoman Identifikasi Kawasan Permukiman Kumuh Penyangga Kota Metropolitan Tahun 2006.*

Khorram, S., Nelson, S. A. C., Cakir, H., van der Wiele, C. F. (2013). Digital Image Acquisition: Preprocessing and Data Reduction. In: Pelton, J.N., Madry, S., Camacho-Lara, S. (eds) *Handbook of Satellite Applications*. Springer, New York, NY. https://doi.org/10.1007/978-1-4419-7671-0_46

Kohl M., Magnussen S., & Marchetti M. (2006). *Sampling Methods, Remote Sensing and GIS Multiresource Forest Inventory*. Editor: Dieter Czeschlik. Berlin Heidelberg (EN): Springer-Verlag. https://doi.org/ 10.1007/978-3-540-32572-7

Nabawi, I., Tjung, L. J., & Pribadi, I. G. O. S. (2020). Studi Perkembangan Lahan Terbangun Serta Kesesuaian Terhadap RTRW Kabupaten Bogor Tahun 2016-2036. *Jurnal Stupa*, 2(2), 2815–2828.

https://doi.org/10.24912/stupa.v2i2.8869

Nugraha, V. S., & Zuharnen. 2015. Pemanfaatan Teknologi Penginderaan Jauh untuk Monitoring Densifikasi Bangunan di Daerah Perkotaan Magelang. *Jurnal Bumi Indonesia*, 4(1), 301–306. https://core.ac.uk/download/pdf/295176238.pdf

Nurrohmat, A. (2021). Pemetaan Sebaran lahan Terbangun Dalam Koridor 250 Meter Sesar Lembang. *Elipsoida: Jurnal Geodesi dan Geomatika*, 4(01), 42–49. https://doi.org/10.14710/elipsoida.2021.11497

Pidu, R. E., Sudarsono, B., & Amarrohman, F. J. (2019). Analisis Kesesuaian Penggunaan Lahan Kawasan Industri dan Lahan Terbangun Terhadap RTRW di Kecamatan Bawen Dan Kecamatan Pringapus Menggunakan Sistem Informasi Geografis. *Jurnal Geodesi UNDIP*, 9(1), 295–304. https://ejournal3.undip.ac.id/index.php/geodesi/article/view/26174

Rahmad, R. (2019). Pemanfaatan Drone DJI Phantom 4 Untuk Identifikasi Batas Administrasi Wilayah. *Jurnal Geografi*, 11(2), 218–223. https://doi.org/10.24114/jg.v11i2.10604

Salihin, I., Akbar, L. O. N., & Jaya. G. (2018). Analisis Perubahan Tingkat Kepadatan Lahan Terbangun Kota Kendari Berdasarkan Indeks Lahan Terbangun. *JAGAT (Jurnal Geografi Aplikasi dan Teknologi)*, 2(2), 1–10. https://doi.org/10.5281/zenodo.2667849

Sampurno, R. M., & Thoriq, A. (2016) Klasifikasi Tutupan Lahan Menggunakan Citra Landsat 8 Operational Land Imager (OLI) di Kabupaten Sumedang. *Jurnal Teknotan*, 10(2), 61–70. https://jurnal.unpad.ac.id/teknotan/article/view/9941

Simbolon, A. B. S., Yuwono, B. D., & Amarrohman, F. J. (2017). Analisis Perbandingan Ketelitian Metode Registrasi Antara Metode Kombinasi Dan Metode Traverse Dengan Menggunakan Terrestrial Laser Scanner Dalam Pemodelan Objek 3 Dimensi. *Jurnal Geodesi Undip*, *6*(4), 285–294. https://ejournal3.undip.ac.id/index.php/geodesi/article/view/18153

Sutanto. (1994). *Penginderaan Jauh Jilid I*. Gadjah Mada University Press.

Suyana, J., & Muliawati, E. S. (2014). Analisis Kemampuan Lahan pada Sistem Pertanian di Sub-DAS Serang Daerah Tangkapan Waduk Kedung Ombo. *Agrista: Jurnal Ilmiah Mahasiswa Agribisnis UNS*, 11(2), 139–149. https://doi.org/10.15608/stjssa.v11i2.245

Syauqani, A., Subiyanto, S., & Suprayogi, A. (2017). Pengaruh Variasi Tinggi Terbang Menggunakan Wahana Unmanned Aerial Vehicle (UAV) Quadcopter Dji Phantom 3 Pro Pada Pembuatan Peta Orthofoto (Studi Kasus Kampus Universitas Diponegoro). *Jurnal Geodesi UNDIP*, 6(1), 249–257. https://ejournal3.undip.ac.id/index.php/geodesi/article/view/15388

Tiara, D., Sabri, L., & Sukmono, A. (2022). Analisis Perubahan Kepadatan Dan Pola Lahan Terbangun Menggunakan Interpretasi Hibrida Citra Sentinel 2A (Studi Kasus: Kota Ungaran). *Jurnal Geodesi UNDIP*, 11(1), 41–50. https://ejournal3.undip.ac.id/index.php/geodesi/article/view/32273

Wijaya, M. S., & Susilo, B. (2013). Integrasi Model Spasial Cellular Automata dan Regresi Logistic Biner untuk Pemodelan Dinamika Perkembangan Lahan Terbangun (Studi Kasus Kota Salatiga). *Jurnal Bumi Indonesia*, 2(1), 125–133.

Webster, D. (2002). *On the Edge: Shaping the Future of Peri-urban East Asia*.

Institute for International Studies Asia/ Pacific Research Center, Stanford University. https://aparc.fsi.stanford.edu/publications/on_the_edge_shaping_the_future_of_periurban_east_asia

ISSN: 2579-5821 (Print)
ISSN: 2579-5546 (Online)
URL address: http://journal.unhas.ac.id/index.php/geocelebes
DOI: 10.20956/geocelebes.v7i1.23065

Jurnal Geocelebes Vol. 7 No. 1, April 2023, 64 – 76

# Mine Design of Laterite Nickel Ore Based on Pit Limit Optimization with Floating Cone Method at Meranti Pit of PT Ang and Fang Brother

Rifyan Sabaruddin, Aryanti Virtanti Anas*, Rizki Amalia, Rini Novrianti Sutardjo Tui

Department of Mining Engineering, Engineering Faculty, Universitas Hasanuddin, Indonesia.

*Corresponding author. Email: aryantiv@unhas.ac.id

Manuscript received: 20 September 2022; Received in revised form: 6 March 2023; Accepted: 30 April 2023

**Abstract**

PT Ang and Fang Brother Site Lalampu is a nickel laterite mines company located at Lalampu Village, Morowali Regency, Central Sulawesi Province. The purpose of research is to determine the ultimate pit limit using floating cone method and calculate the net present value (NPV), to design the ultimate pit limit at Front 8 of Meranti Pit (one of the company's fronts), to calculate the mined laterite nickel reserves and the overburden based on the pit design. The data used are block model data, topography, capital and operating costs, commodity price, density, geotechnical data, mine recovery 85%, cut-off grade 1.3%, and the company's production target of 50,000 tons/month. Data processing generates Pit Shell 9 as the ultimate pit limit with ore recovery of 264,375 tons from 284,063 tons of Front 8 resources. Based on the design using Micromine 2021 software with an area of 5.25 hectares, a total of 234,142 tons laterite nickel ore obtained by stripping 389,063 BCM of the overburden, and it still economical with stripping ratio value (1.66 BCM/ton), smaller than the BESR value (6.32 BCM/ton). The amount of nickel laterite reserves produced based on mine recovery of 85% is 199,021 tons so the life of mine lasted 3.98 months.

**Keywords**: Laterite nickel; pit optimization; pit design.

**Citation**: Sabaruddin, R., Anas, A. V., Amalia, R. and Tui, R. N. S. (2023). Mine Design of Laterite Nickel Ore Based on Pit Limit Optimization with Floating Cone Method at Meranti Pit of PT Ang and Fang Brother. *Jurnal Geocelebes,* 7(1):64–76, doi: 10.20956/geocelebes.v7i1.23065

## Introduction

PT Ang and Fang Brother Site Lalampu is one of the companies engaged in mining, especially for laterite nickel ore mining. The company is located at Lalampu Village, Bahodopi District, Morowali Regency, Central Sulawesi Province. The Mining Business Permit obtained by PT Ang and Fang Brother at Lalampu is divided into two, which are IUP 576 and IUP 199. IUP 576, which is the research location, has a mining area of 576 hectares based on Morowali Regent Decree No.540.3/SK.002/DESDM/IV/ 2012 dated April 19, 2012 (PT Ang and Fang Brother, 2019). IUP 576 consists of several pits, one of them is the Meranti Pit. It is carried out the mining operation based on the consideration of a cut-off grade of 1.3%. It also has eight mining fronts; six fronts are in the mining process and two other fronts have not been mined yet including Front 8. Front 8 has an area of 5.68 hectares (Figure 1) and there are 21 drill points obtained from exploration activities and used in the mine planning stage.

PT Ang and Fang Brother applies an open-pit mining system (surface mining) with a selective mining method. Open pit mining is a common mining method which carried out above the surface by stripping the overburden. Open pit mine design and long-term production scheduling is a critically important part of mining business. The optimization of long-term planning deals with the maximization of Net Present Value (NPV). Life-of-mine planning determines the technical plan to be

followed from mine development to mine closure and further rehabilitation. The work must associate all the different processes in the mining value chain to maximize Net Present Value (NPV) (Araya et al., 2020; Meagher et al., 2014).


**Figure 1.** The location of Front 8 of Meranti Pit that has an area of 5.68 hectares.

Pit optimization is an effort to determine the ultimate pit limit (UPL) that engenders the highest NPV compared the other potential pits (Esmaeil et al., 2018). The pit expansion that gives a profit equal to zero is called the break-even stripping ratio (BESR). The break-even approach of pit limit is often sought for through the economic limit stripping ratio, which is the maximum stripping ratio above which the pit cannot break-even. The limiting stripping ratio can only be used in a preliminary assessment of pit limits. However, the use of NPV in pit limit analysis optimizes the value of the deposit (Nwosu et al., 2022).

The methods that are often applied in pit optimization, especially in ore mining are the Learch-Grossman method and the floating/moving cone. The floating or moving cone algorithm is one of the easiest and fastest algorithms to determine the optimum solution of mining pit limit (Jodeiri et al., 2021; Zeyni et al., 2011). This algorithm first designed an upward cone for ore blocks based on the desired slope angle. Then the value of all the blocks in the cone is added together. If the result is a positive value, all the blocks inside the cone are removed. Otherwise, it is ignored (Azadi et al., 2023).

The floating cone method is not commonly used compared to the Lerch-Grossman method and still has disadvantage, that is the maximum net present value (NPV) produced by the pit shell is smaller than the Lerch-Grossman method. However, the floating cone method always provides a solution and can be easily programmed (Ares et al., 2022). In addition, restrictions of mining operations on various slopes can be perfectly applied to this method (Zeyni et al., 2012). The method contains errors in most cases but still used due to the simplicity (Jodeiri et al., 2021). Therefore, this study was conducted to design and determine the ultimate pit limit at Front 8 of Meranti Pit that has maximum NPV value using the floating cone method with considering the BESR value which provides the highest benefit.

*Laterite Nickel*

Laterite nickel is a material derived from regolith, a layer that is the result of weathering of rocks that surrounds a bedrock, from ultramafic igneous rocks containing Ni and Co elements, formed through intensive physical and chemical weathering processes in areas with tropical to subtropical climates. The process of forming laterite nickel deposits begins with the deposition of the parent rock, namely peridotite, which has a composition of laterite nickel ranged between 0.2% - 0.4%. Nickel is hosted in several minerals such as oxides, Mg silicates and clays. The mineralogy and ore grade depend on the lithology and climate during the formation

of the deposit (König, 2021; Xiao, et al., 2020; Butt and Cluzel, 2014).

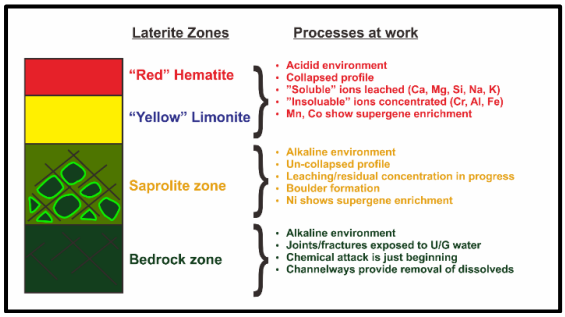


**Figure 2**. Lithology profile of laterite nickel deposits (Rahmi and Yulhendra, 2019).

The profile of laterite nickel deposits formed from weathering of ultramafic rocks generally consists of four layers, which are top soil, limonite, saprolite, and bedrock layers that are shown in Figure 2 (Rahmi and Yulhendra, 2019).

*Floating Cone*

Pit optimization determines the shape of the pit that is most likely to obtain the largest total recovery value (Whittle and Rozman, 1991). If optimization is a process, then the result of pit optimization is a pit that has become more effective and has advantages (Gusman and Octova, 2018). The floating or moving cone algorithm is one of the easiest and simplest algorithms to determine the optimal pit boundary (Ares et al., 2022).

The floating cone was first described by Carlson, Erickson, O'Brain and Pana in 1966, apply for each positive (ore) block. This method involves constructing a cone with oriented parallel sides to the slope angle of the pit, and then determining the value of the cone by summing value of the block enclosed in it. If the cone value is positive, all blocks inside the cone are mined. This process starts from the top level and moves downwards looking for positive blocks. It continues until there are no positive cones left in the block model (Zeyni et al., 2011).

The floating cone belongs in the automated method, means it's completely done by computer based on economic and physical parameters, and it is capable of designing mine boundaries based on existing economic and physical parameters without designer intervention. One of the computer programs that can perform these tasks is FOUR-D Whittle Open Pit Optimization Software program which is a product of Whittle Programming Proprietary Limited Australia, as well as other similar programs (Whittle and Rozman, 1991). The target that will be used in determining the pit limit in the floating cone method requires that the final limit calculated using basic return economics.

*Pit Design*

The design of a mining pit is the first step in evaluating the amount of minerals. One of the parameters that becomes a reference in the design of mining pit is the pit limit (Hustrulid et al., 2013). Parameters that affect mining boundaries to calculate mineable reserves include the strip ratio calculated by the BESR are mining slope geometry, topographical and geological conditions (Aswandi and Yulhendra., 2019).

## Research Methods

Design and optimization pit aims to determine the most ultimate pit limit to obtain minerals that are constrained by mining and economic conditions. In general, this research discusses the ultimate pit limit design and requires detailed data related to technical and economic factors of mining.

*1. Data Collections*

a. Block model
   Block model is the basic model at the research site to make mining pit of Front 8.
b. Meranti Pit topographic

Topographic data is data related to the contour or elevation of the mining site in the Meranti Pit.

c. Density and cut-off grade
The ore density used in this study is 1.5 tons/BCM, the waste and overburden density are 1.6 tons/BCM, and the cutoff grade is 1.3%.

d. Mine recovery
Mine recovery is 85% based on historical data obtained from the Mine Plan Engineer Department.

e. Commodity price
Commodity price used is USD 38 per wet metric ton obtained from the Finance Department based on consideration of market conditions and economic analysis on the sale of low-grade nickel in 2021.

f. Capital cost
The capital cost in this study is historical data obtained from the Ministry of Finance which is shown in Table 1.

g. Operating costs
The operating costs calculated in this study are divided into two, which are the cost of mining and processing ore (ore) which is shown in Table 2 and the cost of stripping overburden (OB) which is shown in Table 3

**Table 1.** Capital cost parameters (PT Ang and Fang Brother, 2019).

| Capital cost parameters | Cost (USD) |
|---|---|
| Licencing cost | 477 |
| Land acquisition cost | 143,149 |
| Exploration cost | 84,327 |
| AMDAL cost | 1,193 |
| Feasibility study cost | 716 |
| Construction cost | 75,225 |
| Total cost | 305,086 |

**Table 2.** Ore cost parameters (PT Ang and Fang Brother, 2019).

| Ore cost parameters | Cost (USD/ton) |
|---|---|
| Ore getting | 1.55 |
| Barging | 1.92 |
| Supporting | 0.91 |
| Man Power | 0.53 |
| Hauling | 1.20 |
| Blending | 0.42 |
| Total cost | 6.53 |

**Table 3.** Overburden cost parameter (PT Ang and Fang Brother, 2019).

| Overburden cost parameters | Cost (USD/ton) |
|---|---|
| OB removal | 2.23 |
| Supporting | 0.91 |
| Man Power | 0.53 |
| Hauling | 1.19 |
| Total cost | 4.86 |

h. Operating costs
The operating costs calculated in this study are divided into two, which are the cost of mining and processing ore (ore) which is shown in Table 2 and the cost of stripping overburden (OB) which is shown in Table 3.

i. Bench geometry and haul roads
Bench geometry data includes a height of 3 meters, a width of 2 meters, and a slope angle of 60°. The width of the haul road (ramp) used by the company is 10 meters with a 10% grade.

j. Monthly production
Monthly production target is the planned number of tonnage of ore to be mined at the Front 8 of Meranti Pit every month. The production target used in making discounted cash flow is 50,000 tons/month.

*2. Data Processing*

a. Resource estimation using block model data.

b. Calculation of the break-even stripping ratio (BESR).
The BESR value can be obtained through the Equation 1 (Maritz and Uludag, 2019):

$$\text{BESR} = \frac{(1-x)s - c}{w} \quad (1)$$

where x = production fee / royalty (%), s = commodity price ($), c = variable cost of ore mining ($/ton), w = variable cost of stripping overburden ($/BCM). The data used commodity price (s) worth 38 USD/ton, ore mining cost (c) 6.53 USD/ton and overburden stripping cost (w) 4.86 USD/BCM obtained from the company and royalty value (x) 2%

based on Government Regulation no. 81 of 2019. The calculation of BESR is as follows:

$$\text{BESR} = \frac{(1\text{-}0{,}02)\ 38\ \text{USD/ton} - 6.52\ \text{USD/ton}}{4.86\ \text{USD/BCM}}$$

$$\text{BESR} = \frac{30.72}{4.86} = 6.32\ \text{BCM/ton}$$

c. Pit optimization using the floating cone method with the help of Whittle 4.5.1 and Surpac 6.6.2 software. The data used are block model data, capital costs, operating costs, and geotechnical data.
d. Calculation of NPV.
e. Mining pit design using Micromine 2021 based on a predetermined ultimate pit limit.
f. Calculation the amount of laterite nickel reserves and overburden based on the designed pit.

## Results and Discussion

Cut-off grade is one of the most important parameters in metal ore mining because of its influence on the overall economic profit of mining production (Qing Hua et al., 2014). Laterite nickel deposits are limited by a cutoff grade (COG) as a criterion to identify waste of minerals in a mining reserve of 1.3% which was set by the company. Deposits that are limited by this COG value are further classified as a resource. Resource estimation is carried out to determine the volume, tonnage, and grade of laterite nickel ore deposits.

The total number of nickel resources in the Front 8 of Meranti Pit block model is known by reporting the block model obtained from the company and has been estimated using the Inverse Distance Weighting (IDW) method. The density of nickel ore was set by the company that used in this research is 1.5 tons/BCM. This density is used to determine the tonnage of laterite nickel ore deposits by multiplying the density and volume of laterite nickel ore deposits.

Resource reporting using Surpac 6.6.2 software by dividing reporting categories into four, that are high grade ore (HGO) with a grade range of 1.7%, medium grade ore (MGO) with a grade range of 1.5%-1.7%, and low-grade ore (LGO) with a grade range of 1.3%-1.5%, and the overall grade of ore is 1.3%. In addition to the nickel element, resource reporting is also carried out to display the grade of other elements, that are iron and cobalt contained in laterite nickel ore deposits. The results of reporting resources obtained can be seen in Table 4.

**Table 4.** Resources reporting results based on the Front 8 of Meranti Pit block model.

| Category | Volume (BCM) | Tonnage (Ton) | Ni Grade Average | Fe Grade Average | Co Grade Average |
|---|---|---|---|---|---|
| LGO | 67,188 | 100,781 | 1.39% | 32.56% | 0.10% |
| MGO | 45,313 | 67,969 | 1.60% | 23.92% | 0.07% |
| HGO | 76,875 | 115,313 | 1.91% | 20.63% | 0.05% |
| Total | 189,375 | 284,063 | 1.65% | 25.65% | 0.08% |

The total nickel laterite resource in Front 8 of Pit Meranti is 284,063 tons with an average nickel grade of 1.65%, an average iron grade of 25.65%, and an average cobalt grade of 0.08%. The grade of nickel ore in each class has a different tonnage amount, which are LGO with an average nickel grade of 1.39% at 100,781 tons, MGO with an average nickel grade of 1.60% at 67,969 tons, and HGO with an average of 1.91% of 115,313 tons. These resources are used as the basis for carrying out the mine planning stages, which are the optimization of pit limits, and additional attributes were added to the Front 8 of Meranti Pit block model using Surpac 6.6.2 software to overview the shape of the laterite nickel ore deposits. These additional attributes are grade attribute which reads ore with a value of 1, flag attribute which reads ore with ore character, and overburden density attribute

to obtain stripping ratio value when optimizing pit limit.

Pit limit optimization on the Front 8 of Meranti Pit with the floating cone method is carried out using two different software that implements the floating cone algorithm.

*a. Pit limit optimization using Whittle*

Geovia Whittle 4.5.1 software able to design mine boundaries based on existing economic and physical parameters (Whittle and Rozman, 1991). Whittle produced a nested pit shell consisting of 17 pit shells with different Revenue Adjustment Factors (RAF) so that they have different ore and overburden tonnage gains. The obtained ore tonnage and overburden for each pit shell produced are shown in Table 5 and Figure 3.

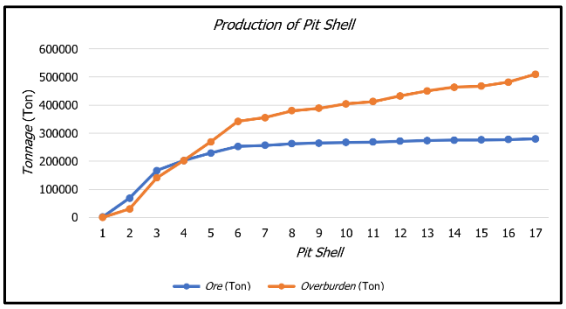


**Figure 3**. Tonnage graphic of nested pit shell.

The volume of overburden is obtained by dividing the tonnage by the density of the overburden, which is 1.6 tons/BCM. In Pit Shell 9 with RAF 1 obtained 264,375 tons of ore by stripping 243,017.50 BCM of overburden so that the stripping ratio is 0.92 BCM/ton. The average nickel ore grade obtained from Pit Shell 9 is 1.66%, this value is almost close to the average nickel grade obtained from other pit shells. This means that there is no significant difference in the average nickel content gain in each pit shell.

The larger the number and the RAF pit shell, the greater the ore and overburden tonnage obtained. Pit Shell 1 with RAF 0.2 had the smallest gain due to the small pit shell opening area, while Pit Shell 17 with RAF 2 had the largest ore and overburden tonnage gain due to the large pit shell opening area.

Determination of the ultimate pit limit at Whittle using the floating cone method based on the value of the BESR and the calculation of discounted cash flow (DCF) for each pit shell so that it is known which pit shell has the largest NPV. BESR is the maximum stripping ratio (SR) of a pit shell that will be selected in the mining design process. Based on the calculated BESR value of 6.32 BCM/ton, it is known that economically 6.32 BCM overburden stripping to obtain one tons of nickel ore is still considered economical. All the pit shells produced have an SR value (Table 5) below the BESR value, so overall they are feasible to mine.

Pit shells that have a maximum NPV can be seen in pit shells that have an incremental SR value equal to the BESR value, so that an incremental SR calculation is carried out for each pit shell. The incremental SR value is obtained from the division of overburden and ore increments from each pit shell. Variable increase in ore per pit shell is obtained from reducing the amount of nickel ore in a pit shell with the amount of nickel ore in the previous pit shell, as well as the variable increase in overburden. The results of the incremental SR calculation for each pit shell are shown in Table 6.

The larger the pit shell opening, the greater the incremental SR produced. Pit Shell 16 with an RAF of 1.9 has an incremental SR value that is close to the BESR value, so it is assumed to have the largest NPV. Data processing is continued by calculating the discounted cash flow for each pit shell to determine the NPV of each pit shell based on the principle of sequence and scheduling on Whittle. The results of the discounted cash flow calculation can be seen in Table 7 and Figure 4.

**Table 5.** Tonnage gains of ore and overburden nested pit shell.

| Pit Shell | RAF | Ore (Ton) | Overburden (Ton) | Overburden (BCM) | SR (BCM/ton) | Ni Ore Grade (%) |
|---|---|---|---|---|---|---|
| 1 | 0.2 | 938 | 0 | 0,00 | 0.00 | 1.83 |
| 2 | 0.3 | 68,438 | 29,531 | 18,456.88 | 0.27 | 1.75 |
| 3 | 0.4 | 166,875 | 140,859 | 88,036.88 | 0.53 | 1.70 |
| 4 | 0.5 | 202,266 | 202,265 | 126,415.63 | 0.62 | 1.68 |
| 5 | 0.6 | 229,453 | 269,531 | 168,456.88 | 0.73 | 1.67 |
| 6 | 0.7 | 252,891 | 341,953 | 213,720.63 | 0.85 | 1.67 |
| 7 | 0.8 | 256,641 | 355,547 | 222,216.88 | 0.87 | 1.66 |
| 8 | 0.9 | 262,500 | 379,922 | 237,451.25 | 0.90 | 1.66 |
| 9 | 1.0 | 264,375 | 388,828 | 243,017.50 | 0.92 | 1.66 |
| 10 | 1.1 | 267,188 | 404,296 | 252,685.00 | 0.95 | 1.66 |
| 11 | 1.2 | 268,594 | 412,734 | 257,958.75 | 0.96 | 1.66 |
| 12 | 1.3 | 271,641 | 432,890 | 270,556.25 | 1.00 | 1.65 |
| 13 | 1.4 | 273,984 | 450,469 | 281,543.13 | 1.03 | 1.65 |
| 14 | 1.5 | 275,625 | 463,594 | 289,746.25 | 1.05 | 1.65 |
| 15 | 1.6-1.7 | 276,094 | 467,812 | 292,382.50 | 1.06 | 1.65 |
| 16 | 1.8-1.9 | 277,500 | 481,875 | 301,171.88 | 1.09 | 1.65 |
| 17 | 2.0 | 280,078 | 510,235 | 318,896.88 | 1.14 | 1.65 |

**Table 6.** Calculation results of incremental SR nested pit shell.

| Pit Shell | RAF | Ore Changes (Tons) | Overburden Changes (BCM) | SR Incremental (Tons/BCM) |
|---|---|---|---|---|
| 1 | 0.2 | - | - | - |
| 2 | 0.3 | 67,500 | 18,456.88 | 0.273 |
| 3 | 0.4 | 98,437 | 69,580.00 | 0.707 |
| 4 | 0.5 | 35,391 | 38,378.75 | 1.084 |
| 5 | 0.6 | 27,187 | 42,041.25 | 1.546 |
| 6 | 0.7 | 23,438 | 45,263.75 | 1.931 |
| 7 | 0.8 | 3,750 | 8,496.25 | 2.266 |
| 8 | 0.9 | 5,859 | 15,234.38 | 2.600 |
| 9 | 1.0 | 1,875 | 5,566.25 | 2.969 |
| 10 | 1.1 | 2,813 | 9,667.50 | 3.437 |
| 11 | 1.2 | 1,406 | 5,273.75 | 3.751 |
| 12 | 1.3 | 3,047 | 12,597.50 | 4.134 |
| 13 | 1.4 | 2,343 | 10,986.88 | 4.689 |
| 14 | 1.5 | 1,641 | 8,203.13 | 4.999 |
| 15 | 1.6-1.7 | 469 | 2,636.25 | 5.621 |
| 16 | 1.8-1.9 | 1,406 | 8,789.38 | 6.251 |
| 17 | 2.0 | 2,578 | 17,725.00 | 6.875 |

Whittle produces two kinds of scheduling scenarios, best case, and worst case. The best-case scenario has a mining pattern starting from a pit shell with a small SR so it is possible to get ore faster, while the worst-case scenario has a mining pattern starting from the highest elevation to the lowest elevation without considering the pit shell SR so that the actual implementation is easier.

RAF affects the discounted cash flow calculation for each pit shell. RAF varies the price of ore differently, resulting in different scheduling and NPV scenarios for each pit

shell. Each pit shell has a different NPV value in each scenario, besides the mine life in the worst-case scenario is longer than the best-case scenario. Overall, in both scenarios, it is known that the larger the pit shell opening, the longer the life of the mine.

Figure 4 shows the results of discounted cash flow calculations and analysis of each pit shell. The x-axis being the pit shell and the y-axis being the NPV. The increase in the size of the pit shell does not determine the magnitude of the increase in profits. Profits are affected by the difference between the total profit from nickel ore mining and the cost of overburden removal. Pit Shell 9 is the most profitable pit shell or has the largest NPV in both scenarios, worth USD 5,557,414 in the best-case scenario and USD 5,512,302 in the worst-case scenario.

**Table 7.** Calculation result of discounted cash flow nested pit shell.

| Pit Shell | NPV of Best Case (USD) | NPV of Worst Case (USD) | Life of Mine of Best Case (Month) | Life of Mine of Worst Case (Month) |
|---|---|---|---|---|
| 1 | -275,503 | -275,503 | 0.02 | 0.02 |
| 2 | 1,658,924 | 1,658,924 | 1.37 | 1.37 |
| 3 | 4,034,807 | 4,030,936 | 3.33 | 3.33 |
| 4 | 4,755,217 | 4,746,147 | 4.04 | 4.04 |
| 5 | 5,191,137 | 5,175,106 | 4.58 | 4.58 |
| 6 | 5,480,747 | 5,446,448 | 5.05 | 5.23 |
| 7 | 5,515,702 | 5,477,699 | 5.12 | 5.33 |
| 8 | 5,552,153 | 5,508,912 | 5.25 | 5.49 |
| 9 | 5,557,414 | 5,512,302 | 5.30 | 5.54 |
| 10 | 5,553,142 | 5,507,491 | 5.39 | 5.60 |
| 11 | 5,546,958 | 5,500,977 | 5.43 | 5.63 |
| 12 | 5,522,786 | 5,475,611 | 5.55 | 5.69 |
| 13 | 5,492,305 | 5,442,120 | 5.64 | 5.75 |
| 14 | 5,466,284 | 5,414,256 | 5.71 | 5.79 |
| 15 | 5,456,164 | 5,403,358 | 5.73 | 5.81 |
| 16 | 5,417,756 | 5,362,238 | 5.81 | 5.85 |
| 17 | 5,332,697 | 5,271,807 | 5.95 | 5.94 |

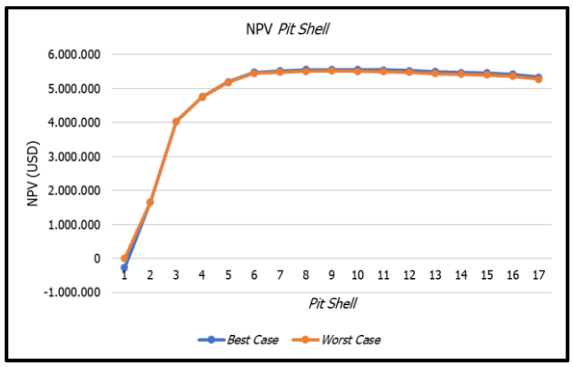


**Figure 4.** NPV Graphic of nested pit shell.

The optimal Pit Shell 16 based on BESR has a smaller NPV value than Pit Shell 9 after the scheduling scenario is carried out. This can be happened due to the addition of the discount rate and capital cost parameters which resulted in the optimal pit shell opening being smaller in the Whittle analysis. Pit Shell 9 is considered the most profitable to mine and is used as a reference in designing the ultimate pit limit as shown in Figure 5. The three-dimensional view of Pit Shell 9 is shown in Figure 6.

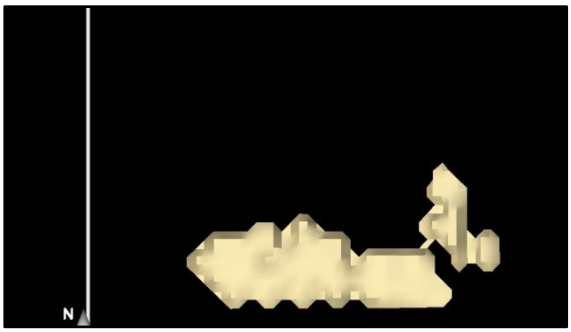


**Figure 5.** Pit Shell 9 display using Whittle. The pit shell is cream with plan view.

Pit Shell 9 is the ultimate pit limit at RAF 1 or when the normal ore selling price is USD 38/ton. The stripping ratio produced from this pit shell is 0.92 BCM/ton. The mining sequence in this pit shell starts from Pit Shell 1,2,3,4,5,6,7,8 to Pit Shell 9.

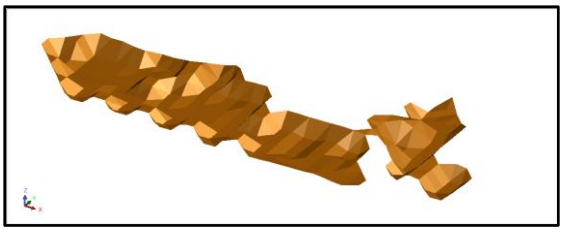

**Figure 6.** Pit Shell 9 display using Surpac. The pit shell is brown with 3d view.

*b. Pit limit optimization using Surpac*

Surpac is a mine planning and designing software that has been developed by Gemcom International. It uses in application for the process of geological modelling and opencast mine to quantify and evaluate mineral deposits and to plan the efficient extraction of reserves. Geovia Surpac is the most widely used software system of its kind in the world, supporting open pit and underground mining operations (Agrawal, 2012).

After optimization of pit limits, Surpac produces only one ultimate pit limit because it does not have RAF input parameters that can produce pit shell variations. Surpac's ultimate pit limit has an NPV of USD 9,840,855. This higher NPV is due to Surpac does not have an input of production parameters per month so that the mine life may be shorter, besides that capital costs are not included in the optimization process. The ultimate pit limit resulting from the optimization of the pit limit using Surpac is shown in Figure 7.

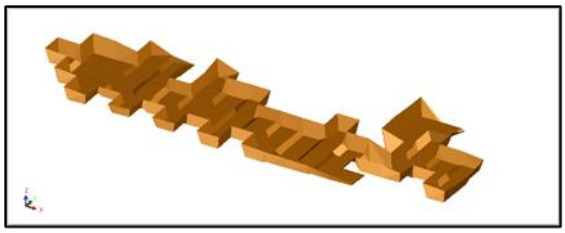

**Figure 7.** Ultimate pit limit by using Surpac. The pit limit is brown with 3D view.

The appearance and area of the ultimate pit limit produced by Surpac is identical to the Pit Shell 16 produced by Whittle which is the ultimate pit limit based on the BESR value. For this reason, the calculation of the amount of nickel ore obtained from the ultimate pit limit generated is carried out.

The results of the calculation of Surpac ultimate pit limit ore recovery are 277,266 tons (Table 8). The ore recovery is close to the ore recovery at Pit Shell 16 produced by Whittle, which is 277,500 tons. This shows that the ultimate pit limit produced by Surpac is the same as the optimal pit shell produced by Whittle based on the BESR value, but Pit Shell 16 has a less than optimal NPV value in the Whittle scheduling scenario. The pit shell that is used as a reference in designing the ultimate pit limit is Pit Shell 9 produced by Whittle which has a maximum NPV value.

**Table 8.** Calculation results of ore recovery on Surpac ultimate pit limit.

| Category | Volume (BCM) | Tonnage (Ton) | Ni Grade Average |
|---|---|---|---|
| LGO | 63,281 | 94,922 | 1.39% |
| MGO | 44,688 | 67,031 | 1.60% |
| HGO | 76,875 | 115,313 | 1.91% |
| Total | 184,844 | 277,266 | 1.65% |

The pit design is based on the mining method applied by the company, namely the open pit mining method. The open pit mining method is an open pit mining technique to extract nickel ore from pits. This mining method is effectively applied to the Front 8 of Meranti Pit area which is relatively flat.

The pit design is based on topographical forms and the ultimate pit limit results from the Whittle 4.5.1 software that have been previously determined. The ultimate pit limit design uses geometric parameters set by the company. The width of the haul road used in designing the ultimate pit limit based on company standards is 10 meters with a minimum slope of 10%. The ultimate pit limit on the Front 8 of Meranti Pit is designed using Micromine 2021 software because the process is easy and fast and can produce many types of output. The use of Micromine software is advised for all mining projects from exploration to exploitation and later operation (Shehu and Lipo, 2016).

The ultimate pit limit designed by using Micromine 2021 has a difference with the pit limit optimization results from Whittle. This is due to technical factors and several

adjustments made, such as the construction of berms and ramps at each mining level which resulted in widening of the ultimate pit limit design. This widening causes the ore recovery to decrease, the overburden increases, to increase the stripping ratio. The resulting outputs include the pit limit design is shown in Figure 8.

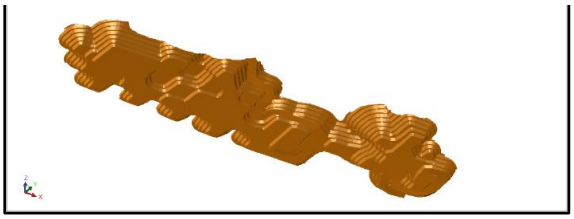

**Figure 8.** Front 8 ultimate pit limit design which 15 mining levels. The lowest elevation of 82 masl and the highest is 127 masl.

Surpac 6.6.2 produce several functions to modeling resources and reserves (ore bodies) (Tivig et al., 2015). Reserves are resources that have met the technical and economic factors to be mined, namely block models that have a nickel grade of more than or equal to the cut-off grade and are within the design pit limit. Overburden is a model block that is above the reserves that must be removed to obtain ore and have a nickel grade below the cut-off grade.

The density used to obtain the total tonnage is 1.5 tons/BCM for laterite nickel ore and 1.6 tons/BCM for overburden. The amount of nickel reserves in Front 8 of Meranti Pit based on the design pit limit is 234,142 tons with an average nickel grade of 1.66%, an average iron grade of 26.44%, and an average cobalt grade of 0.08%. The results of the calculation of reserves are shown in Table 9.

**Table 9.** Reserve calculation results at Front 8 of Meranti Pit.

| Category | Volume (BCM) | Tonnage (Ton) | Ni Grade Average | Fe Grade Average | Co Grade Average |
|---|---|---|---|---|---|
| LGO | 55,313 | 82,969 | 1.39% | 33.91% | 0.11% |
| MGO | 32,188 | 48,282 | 1.60% | 25.75% | 0.08% |
| HGO | 68,594 | 102,891 | 1.92% | 20.74% | 0.05% |
| Total | 156,094 | 234,142 | 1.66% | 26.44% | 0.08% |

Each grade of nickel ore has a different tonnage, which are LGO with an average nickel grade of 1.39% at 82,969 tons, MGO with an average nickel grade of 1.60% at 48,282 tons, and HGO with an average nickel grade of 1.92% of 102,891 tons. The amount of production obtained based on mine recovery of 85% is 199,021 tons. Based on the production target applied by the company of 50,000 tons/month, the life of the Front 8 of Meranti Pit mine is 3.98 months. The results of the calculation of overburden are shown in Table 10.

**Table 10.** Overburden calculation results at Front 8 of Meranti Pit.

| Variable | Value |
|---|---|
| Volume (BCM) | 389,063 |
| Tonnage (Ton) | 622,500 |
| Ni average (%) | 0.68 |
| Fe average (%) | 35.20 |
| Co average (%) | 0.12 |

The amount of overburden that must be removed at the Front 8 of Meranti Pit based on the pit limit design is 389,063 BCM with an uneconomical average nickel grade of 0.68%, an average iron grade of 35.20%, and an average cobalt grade of 0.12%. The Stripping Ratio (SR) resulting from this pit limit design is 1.66 BCM/ton. It is known that there is an increase in the stripping ratio by 5% after designing the ultimate pit limit from 0.92 BCM/ton to 1.66 BCM/ton which is influenced by technical factors such as widening of the berm and making ramps when designing the pit limit. Nevertheless, the pit limit design is still feasible and still profitable because the SR value obtained (1.66 BCM/ton) is still smaller than the BESR value (6.32 BCM/ton).

## Conclusions

The ultimate pit limit based on the maximum NPV value after the Whittle scheduling scenario is Pit Shell 9 with ore recovery of 264,375 tons and the resulting NPV of USD 5,557,414 in the best case and USD 5,512,302 in the worst case. Surpac's ultimate pit limit has an NPV of USD 9,840,855. This higher NPV is due to Surpac does not have an input of production parameters per month so that the mine life may be shorter, besides that capital costs are not included in the optimization process. The pit limit design is still economical because it has a stripping ratio value (1.66 BCM/ton) smaller than BESR value (6.32 BCM/ton). Based on the pit limit design that has been made, the total tonnage of laterite nickel ore is 234,142 tons and the overburden volume is 389.063 BCM. The amount of laterite nickel ore production obtained based on mine recovery of 85% is 199,021 tons with a mine life of 3.98 months.

## Acknowledgements

The authors are sincerely thankful and grateful to PT Ang and Fang Brother and Micromine Indonesia for the supports of this research. Thanks also to the editors and reviewers for helps and suggestions to improve this paper.

## Author Contribution

Rifyan Sabaruddin conducted all stages of the research and wrote the paper. Aryanti Virtanti Anas corrected the mine design, the results of pit limit optimization, and revised the paper. Rizki Amalia corrected the calculation of reserves, overburden, and NPV value. Rini Novrianti Sutardjo Tui corrected the resources estimation and BESR value.

## Conflict of Interest

The authors declare no conflict of interest.

## References

Agrawal. (2012). *Modeling of Open Cast Mines Using Surpac and Its Optimization*. Thesis, Department of Mining, National Institute of Technology, India. https://core.ac.uk/download/pdf/53188255.pdf

Araya, A. S., Nehring, M., Vega, E. T., & Miranda, N.S. (2020). The Impact of Equipment Productivity and Pushback Width on the Mine Planning Process. *Journal of the Southern African Institute of Mining and Metallurgy*, 120(10), 599–608. http://www.scielo.org.za/pdf/jsaimm/v120n10/08.pdf

Ares, G., Fernandez, C. C., Alvarez, I. D., Arias, D., & Diaz, A. B. (2022). Open Pit Optimization Using the Floating Cone Method: A New Algorithm. *Minerals*, 12(495), 1–20. https://doi.org/10.3390/min12040495

Aswandi, D., & Yulhendra, D. (2019). Ultimate Pit Design Redesign Using Minescape 4.118 Software in Pit S41 PT. Energi Batu Hitam, Muara Lawa and Siluq Ngurai Districts, West Kutai Regency, East Kalimantan. *Jurnal Bina Tambang*, 4(1), 153–164. http://ejournal.unp.ac.id/index.php/mining/article/view/103474.

Azadi, N., Mirzaei-Nasirabad, H., & Mousavi, A. (2023). Evaluating the efficiency of the genetic algorithm in designing the ultimate pit limit of open-pit mines. *International Journal of Mining and Geo-Engineering*, 57(1), 55–58. https://doi.org/10.22059/ijmge.2022.340973.594963

Butt, C. R. M., & Cluzel, D. (2014). Nickel Laterite Ore Deposits: Weathered Serpentinites Provided for Non-Commercial Research and Education Use. *International Journal of Mineralogy, Geochemistry, and Petrology*, 9(2), 123–128.

https://doi.org/10.2113/gselements.9.2.123

Esmaeil, R., Ehsan, M., Reza, S., & Mehran, G. (2018). Optimized Algorithm in Mine Production Planning, Mined Material Destination, and Ultimate Pit Limit. *Journal of Central South University*, 25, 1475–1488. https://doi.org/10.1007/s11771-018-3841-5

Gusman, M., & Octova, A. (2018). Estimasi Cadangan Insitu Melalui Kegiatan Inpit Drill Activities Pada Bukit Everest, Cherokee, dan Strada di PT Antam (Persero) Tbk UBPN Sultra. *Jurnal Bina Tambang*, 3(2), 722–735. http://ejournal.unp.ac.id/index.php/mining/article/view/10100

Hustrulid, W., Kuchta, M., & Martin, R. (2013). *Open Pit Mine Planning and Design, 3rd Edition.* AA Balkema Publisher, Rotterdam Brookfield. Netherland.

Jodeiri, B., Dehghani, H., & Sadeghi, M. (2021). Ultimate Pit Limit Determination Using Flashlight Algorithm. *International Journal of Mining and Geo-Engineering*, 55(1), 43–48. https://doi.org/10.22059/ijmge.2020.296120.594840

König, U. (2021). Nickel Laterites—Mineralogical Monitoring for Grade Definition and Process Optimization. *Minerals*, 11(11), 1178. https://doi.org/10.3390/min11111178

Maritz, J. H., & Uludag, S. (2019). Developing a mining plan for restarting the operation at Uis mine. *Journal of the Southern African Institute of Mining and Metallurgy*, 119(7), 621–630. http://www.scielo.org.za/pdf/jsaimm/v119n7/06.pdf

Meagher, C., Dimitrakopoulos, R. & Avis, D. (2014). Optimized open pit mine design, pushbacks, and the gap problem—a review. *Journal of Mining Science*, 50(3), 508–526. https://doi.org/10.1134/S1062739114030132

Nwosu, J. I., Ononuju, N. F., & Bassey, M. I. (2022). A Review of Pit Limit of Itakpe Iron Ore Deposit, North Central Nigeria. *International Journal of Scientific Research and Engineering Development*, 5(2), 565–573. http://www.ijsred.com/volume5/issue2/IJSRED-V5I2P65.pdf

PT Ang and Fang Brother. (2019). *Boundary Plan Report of PT Ang and Fang Brother*. Morowali Regency, Central Sulawesi Province.

Qing-hua, G., Chun-ni, B., Fa-ben, L., & Abrand, J. (2014). The Optimization and Application of Cut-off Grades of Multiple Metal Open-pit Mines Based on Equivalent Grade. *Metallurgical and Mining Industry*, 6, 83–91. https://www.metaljournal.com.ua/assets/MMI_2014_6/16-GU-Qing-hua.pdf

Rahmi, F., & Yulhendra, D. (2019). Optimasi Pit Limit Penambangan Mineral Nikel Laterit PT ANTAM Tbk. Unit Bisnis Penambangan Nikel di Site Pomalaa, Sulawesi Tenggara di Front X. *Jurnal Bina Tambang*, 4(3), 295–305. http://ejournal.unp.ac.id/index.php/mining/article/view/105789

Shehu, A., & Lipo, S. (2016). 3D Modeling and Interpretation of Fe/Ni Deposit in Skroska Mine Using Micromine. *Journal of Natural and Technical Sciences*, XX1(1), 49–62. https://www.researchgate.net/publication/328580009

Tivig, D. F., Rotunjanu, I., Florea A., Manu, C. S. (2015). Mining Design Based on A Digital Terrain and Deposit Body Model at Tismana Open Pit. *Annals of the University of Petroşan*i *Mining Engineering*, 16, 5–13.

Whittle, J., & Rozman, L.I. (1991). Open Pit Design in the 90s. *Proceedings Mining Industry Optimisation*

*Conference, The Australian Institute of Mining and Metallurgy, Melbourne*.

Xiao, J., Ding, W., Peng, Y., Chen, T., Zou, K., & Wang, Z. (2020). Extraction of Nickel from Garnierite Laterite Ore Using Roasting and Magnetic Separation with Calcium Chloride and Iron Concentrate. *Minerals*, 10(4), 352. https://doi.org/10.3390/min10040352

Zeyni, E. E., Kakaie, R., & Yousefi, A. (2012). A New Algorithm for Optimum Open Pit Design: Floating Cone Method III. *Journal of Mining & Environment*, 2(2), 118–125. https://www.magiran.com/paper/999017/?lang=en

ISSN: 2579-5821 (Print)
ISSN: 2579-5546 (Online)
URL address: http://journal.unhas.ac.id/index.php/geocelebes
DOI: 10.20956/geocelebes.v7i1.23654

Jurnal Geocelebes Vol. 7 No. 1, April 2023, 77–88

# Identification of Slip Area in Makale Selatan District Using the Geoelectric Method

Bergita Gela M. Saka[1]*, Reni Oktaviani Tarru[2], Enos Lolang[1], Alexander Pakiding[1]

[1]Pendidikan Fisika, Universitas Kristen Indonesia Toraja, Tana Toraja, Indonesia.
[2]Teknik Sipil, Universitas Kristen Indonesia Toraja, Tana Toraja, Indonesia.

*Corresponding author. Email: bergitagelasukumusaka@gmail.com

Manuscript received: 22 October 2023; Received in revised form: 6 February 2023; Accepted: 30 April 2023

**Abstract**

Landslides are most common in steep areas with heavy rainfall. Aside from rainfall, there are numerous other factors that contribute to landslides. The presence of slip fields in the subsurface layer is one of the primary causative factors. South Makale is one of the sub-districts in Tana Toraja Regency that is located in the mountains, where landslides frequently occur, claiming lives. The purpose of this study was to determine the slip area of potential landslides in three sub-districts, which are Sandabilik, Tiromanda, and Randan batu villages. The geoelectric method with the Wenner-Sclumberger configuration type was used. The measurement data is in the form of rock resistivity values, which are then interpreted based on the rock layer type. The findings revealed that the Sandabilik and Randan Batu villages were landslide risk areas. Sandabilik Village has a slip area in the form of lava rock at a depth of 6.5 - 19.8 meters on line 1 and 1.5 - 16 meters on line 2. Rocks of the same type can also be found in Randan Batu Village, a landslide point with depths ranging from 2 to 16 meters on line 1 and 5 to 20 meters on line 2.

**Keywords**: Geoelectric Method; Makale Selatan; Wenner-Sclumberger.

**Citation**: Saka, B.G.M., Tarru, R.O., Lolang, E. and Pakiding, A. (2023). Identification of Slip Area in Makale Selatan District Using the Geoelectric Method. *Jurnal Geocelebes*, 7(1):77-88, doi: 10.20956/geocelebes.v7i1.23654

## Introduction

Landslides cannot be avoided without mitigation measures. Many studies have been conducted on various techniques for estimating an area's vulnerability to potential landslides. Landslide vulnerability is defined as the likelihood of landslides occurring in a specific area in the future, and it can be measured by examining the relationship between certain factors and the distribution of landslides (Yuliana et al., 2017). External causes of landslides, according to Carrión-Mero et al. (2021) and Baldermann et al. (2021), can be classified as weathering (physical, chemical, and biological) and erosion, land subsidence, deposition, vibration, and seismic activity, tephra fall, and water regime changes (Brahmantyo & Yulianto, 2014; Kamur et al., 2020).

Weathering and erosion are heavily influenced by climate. Rainfall, water content (%), and water saturation (Sr, %) are all terms used to describe the climate. The high intensity of rainfall, particularly on steep slopes, is one of the main factors supporting the occurrence of landslides. If the intensity of the rainfall is high, the soil water content will rise, causing the physical condition of the slope body to change. Increased water content weakens the soil's physical-mechanical properties and reduces the slope safety factor (Gusman et al., 2018). Furthermore, landslides are more likely to occur when rocks and slopes are not compacted and easily degraded (Yilmaz & Narman, 2015).

South Makale is one of the sub-districts in Tana Toraja Regency where landslides occur more frequently than in other sub-districts. Landslides in the sub-district buried dozens of houses, cut off the main road, and even resulted in the deaths of landslide victims (Wahyuni et al., 2018). One of the causes of landslides is the presence of a plane that is suspected of being a place for material to move, known as a slip plane (Akmam et al., 2019). Slip plane is also known as the boundary between rock slides and hard rock that serves as a foundation (Zakaria et., 2019).

According to preliminary research, which included creating a map of potential landslide-prone areas in Makale Selatan District, Lembang Randan Batu has a very high potential level of vulnerability, while Tiromanda Village has a low potential level of vulnerability (Saka et al., 2022). In general, an avalanche will move the land/ plane above the sliding plane (Heradian & Arman, 2015; Darsono et al., 2016). The distribution of resistivity values beneath the surface is determined by the rock's ability to conduct electricity. Electric current is the movement of electric charges such as electrons or ions. Ions move in the liquid in the pores of the rock (Sutasoma et al., 2017; Zaenudin & Dani, 2019). It is hoped that the findings of this study will be used to inform mitigation efforts undertaken by the local government and the community in order to reduce losses.

## Materials and Methods

Makale Selatan is one of the Tana Toraja district's sub-districts, with the sub-district capital located in the Tiromanda sub-district. South Makale sub-district is located at 3º06'33" S and 119º49'51" E. The geoelectric method was used to conduct research in three sub-districts: Sandabilik, Tiromanda, and Randan Batu. Randan Batu Village is prone to landslides every year. The Wenner Schlumberger configuration was used in this study. The Wenner Sclumberger configuration's characteristics are not very sensitive to horizontal changes (Ramadhan et al., 2015; Hendri et al., 2020). The current penetration, on the other hand, is quite deep. This configuration is commonly used in a variety of measurements, including slip plane, underground river, and geotechnical measurements (Telford et al., 1990; Maharani et al., 2018). The study location is shown in Figure 2.

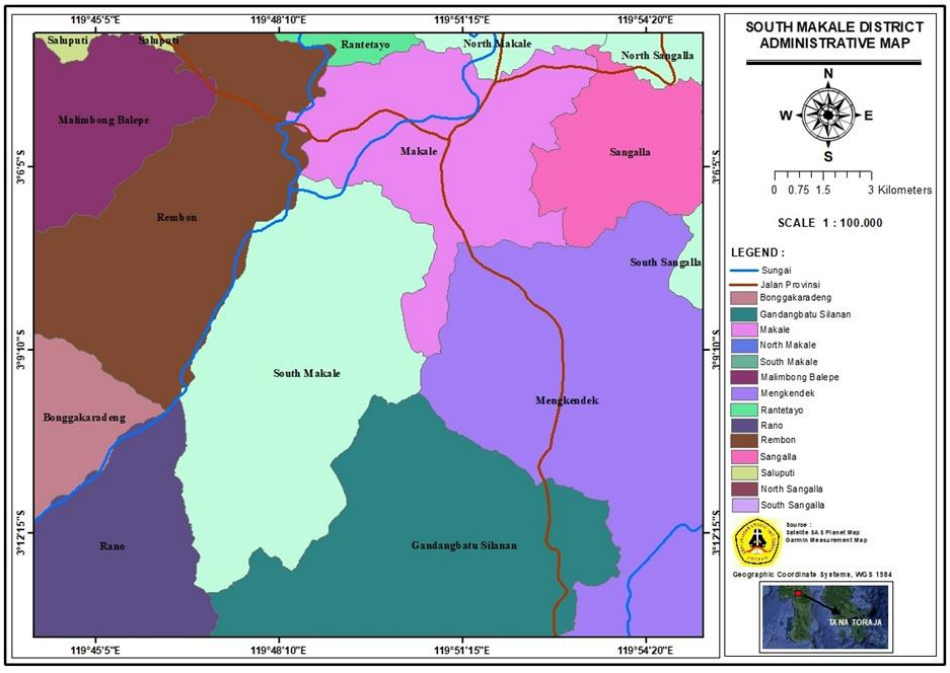


**Figure 1**. Makale Selatan district administrative map.

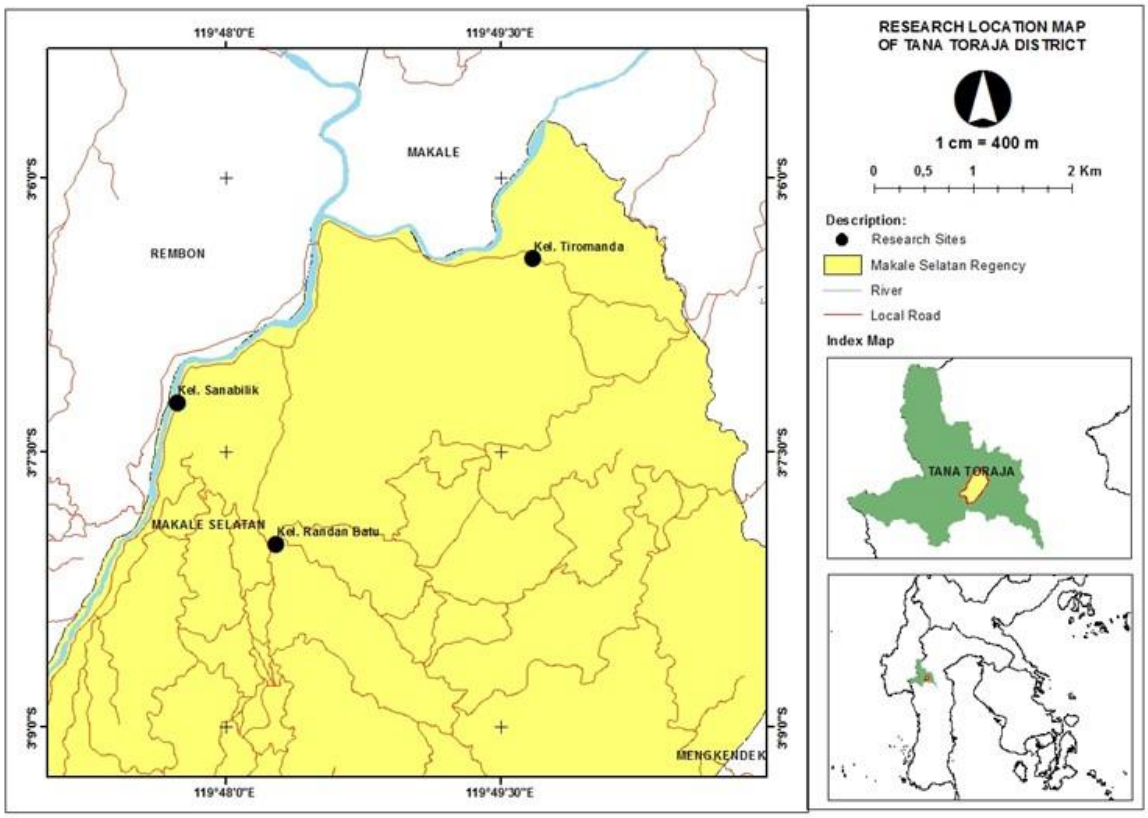


**Figure 2.** Data collection location.

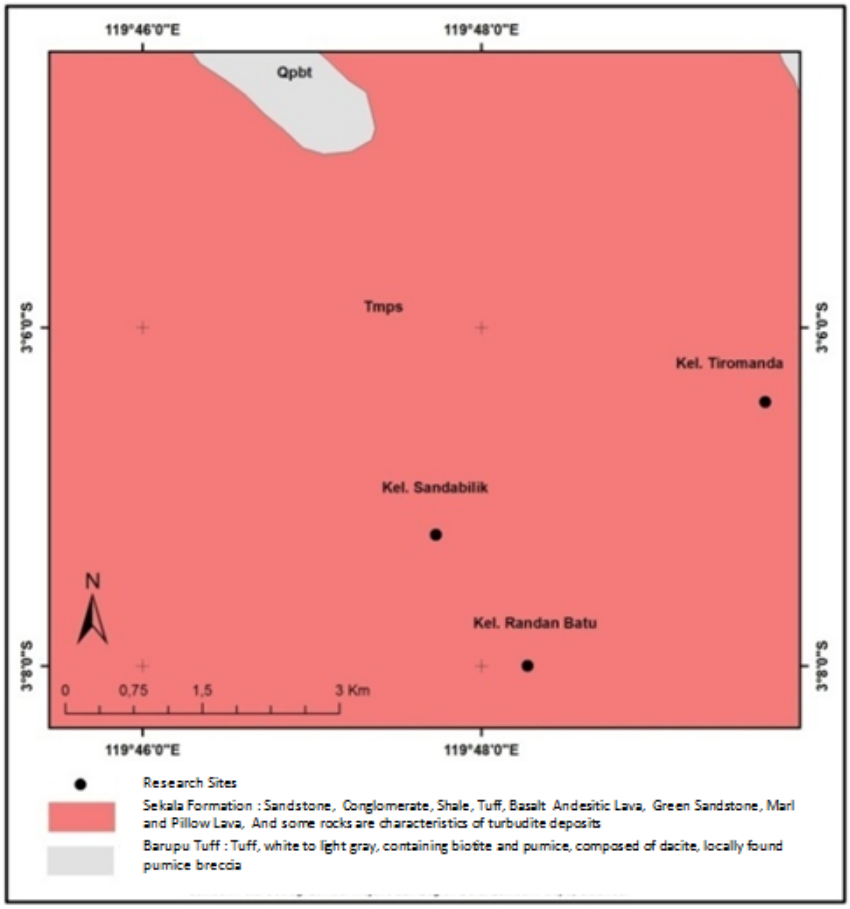


**Figure 3.** Toraja geological formations (modified from Puslitbang Geologi, 1999).

Figure 3 depicts the geological conditions at the study site. The study site is in the Tmps formation unit (Sekala Formation), which contains lithology types such as sandstones, conglomerates, shales, tuffs, and basaltic andesitic lava inserts (Massinai, 2018).

The Barupu Tuff Unit formed independently of the Talaya Volcano Rock Unit and the Latimojong Formation. Tuff, lapilli tuff, and Pleistocene lava breccias make up this unit. Located primarily to the south and east of the study area (Mangala et al., 2017).

The Toraja Formation unconformably overlaps the Latimojong Formation and is unconformably overlain by Lamasi Volcano Rocks (Toml), which are composed of OligoMiocene or Late Oligocene - Early Miocene volcanic rocks, volcanic sediments, and limestones. The Limestone Member (Tomc) of this volcanic rock is aligned with the Riu Formation (Tmr), which is composed of limestone and marl. The Riu Formation is Early Miocene to Middle Miocene in age, and it is unconformably overlain by the Talaya Volcanic Rocks (Tmtv) (Massinai, 2018).

The Schlumberger configuration was used to retrieve geoelectrical resistivity data. This measurement was carried out in Sandabilik Village, Tiromanda Village, and Randan Batu Village, all of which are in the South Makale District of Tana Toraja Regency. A single channel geoelectrical resistivity meter was used in this study. During the geoelectric measurement activities at each research site, two lines with a line length of 75-105 m were taken to obtain a 2D subsurface cross-section.

## Results and Discussion

### *Sandabilik Village*

Figure 4 depicts the results of the measurements taken in Sandabilik Village. The first line coordinates are 3°7'15.50" S and 119°47'43.40" E, while the second one coordinates are 3°7'19.20" S and 119°47'42.50" E.

After measuring and processing geoelectrical data on line 1, the subsurface cross-section has a resistivity value ranging from 1,64 to 714 m .

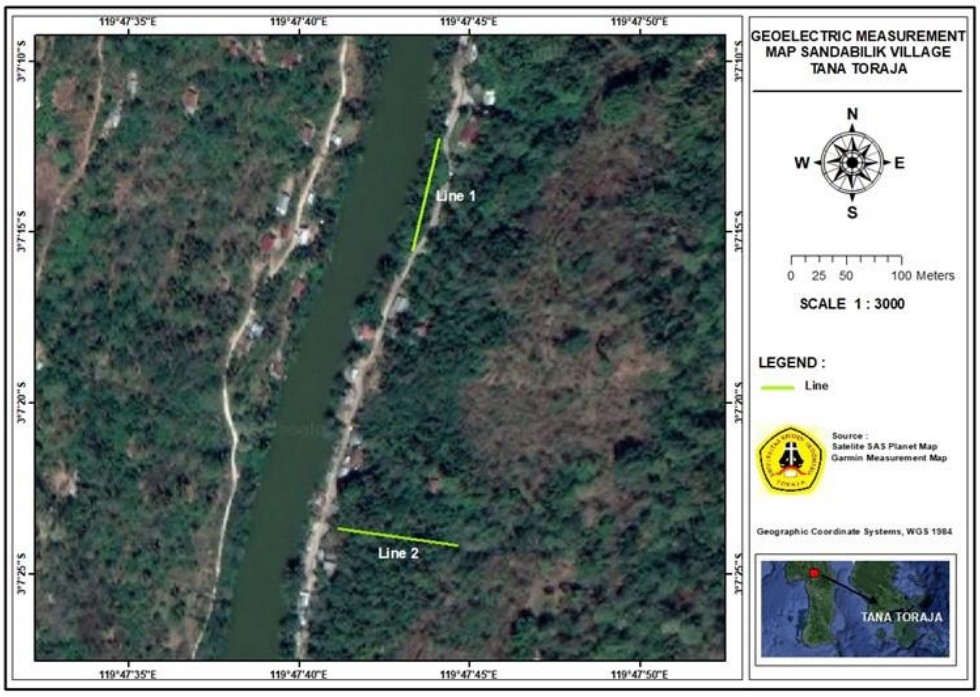


**Figure 4**. Sandabilik Village measurement locations.

**Table 1**. The resistivity values for Line 1 in Sandabilik Village.

| No | Resistivity Value (Ωm) | Depth (m) | Interpretation |
|---|---|---|---|
| 1. | 22.1 – 52.8 | 0 – 20 | Soil |
| 2. | 1.64 – 9.29 | 1.5 – 16 | Water-interspersed soil |
| 3. | 126 – 714 | 6.5 – 19.8 | Lava is a type of compact rock layer |

The resistivity section in Figure 5 is divided into three layers based on the resistivity value, the first of which is a soil layer with a thickness ranging from 0 to 20 m and a resistivity value of 22.1 – 52.8 Ωm. The second layer is a layer of soil that has been saturated with water, resulting in a relatively low resistivity value because water is a good current conductor. The layer with the resistivity value 126 – 714 Ωm can be identified as a compact layer with a lithology type of lava at depths ranging from 6,5 to 19,8 m.

The subsurface section below shows the results of geoelectrical measurements on Line 2 of Sandabilik Village, which has a line length of 75 m:

**Table 2**. The resistivity values for Line 2 in Sandabilik Village.

| No | Resistivity Value (Ωm) | Depth (m) | Interpretation |
|---|---|---|---|
| 1. | 40.4 – 101 | 0 – 16 | The soil layer |
| 2. | 2.55 – 16.1 | 2 – 16 | Water-interspersed soil layer |
| 3. | 254 – 1601 | 1.5 – 16 | Igneous rock layers in the lava |

The second line in Sandabilik village is suspected to have several types of subsurface layers (Figure 6), the first of which has a resistivity value of 40.4 – 101 Ωm and is presumably a soil layer. Soil layers that have a resistivity value of 2.55 – 16.1 Ωm are thought to be saturated with water. Meanwhile, at a resistivity of 254 - 1601 Ωm, the igneous rock layer is thought to be a compact lava layer.

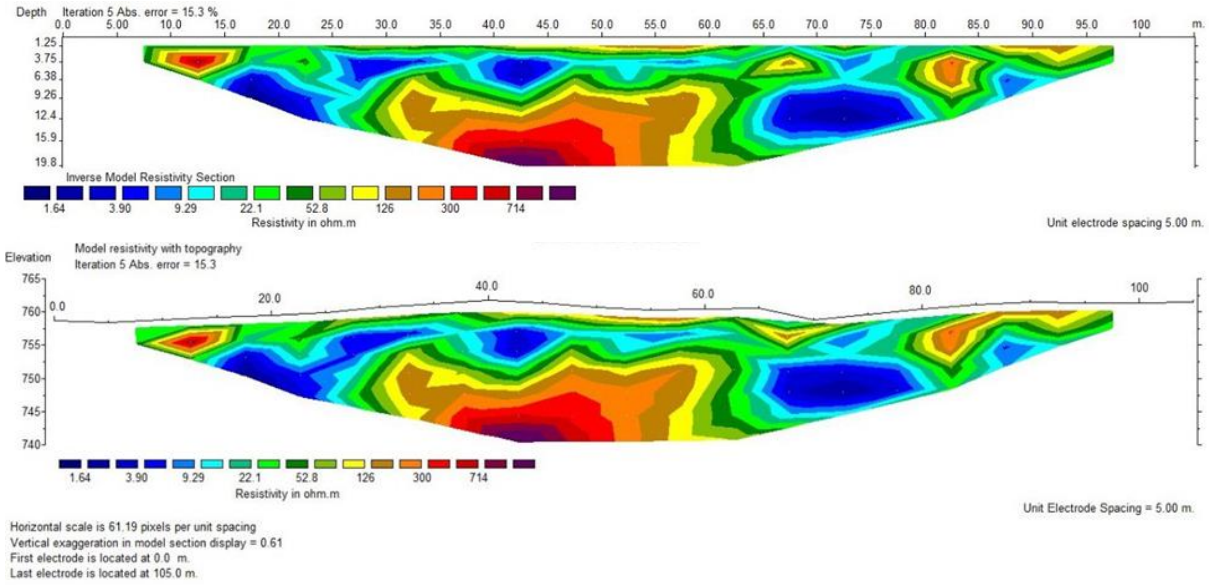


**Figure 5.** (above) Line 1 subsurface cross-section; (below) Line 1 subsurface cross-section with topography in the Sandabilik sub-district.

*Tiromanda Village*

The geoelectric method was used to conduct research in Kel. Tiromanda Kec. Makale Selatan, which is located at coordinates 3°6'26.40" S 119°49'40.60" E, as shown in Figure 7.

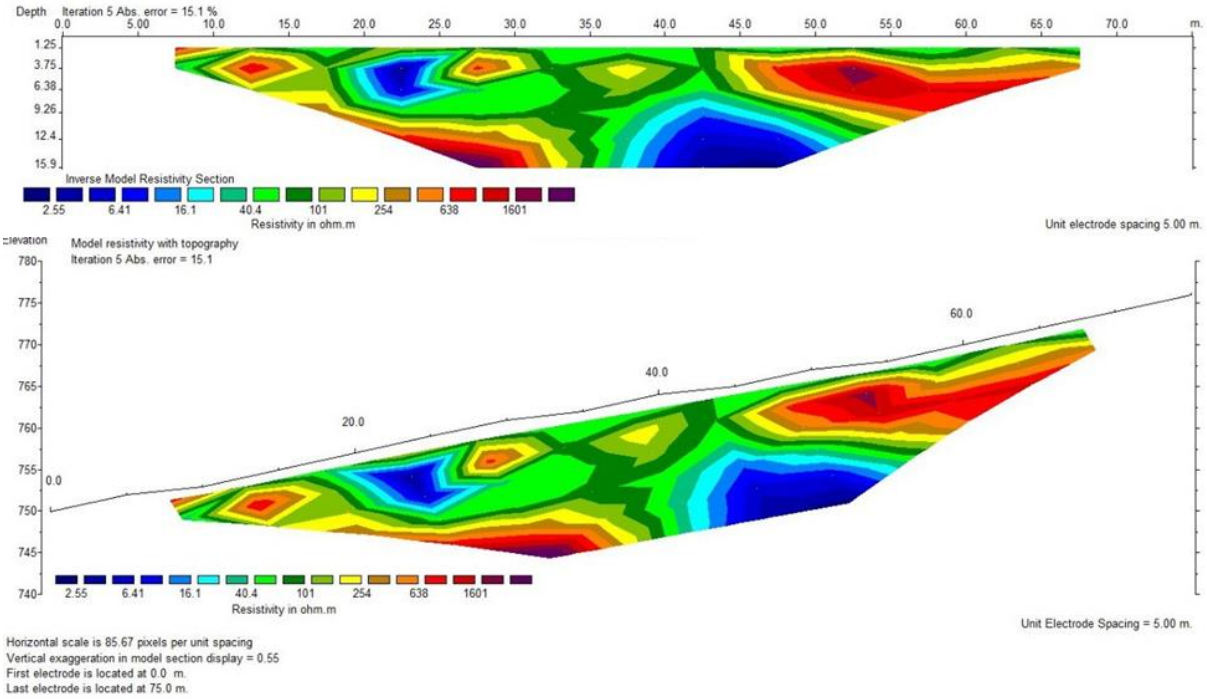


**Figure 6.** (above) Line 2 subsurface cross-section (b) Line 2 subsurface cross-section with topography in Sandabilik Village.

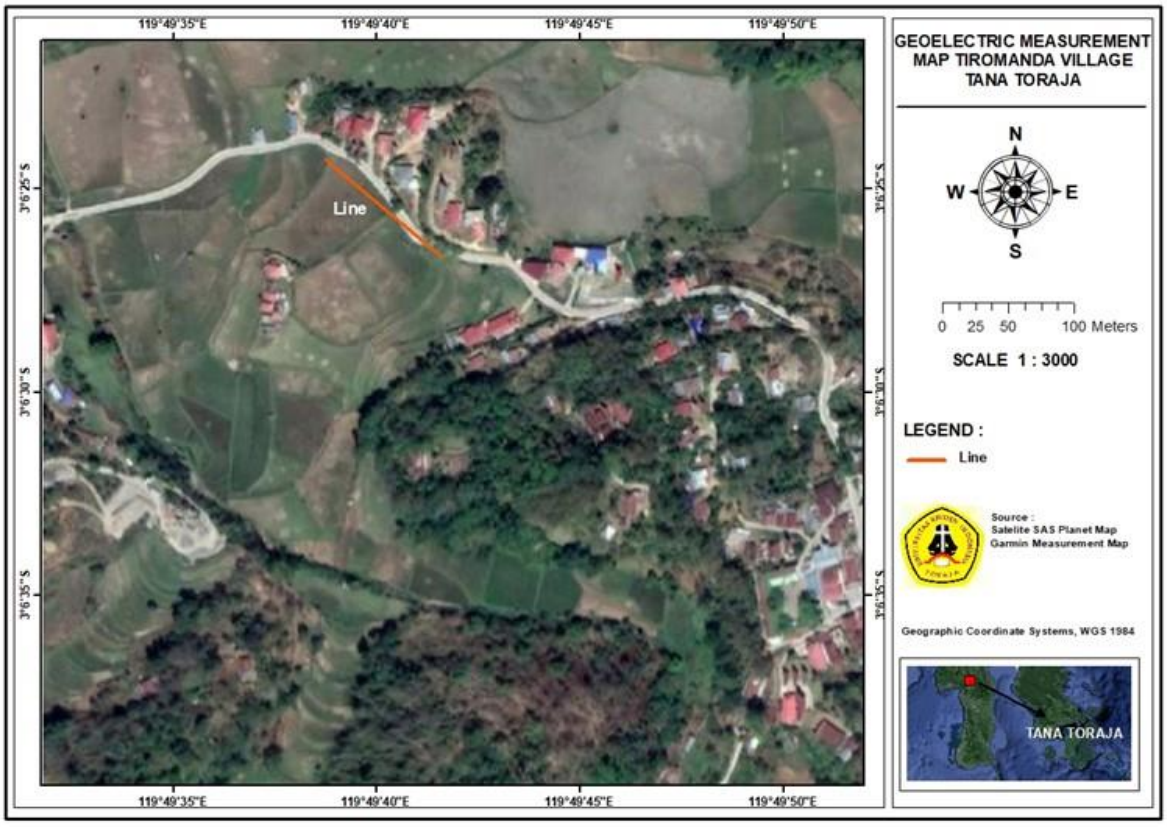


**Figure 7**. Tiromanda Village Measurement Locations.

**Table 3**. The resistivity values for Line 1 in Tiromanda Village.

| No | Resistivity Value (Ωm) | Depth (m) | Interpretation |
|---|---|---|---|
| 1. | 13.8 – 46.8 | 0 – 16 | The soil layer |
| 2. | 0.646 – 7.46 | 3 – 15.9 | A sandstone layer that has been saturated with water |

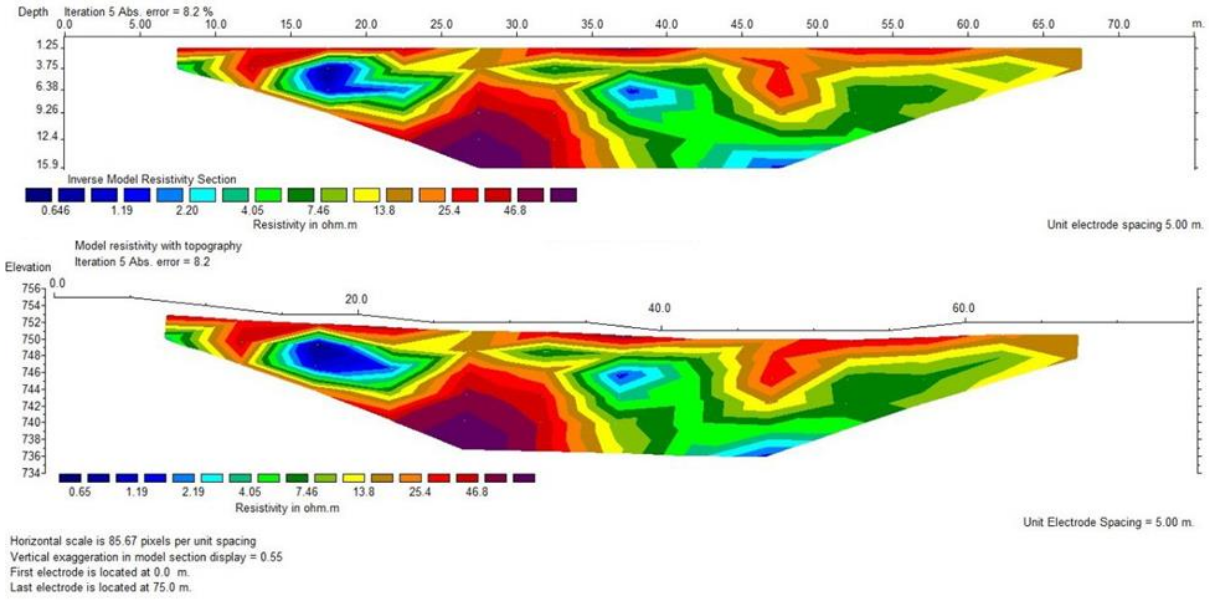


**Figure 8**. (above) Line 1 subsurface cross-section; (below) Line 1 subsurface cross-section with topography in the Tiromanda sub-district.

The results of geoelectric measurement data processing in Tiromanda Village has two layers. There are two types of layers: a soil layer with a resistivity value of 13.8 – 46.8 Ωm at a depth of 0 – 16 m, and a layer with a resistivity value of 0.646 – 7.46 Ωm at a depth of 3 – 15.9 m, which can be assumed to be sedimentary rock as sandstone interspersed with water (Table 3 and Figure 8).

*Randan Batu Village*

The Lembang Randan Batu contains a landslide point. Every year, landslides occur in this valley, killing many people. The coordinates of Line 1 are 3°8'52.90" S 119°48'16.40" E and Line 2's are 3°8'53.70" S 119°48'16.96" E, as shown in Figure 9.

Line 1 has completed a 75-meter-long line. Data processing can be seen at Table 4 and Figure 10. The first is a layer of previously weathered rock soil with a resistivity value of 35 – 21.2 Ωm that is saturated with water at a depth of 0 – 16 m. Layers with resistivity values ranging from 36.7 – 110 Ωm are thought to be at depths ranging from 2 to 16 m.

The depth 20 m is obtained from interpreted as layers of sandstone and lava in the second line measurement with a line length of 105 m (Table 5 and Figure 11). Layers with resistivity values ranging from 6.13 – 969.9 Ωm are thought to be sandstone interspersed with water at depths ranging from 0 to 20 m. Layers 5 – 20 m are interpreted as lava with resistivity values of 193 – 768 Ωm.

**Table 4**. The resistivity values for Line 1 in Randan Batu Village.

| No | Resistivity Value (Ωm) | Depth (m) | Interpretation |
|---|---|---|---|
| 1. | 2.35 – 21.2 | 0 – 16 | Water-saturated soil layer |
| 2. | 36.7 – 110 | 2 – 16 | Lava |

**Table 5**. The resistivity values for Line 2 in Randan Batu Village.

| No | Resistivity Value (Ωm) | Depth (m) | Interpretation |
|---|---|---|---|
| 1. | 6.13 – 96.9 | 0 – 20 | Water-filled sandstone |
| 2. | 193 – 768 | 5 – 20 | Lava |

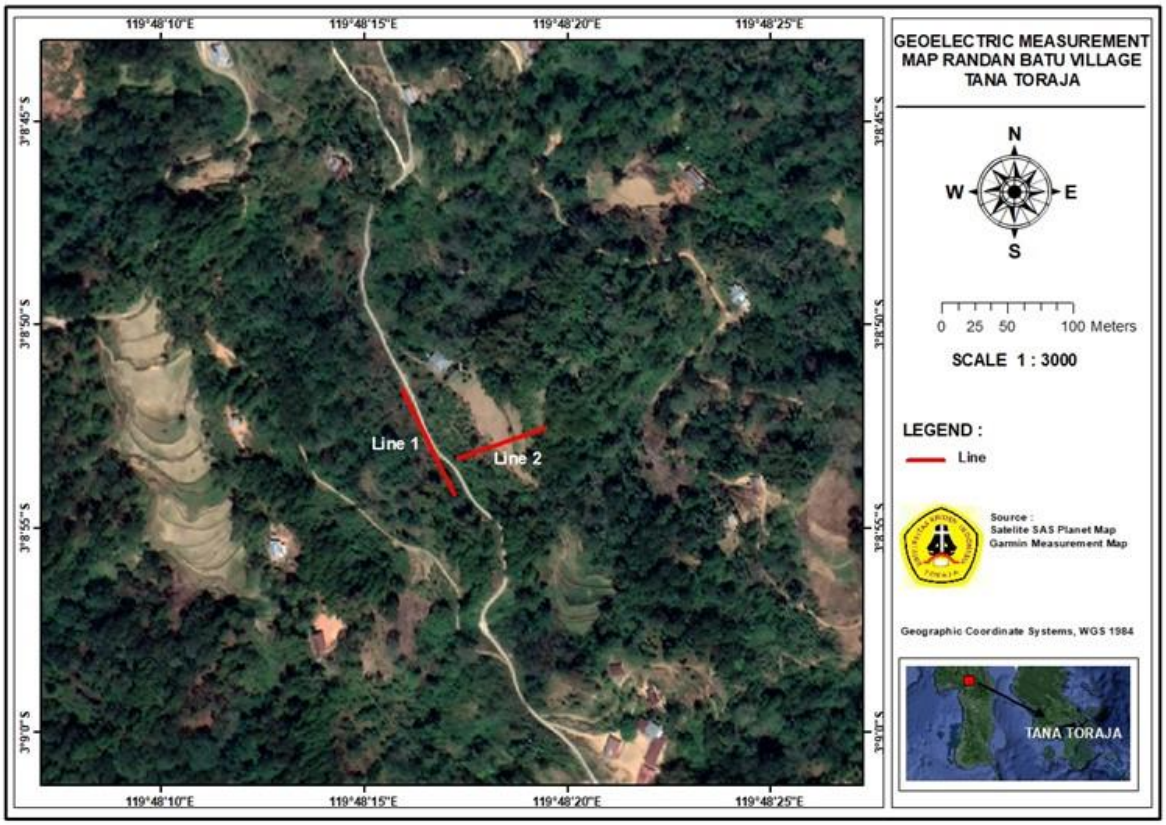


**Figure 9**. Locations of Measurement in Lembang Randan Batu.

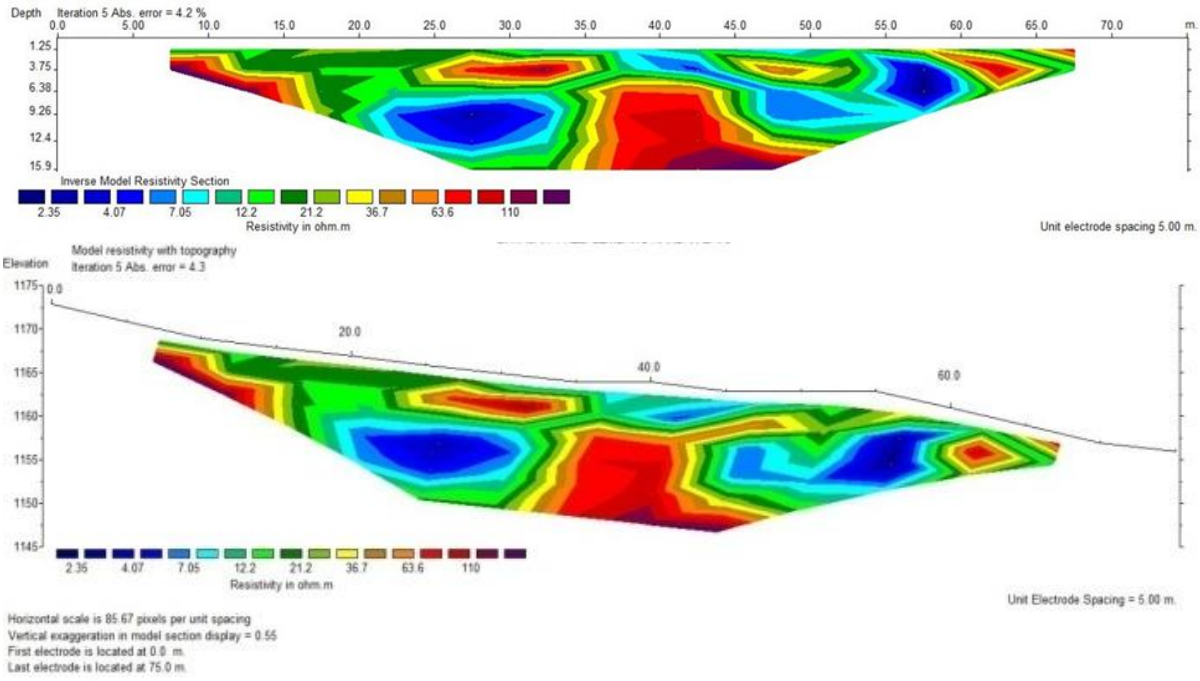


**Figure 10.** (above) Line 1 subsurface resistivity cross-section (below) Line 1 resistivity cross-section with topography at Lembang Randan Batu.

According to the interpretation of the results of geoelectrical measurements, the South Makale District has the potential for landslides. This is evident from measurements taken in the Tiromanda. Lava rocks can be found at depths ranging from 6,5 to 19,8 meters on line 1 and 1,5 to 16 meters on line 2. The same thing can be

found in Lembang Randan Batu, a landslide points with depths ranging from 2 to 16 meters on line 1 and 5 to 20 meters on line 2. Both areas have water-saturated soil above a layer of lava rock.

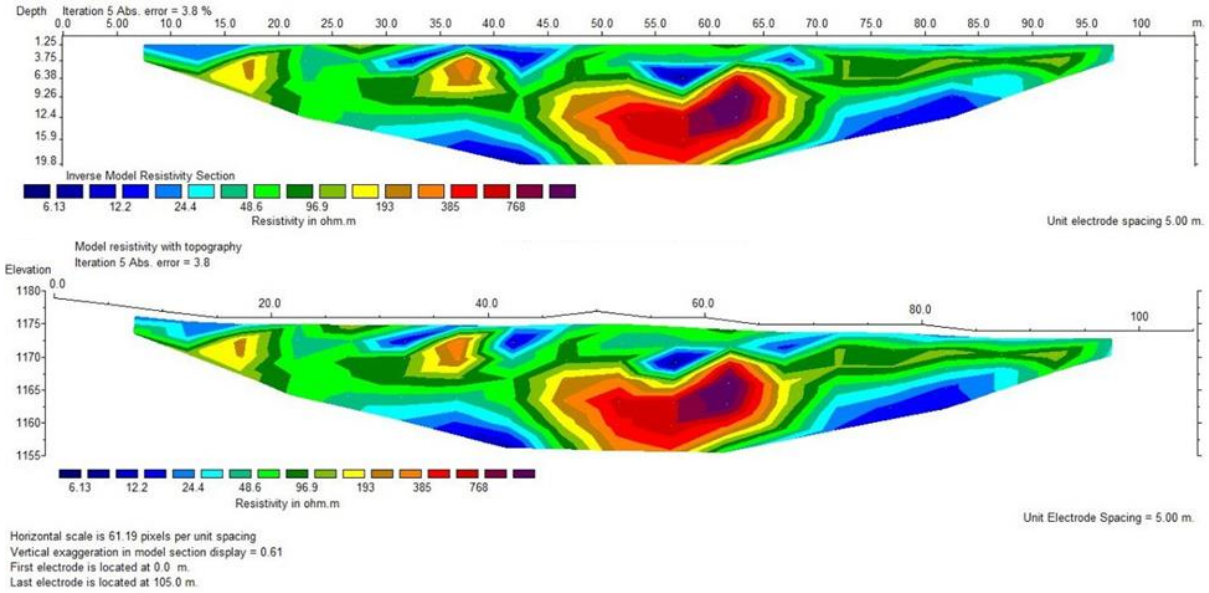


**Figure 11**. (a) Line 2 subsurface resistivity section (b) Line 2 resistivity section with topography at Lembang Randan Batu.

The lithology of the soil layers in the South Makale sub-district is composed of rocks, specifically sandstone, shale, tuff, and basaltic andesitic lava inserts. Tuff and lava layers can be altered to form clay material, which can act as a slip surface for the movement of the soil/ rock mass above it (Nurhayati et al., 2016). Weathering of lava rock can also contribute to mass movement. This movement can take place in either a straight or curved glide plane.

The slip plane is the material's resistivity contrast plane in the unsaturated and saturated zones. The condition of the water contained in the cavity of the media, which is soil or rock, distinguishes the unsaturated zone from the water-saturated zone. When there is no precipitation (the process of rain) in the unsaturated zone, the cavity conditions in the media will be partially filled with air and partially filled with water, but if precipitation occurs, the cavity conditions in the media can become saturated with water due to the infiltration process (absorption of rainwater by land). Meanwhile, whether good water precipitation occurred in the water-saturated zone, media conditions will always be filled (saturated).

Landslide areas are typically associated with low resistivity and high-water content. In this study, the soil is saturated with water, and the slip plane is typically made of a clay material with a higher resistivity (Yatini and Suyanto, 2018). If there is a lot of rain, especially if it is heavy rain, and it lasts for a long time in the two villages, it is likely that water will accumulate in the saturated layers, causing movement if an avalanche occurs. This occurs because rainwater seeping into the soft clay layer causes the material's volume to change, causing the excess material to become more compact.

Due to the force of gravity, the compact material becomes more slippery and serves as the foundation for slipping weathered material in the form of water-saturated clay down the slope.

The high resistivity value on the results of geoelectrical measurements indicates that the potential for landslides in the Sandabilik and Lembang Randan Batu sub-districts is relatively high.

Based on previous research, Tiromanda Village, which is in an area prone to landslides, is also classified as low. Based on the results of potential landslide mapping with the ArcGIS software (Saka et al., 2022). This also supports the findings of geoelectrical measurements, which show that the layer in Tiromanda Village is soil saturated with water at a depth of 3 – 15.9 meters and has no slip plane.

## Conclusion

Based on the results of the two-dimensional interpretation, it is possible to conclude that the two South Makale sub-districts, Sandabilik Sub-District and Randan Batu Sub-District, have the potential for landslide-prone areas. This is supported by measurement results, which show the presence of slip planes in the layers at 6.5 – 19.8 meters on line 1 and 1.5 – 16 meters on line 2 in Sandabilik Village, and at 2 – 16 meters on line 1 and 5 – 20 meters on line 2 in Randan Batu Village.

## Acknowledgements

Thank you to Toraja Christian University of Indonesia for funding research through Independent Research Grants with a Basic Research scheme, as well as the Physics Department of UIN Alauddin Makassar and students from the UKI Toraja Physics Education Study Program who helped collect data.

## Author Contribution

The authors collaborate to conduct surveys, collect data, and analyze geoelectrical measurements.

## Conflict of Interest

The authors declare that they hold no competing interests.

## References

Akmam, A., Amir, H., & Putra, A. (2019). Identifikasi Bidang Gelincir Menggunakan Metoda Geolistrik Tahanan Jenis Daerah Rawan Longsor Di Kota Padang Dan Kabupaten Agam Sumatera Barat. *Talenta Conference Series: Science and Technology (ST)*, 2(2), 152–165. https://doi.org/10.32734/st.v2i2.487

Baldermann, A., Dietzel, M., & Reinprecht, V. Chemical weathering and progressing alteration as possible controlling factors for creeping landslides. *Science of The Total Environment*, 778(146300), 1–13. https://doi.org/10.1016/j.scitotenv.2021.146300

Carrión-Mero, P., Montalván-Burbano, N., Morante-Carballo, F., Quesada-Román, A., & Apolo-Masache, B. (2021). Worldwide Research Trends in Landslide Science. *International journal of environmental research and public health*, 18(18), 9445. https://doi.org/10.3390/ijerph18189445

Darsono, D., Nurlaksito, B., & Legowo, B. (2016). Identifikasi Bidang Gelincir Pemicu Bencana Tanah Longsor dengan Metode Resistivitas 2 Dimensi di Desa Pablengan Kecamatan Matesih Kabupaten Karanganyar. *Indonesian Journal of Applied Physics*, 2(02), 51–60. https://jurnal.uns.ac.id/ijap/article/view/1292/1234

Gusman, M., Nazki, A., & Putra, R. R. (2018). The modelling influence of water content to mechanical parameter of soil in analysis of slope stability. Journal of Physics: Conference Series, 1008(1), 012022. https://doi.org/10.1088/1742-6596/1008/1/012022

Hendri, H., Faryuni, I. D., & Zulfian, Z.

(2020). Identifikasi Bidang Gelincir dan Tipe Tanah Longsor di Daerah Rawan Longsor Desa Bantai Menggunakan Metode Geolistrik. *Prisma Fisika*, 7(3), 167–174. https://doi.org/10.26418/pf.v7i3.36329

Heradian, E. A., & Arman, Y. (2015). Pendugaan Bidang Gelincir di Desa Aruk Kecamatan Sajingan Besar Kabupaten Sambas dengan Menggunakan Metode Tahanan Jenis. *Prisma Fisika*, III(2), 56–61. https://jurnal.untan.ac.id/index.php/jpfu/article/view/11878/11082

Kamur, S., Awal, S., & Iskandar, A. (2020). Identifikasi Bidang Gelincir Zona Rawan Longsor Menggunakan Metode Geolistrik Di Ruas Jalan Toraja – Mamasa. Majalah Geografi Indonesia, 34(2), 101–107. https://doi.org/10.22146/mgi.48262

Maharani, I., Faresi, T. A. Z., Sari, R. S., & Sugiyanto, D. (2018). Identify Landslide Areas Using Resistivity Methods Wenner-Schlumberger Configuration in Meunasah Krueng Kala Area, Aceh Besar. *Journal of Aceh Physics Society*, 7(3), 139–143. https://jurnal.usk.ac.id/JAcPS/article/view/11242

Mangala, A., Yobel, Y., & Alfadli, M. K. (2017). Pemodelan Struktur Geologi Dan Analisis Sumber Panas Menggunakan Metode Gravitasi, Magnetik Dan Fault Fracture Density (FFD) Pada Daerah Panas Bumi Bittuang, Sulawesi Selatan. *Proceeding Seminar Nasional Kebumian Ke-10*, 1566–1578. https://repository.ugm.ac.id/274243/

Massinai, M. A. (2018). Tektonik dan Pengaruhnya Terhadap Potensi Bencana Kebumian di Wilayah Tana Toraja. *Neutrino Jurnal Pendidikan Fisika*, 1(2), 25–31. https://journals.ukitoraja.ac.id/index.php/neo/article/view/488

Nurhayati, N., & Ardi, N. D. (2016). Identifikasi Zona Bidang Gelincir Daerah Rawan Longsor Cihideung Kabupaten Bandung Barat dengan Menggunakan Metode Resistivitas Konfigurasi Wenner. *PROSIDING SNIPS 2016*, 581–589.

Puslitbang Geologi (1999). *Peta Seismotektonik Daerah Tana Toraja dan sekitarnya. Sulawesi*. ESDM. https://geologi.esdm.go.id/geomap/pages/preview/peta-seismotektonik-daerah-tana-toraja-dan-sekitarnya-sulawesi

Ramadhan, B. T., Rahayu, D. A., Rahmawati, T., Riswandha, Y., Firdaus, M. F., Suprapto, D. J., & Danusaputro, H. (2015). Identification of landslide with resistivity method Wenner-Schlumberger configuration at Bendanduwur Semarang as the first step of landslide disaster mitigation. *Padjadjaran Earth Dialogue: International Symposium on Geophysical Issues*, 8–10.

Saka, B. G. M., Jefriyanto, W., Lolang, E., & Tarru, R. O. (2022). Pemetaan Daerah Potensi Rawan Longsor Kecamatan Makale Selatan Kabupaten Tana Toraja. *Neutrino Jurnal Pendidikan Fisika,* 5(1), 11–14. https://ukitoraja.ac.id/journals/index.php/neo/article/view/1511

Sutasoma, M., Susilo, A., & Suryo, E. A. (2017). Penyelidikan Zona Longsor dengan Metode Resistivitas dan Analisis Stabilitas Lereng untuk Mitigasi Bencana Tanah Longsor. *Indonesian Journal of Applied Physics*, 7(1), 35–45. https://doi.org/10.13057/ijap.v7i1.8784

Telford, W. M., Telford, W. M., Geldart, L. P., & Sheriff, R. E. (1990). *Applied Geophysics*. Cambridge university press.

Wahyuni, A., Saka, B. G. M., & Rahmaniah, R. (2018). Mitigasi Bencana Geologi (Gempabumi Dan Tanah Longsor Di Kabupaten Toraja Utara Dan Tana Toraja Dalam

Mengurangi Risiko Bencana. *Neutrino Jurnal Pendidikan Fisika*, 1(2), 33–38. https://journals.ukitoraja.ac.id/index.php/neo/article/view/512

Yatini, Y., & Suyanto, I. (2018). Identification of slip surface based on geoelectrical dipole-dipole in the landslides hazardous area of Gedangsari District, Gunungkidul Regency, Province of Daerah Istimewa Yogyakarta, Indonesia. *IOP Conference Series: Earth and Environmental Science*, 212(1), 012013. https://doi.org/10.1088/1755-1315/212/1/012013

Yilmaz, S., & Narman, C. (2015). 2-D electrical resistivity imaging for investigating an active landslide along a ridgeway in Burdur region, southern Turkey. *Arabian Journal of Geosciences*, 8, 3343–3349. https://doi.org/10.1007/s12517-014-1412-0

Yuliana, E., Tryono, F. Y., & Minarto, E. (2017). Aplikasi Metode Geolistrik Tahanan Jenis Untuk Identifikasi Zona Bidang Gelincir Tanah Longsor Studi Kasus Desa Nglajo Kec. Cepu Kab. Blora. *Jurnal Sains Dan Seni ITS*, 6(2), B42–B47. https://doi.org/10.12962/j23373520.v6i2.26083

Zaenudin, A., & Dani, I. (2019). Pemodelan 2D Dan 3D Geolistrik Tomografi Untuk Interpretasi Bidang Gelincir Dan Arah Aliran Air Pada Struktur Bawah Permukaan Rel Kereta Api Di Baturaja, Sumatera Selatan. *Wahana Fisika*, 4(2), 104–110. https://doi.org/10.17509/wafi.v4i2.20327

Zakaria, M. F., & Maisarah, S. M. (2019). Identifikasi Bidang Gelincir Pada Daerah Rawan Longsor Desa Srimartani, Yogyakarta. *Jurnal Geofisika Eksplorasi*, 5(3), 55–63. http://dx.doi.org/10.23960/jge.v5i3.36

ISSN: 2579-5821 (Print)
ISSN: 2579-5546 (Online)
URL address: http://journal.unhas.ac.id/index.php/geocelebes
DOI: 10.20956/geocelebes.v7i1.23302

Jurnal Geocelebes Vol. 7 No. 1, April 2023, 89 – 98

# Investigation of Groundwater Aquifer Using Electrical Resistivity Method Wenner-Schlumberger Array Mattoangin Village, Bantimurung District, Maros Regency

Aswar Syafnur, Haidir Jibran, William Desmond Tonapa*, Ashar Sae, Nur Hidayat Nurdin

Geophysics Department, Hasanuddin University, Makassar, Indonesia.

*Corresponding author. Email: tonapawd19h@student.unhas.ac.id

Manuscript received: 30 September 2022; Received in revised form: 5 April 2023; Accepted: 30 April 2023

**Abstract**

Groundwater as a source of clean water which is very important in fulfilling the needs of humans is considered suitable as the main alternative. Layers investigation of soil that is permeable to water (aquifer) in Mattoangin Village, Bantimurung District, Maros Regency aims to obtain 2D model map of the distribution of groundwater below the surface. The presence of groundwater stored in aquifers can be explored by geophysical methods. The Wenner-Schlumberger array has a good resolution so it is deemed suitable for aquifers. The measurement data was processed using Res2DInv software. The exploration resulted in a 2D cross-sectional model of the subsurface resistivity. Based on the results of measurements and data processing, the groundwater aquifer which has the potential to have resistivity values of 9.73-32.7 Ωm on track 1, resistivity values of 6.24-32 Ωm is on track 2 with a depth of 6 - 10 m and resistivity values of 5.68-33, 6 Ωm on track 3 with a depth of 6 - 8 Ωm.

**Keywords**: Aquifer zone; geo-electrical; resistivity; Wenner-Schlumberger.

**Citation**: Syafnur, A., Jibran, H., Tonapa, W. D., Sae, A. and Nurdin, N.H. (2023). Investigasi Akuifer Air Tanah Menggunakan Metode Geolistrik Tahanan Jenis Konfigurasi Wenner-Schlumberger Desa Mattoangin, Kecamatan Bantimurung, Kabupaten Maros. *Jurnal Geocelebes*, 7(1): 89–98, doi: 10.20956/geocelebes.v7i1.23302

## Introduction

Water is a basic need for every living thing. Water is also needed by humans in fulfilling all aspects of life. Humans need clean water, both for daily needs and for drinking (Fadli et al., 2020). However, fulfilling the need for clean water is experiencing problems in several regions of Indonesia. This is due to climate change which causes abnormal natural phenomena, which is the uncertainty of rainy and dry seasons (Larson et al., 2016).

Maros is a part of the Regency in South Sulawesi in Indonesia where many of the population experience access to clean water when the dry season occurs. Maros Regency has a wellspring system as a cave, with a good water system. This can be seen in the Bantimurung Watershed's establishment, which is a clean water source for the surrounding community. As a source of clean water, this problem does not guarantee that it will always fulfill the needs of the community, moreover, in Maros Regency, there has been a drought which has had an impact on the agricultural sector. The need for groundwater in Bantimurung District can be a solution in the long term (Heryani, 2014).

Even though Maros Regency has a good water system, drought often occurs in several areas. One of them occurred in the Lekopancing River Basin Area. In 2017, the Lekopancing River Dam in Maros Regency experienced a drought. The impact of drought has hampered the supply of clean water to the North and East of the City (Wahdaniyah et al., 2017).

Regionally, the Bantimurung District, Maros Regency is dominated by the Tonasa Formation Limestone rock formations which were deposited in the central area, between Maros and Pangkajene, having a thickness of at least 600 m. That limestone was deposited in a shallow marine environment in the form of a stable shelf with dimensions of at least 80 km wide. The deposition of these limestones requires at least a decrease in exposure rate of 3 cm/1000 years (Arsyad et al., 2020).

Groundwater is water that is in the cavities of the deep layers of the soil. Groundwater can also be said to be water below the ground surface. Groundwater generally comes from rainwater that enters the soil through pore spaces (Rizal, 2021).

Groundwater is stored in geological formations called aquifers in the form of porous materials or rocks with the condition that they can store water and has good permeability (Daniswara et al., 2019). The formation of aquifers and their various characteristics is influenced by several factors such as past geomorphological processes, the depositional environment when the rock was formed, the mineral composition of the aquifer, the process and pattern of groundwater movement, and the time the groundwater was trapped in the rock layers (Maria et al., 2018)

Based on its depth, aquifers are divided into 2, which are shallow aquifers and deep aquifers. Shallow aquifers or what can be called phreatic are near the surface of the earth, with a thickness of about 5 – 25 meters. While the aquifer or called arteries is at a depth of 80 meters (Rizal, 2021).

Nowadays, the characterization of bedrock aquifers and their sustainable exploitation is the key to water security in the near term (González et al., 2021). To be able to determine the existence of water sources, it is necessary to detect the presence of aquifer layers in the area. The aquifer layer in the ground cannot be seen directly. The existence of aquifer layers in different places also has different conditions, both in-depth and thickness. There are places where it is difficult to find aquifer layers but there are also places where it is easy to find aquifer layers (Darsono, 2019).

Generally, the resistivity method is only good for shallow exploration with a maximum depth of around 100 meters. If the layer depth is more than this value, the information obtained is less accurate, this is due to the large stretch with the aim of obtaining a penetration depth above 100 m, and the current flowing will be weaker (Minanda et al., 2021). Hence, this paper briefly discusses the application of the electrical resistivity method based on groundwater exploration.

## Materials and Methods

Resistivity as a geophysical method basically is observing the symptoms of disorders that occur in normal conditions. The current flows into the earth's layer through two current electrodes in this method (Figure 1). By knowing the value of the potential current, the resistivity value can be determined (Nurfalaq et al., 2021). Electrical resistivity methods are often observed using specific electrode arrays to obtain the resistivity images that show the change in electrical resistivity within the subsurface for the evaluation of basement aquifers (Oyeyemi et al., 2022).

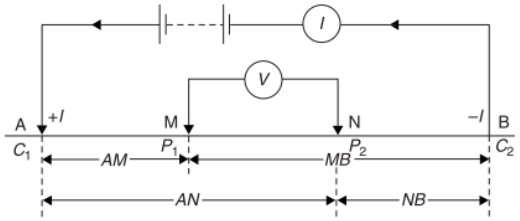


**Figure 1.** Two current electrodes and two potential electrodes on a homogeneous earth surface (Sunarya et al., 2017).

The geophysical problem is an inversion problem that can estimate model parameters based on observational data.

Problems that can be solved by the inversion method can be represented quantitatively by a physical or mathematical approach. The process of estimating the model and model parameters is based on the data observed on the surface (Miftahurrosyada et al., 2022).

Resistivity is a characteristic of the rock that shows the ability of the rock to conduct electric current (Figure 2). This resistivity value can be determined by connecting the battery with an Ammeter and a current electrode to measure the amount of current flowing into the ground (Jamaluddin & Umar, 2018).

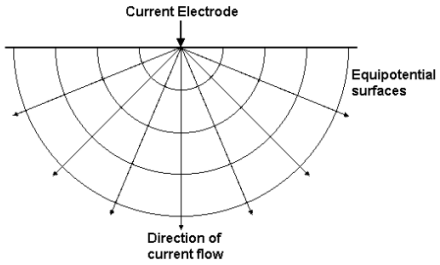


**Figure 2.** Simplified current flow lines and equipotential from a single current source (Jamaluddin & Umar, 2018).

The application of resistivity method is capable of mapping both low and high resistive formations, and therefore it is a valuable tool for vulnerability studies. With the geometry factor (Jamaluddin & Umar, 2018):

$$k = \pi n(n+1)a \quad (1)$$

The resistivity data obtained from measurements is the apparent resistivity data. Apparent resistivity data are generally displayed as colored contour maps and interpreted qualitatively (Andriani et al., 2016). The apparent resistivity can be expressed in the form:

$$\rho_a = K\frac{\Delta V}{I} \quad (2)$$

$$K = \frac{2\pi}{\left(\frac{1}{r_1}-\frac{1}{r_2}\right)-\left(\frac{1}{r_3}-\frac{1}{r_4}\right)} \quad (3)$$

description:
$\rho$ = Apparent Resistivity (Ωm)
$a$ = Electrode Spacing (m)
I = Electric Current (A)
$\Delta V$ = Potential Difference (V)

Where K is geometric factor which is the amount of correction for the location of the two potential electrodes to the location of two current electrodes. The geometric factor depends on the configuration of the current and potential electrodes (Darisma et al., 2020). Geometry values and factors will follow the distribution pattern of the electrodes (Flaño et al., 2018).

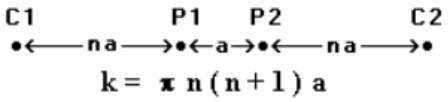


**Figure 3.** The Setting of Wenner-Schlumberger Array (Jamaluddin & Umar, 2018).

Various arrays are frequently used in the resistivity method. One of them is the Wenner–Schlumberger array (Figure 3). The Wenner–Schlumberger Array is a modification and combination of Wenner and Schlumberger Arrays. Wenner-Schlumberger Array can read data vertically and horizontally better than Wenner Array. Wenner-Schlumberger has good data readability due to how the datum density of this array works. This can be seen from how the datum shape of the array. Datum has maximum data density so that the identified geological model has high accuracy (Bery., 2014).

The research location and resistivity data acquisition are in the Mattoanging Village area, Maros Regency, South Sulawesi Sulawesi (Figure 4). Measurements were observed on 3 tracks with each length of 150 meters with 5 meters of electrodes.

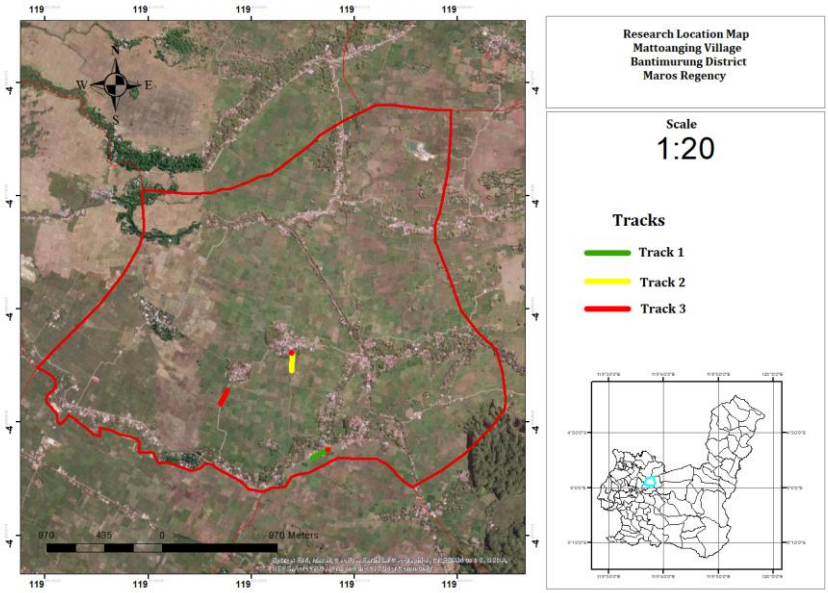


**Figure 4.** Research Location Map and Data Acquisition (Google Earth, 2022 & BIG, 2022)..

The tools used in this study were a set of Geomative Multi-Channel geoelectric tools, electrodes (stainless steel), cables, meter rolls, geological hammers, GPS (Global Positioning System), batteries, compasses, field safety tools, and software such as Res2DInv, Surfer, Google EarthPro, and Microsoft Excel.

Subsurface resistivity modeling was carried out using the inversion finite difference method for each path to obtain a cross-section of the electrical resistivity layering model of the subsurface soil or rock layer. The condition of water saturation is based on the cross-sections obtained in each layer, so that the condition of subsurface groundwater along the measurement path can be identified. (Bakri, 2015).

In obtaining the apparent resistivity value, data processing is carried out by entering current, voltage, and geometry factor values into Microsoft Excel. The data is combined with topographical data and the format is adjusted in a Notepad file so that it can be processed in Res2DInv software with the least square inversion tool to obtain a resistivity cross-section.

So, the scale on resistivity value and the value of apparent resistivity is entered into Golden Surfer software and will get a display of lithology data.

**Table 1**. Rock resistivity values (Sunarya et al., 2017).

| Material | Resistivity (Ωm) |
|---|---|
| Natural Waters | 0.5 – 150 |
| Clays | 1 – 100 |
| Sand | 1 – 1000 |
| Andesite | 100 – 200 |
| Alluvium | 10 – 800 |
| Breccias | 75 – 200 |
| Gravel | 100 – 600 |
| Sandstone | 200 – 8000 |
| Limestone | 50 – ($1 \times 10^7$) |
| Granite | $5 \times 10^3$ – $10^6$ |
| Basalt | $10^3$ – $10^6$ |
| Slate | $6 \times 10^2$ – $4 \times 10^7$ |
| Sandstones | 8 – $4 \times 10^3$ |
| Shale | 20 – $2 \times 10^3$ |
| Limestones | 5 – $4 \times 10^2$ |
| Vulcanic Tuff | 20 – 100 |
| Lavas | 100 – $5 \times 10^4$ |
| Conglomerates | $6 \times 10^3$ – $2 \times 10^4$ |

The iteration process is carried out 5 times iteration. Iteration is aimed to reduce the RMS error data value. The results obtained are in the form of a resistivity section below the 2D surface. By providing a reference to the resistivity values of rock types as in

Table 1, it will be known what is contained in the subsurface layer of the soil.

In determining the estimated layer, there are reliable references, which is the Indonesian National Standard (SNI) 2818 of 2012, regarding the Schlumberger measurement of groundwater and SNI 2528 of 2012 regarding the measurement of Wenner groundwater. SNI 2818 and SNI 2528 attach area conditions, water types, and types of sediment layers based on the measured resistivity scale (Table 2–4).

**Table 2.** Land detention with resistivity scale (SNI, 2012).

| Land detention | Resistivity (Ωm) |
|---|---|
| Wet Area | 50 – 200 |
| Dry Area | 100 – 500 |
| Very Dry Are | 200 - 1000 |

**Table 3.** Water type with resistivity scale (SNI, 2012)

| Water type | Resistivity (Ωm) |
|---|---|
| Ground Water | 1 – 100 |
| Rainwater | 30 – 1000 |
| Sea Water | < 0.2 |
| Ice | 105 - 108 |

**Table 4.** Rock type with resistivity scale (SNI, 2012)

| Rock type | Resistivity (Ωm) |
|---|---|
| Igneous and Metamorphic rocks | 100 - 10000 |
| Consolidated Sediment | 10 – 100 |
| Unconsolidated Sediment | 1 -100 |

## Results and Discussion

Geoelectrical measurements on track 1 are 145 meters long with an electrode spacing of 5 m that is oriented west-east. Using the Wenner-Schlumberger array resulted in 196 data datums. Geoelectrical data inversion on line 1 resulted in a resistivity cross-section as shown in the Figure 5 with an RMS error value of 1.4. the lowest resistivity value is 9.73 Ωm and the largest is 110.01 Ωm.

Based on information from wells around the measurement track, it can be known that the groundwater level is 1 meter, with a layer of sandy loam down to the bottom of the well as deep as 3 meters. From the drilled well it is known that the bedrock is in the form of limestone 6 meters deep.

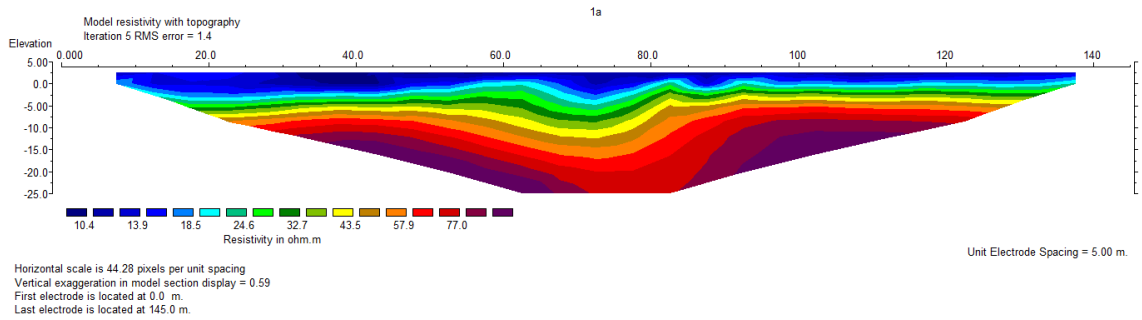


**Figure 5.** Track 1 and Coordinate (791558,9447740).

Based on information from wells data and resistivity cross-sections, it can be concluded that the cross-section of line 1 contains 2 layers, which are (Figure 6):

1. The first layer with a low resistivity value with a resistivity value range of 9.73 – 32.7 Ωm is interpreted as a layer of sandy clay with a thickness varying from 6 – 10 meters. This layer is a shallow aquifer layer.
2. The second layer with a high resistivity value with a resistivity value range of 32.7 – 110 Ωm is interpreted as a layer of limestone up to the end of the data as deep as 30 meters.

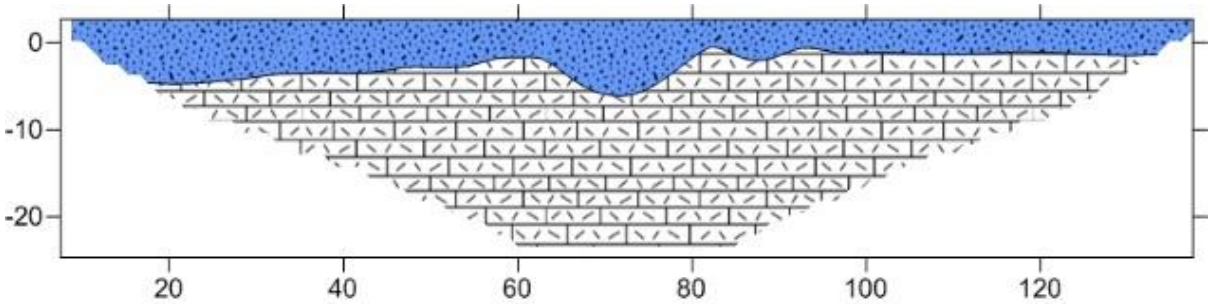


**Figure 6.** Lithology of layer 1.

Geoelectric measurements on track 2 are 145 meters long with 5 m electrode spacing oriented west-east. Using the Wenner-Schlumberger array produces 196 data datums. Geoelectrical data inversion line 2 results in a resistivity cross-section as shown in the Figure 7 with an RMS error value of 2. The lowest resistivity value is 6.24 Ωm and the largest is 566.71 Ωm.

Based on information from wells around the measurement line, it can be known that the groundwater level is 1 meter, with a layer of sandy loam down to the bottom of the well as deep as 3 meters. From the drilled well it is known that the bedrock is in the form of limestone 7 meters deep.

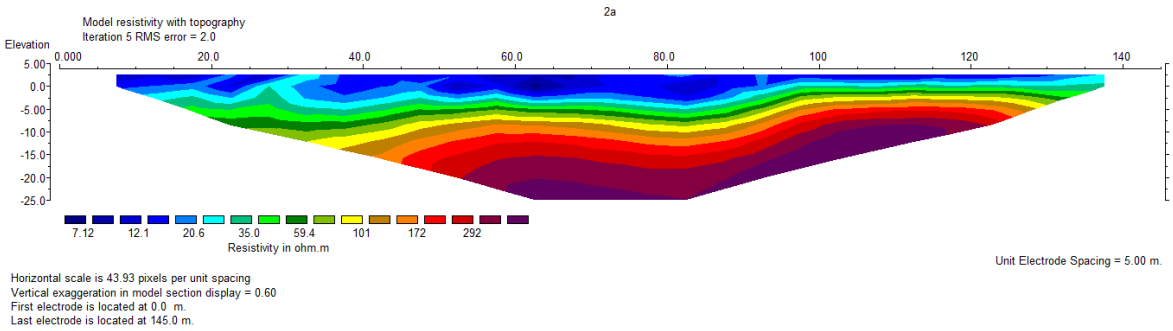


**Figure 7.** Track 2 and Coordinate (791255,9448551).

Based on information from wells data and resistivity cross-sections, it can be concluded that the cross-section of line 2 contains 2 layers, which are (Figure 8):

1. The first layer with a low resistivity. Resistivity value range of 6.24 – 35 Ωm interpreted as a layer of sandy clay with a thickness varies from 6 – 10 meters. This layer is a shallow aquifer layer.
2. The second layer with a high resistivity value with a resistivity value range of 35 – 566.71 Ωm is interpreted as a layer of limestone up to the end of the data as deep as 30 meters.

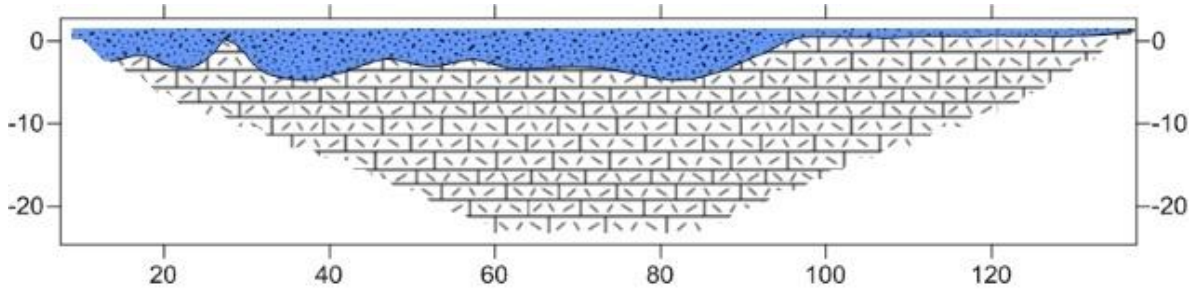


**Figure 8.** Lithology of Layer 2.

Geoelectric measurements on track 3 are 145 meters long with 5 m electrode spacing oriented west-east. Using the Wenner-Schlumberger array produces 196 data datums. Geoelectrical data inversion line 3 results in a resistivity cross-section as

shown in the Figure 9 with an RMS error value of 1.6. The lowest resistivity value is 5.68 Ωm and the largest is 130.75 Ωm.

Based on information from wells around the measurement line, it can be known that the groundwater level is 1 meter, with a layer of sandy loam down to the bottom of the well as deep as 3 meters. From the drilled well it is known that the bedrock is in the form of limestone on 7 meters deep.

Based on information from wells data and resistivity cross-sections, it can be concluded that the cross-section of line 3 contains 2 layers, which are (Figure 10):

1. The first layer with a low resistivity value range 5.68 – 33.6 Ωm interpreted as a layer of sandy clay with a thickness that varies from 6 – 8 meters. This layer is a shallow aquifer layer.
2. The second layer with a high resistivity value with a resistivity value range of 33.6 – 130.75 Ωm is interpreted as a layer of limestone up to the end of the data as deep as 30 meters.

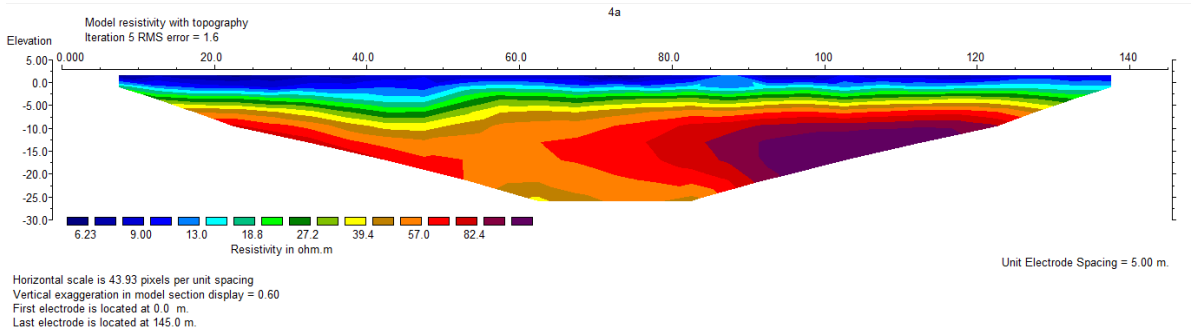


**Figure 9.** Track 3 and Coordinate (790652,9448132).

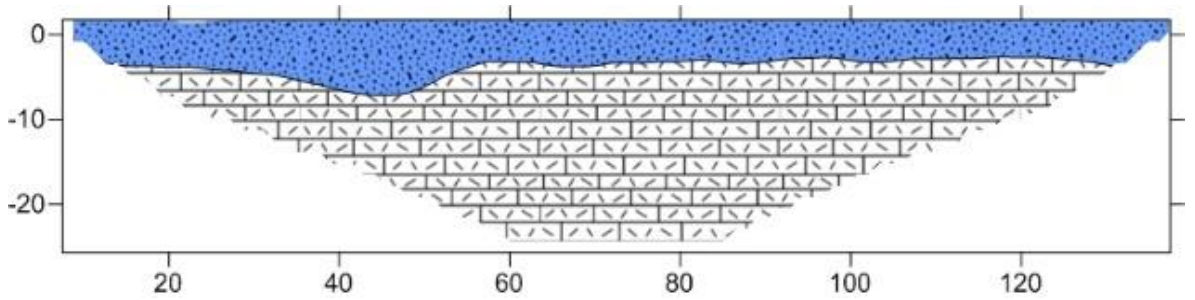


**Figure 10.** Lithology of Layer 3.

## Conclusion

Based on the result study presented, it shows that the application of electrical resistivity method successfully identifies the aquifer as a groundwater source. The information from well data and resistivity cross-sections can be concluded that there are 2 layers in the cross-section of track 3: The first layer shows low resistivity values with range values 5.68 – 33.6 Ωm interpreted as sandy clay with various thicknesses 6 – 8 meters. This is a shallow aquifer. The second layer shows high resistivity with range values 33.6-130.75 Ωm interpreted as a limestone layer to the end of the data limit as deep as 30 meters.

## Acknowledgments

The authors would like to extend sincere gratitude to Geophysics Department, Hasanuddin University, Makassar, Indonesia and as well as an expression of gratitude to the Mattoangin village government, Bantimurung District, Maros Regency for support in making this study successful.

## Author Contribution

Conceptualization, Syafnur, A. and Jibran, H.; methodology, Jibran H. and Sae, A.; software, Nurdin, N.H.; validation, Tonapa, W.D.; format analysis, Syafnur, A. and Sae, A.; investigation, Tonapa, W.D.; data curation, Sae, A.; visualization, Nurdin, N.H.; supervision, Syafnur, A. and Nudin, N.H.; funding acquisition, Syafnur, A. All authors have read and agreed to the published version of the manuscript.

## Conflict of Interest

The authors declare no conflict of interest.

## References

Andriani, F. D., Suwandi, E. A., Dhani, H. S., Firmansyah., Faranie, S. (2016). Pemodelan Kedepan Geolistrik Resistivitas Berdasarkan Metode Beda Hingga (Kasus 2D: Model Lapisan yang Homogen). *Prosiding Seminar Nasional Fisika*, *5*, 73-78. https://doi.org /10.21009/0305020414

Arsyad, M., Ihsan, N., & Tiwow, V. A. (2020). Analysis of mineral sediment characteristics of Bantimurung Bulusaraung National Park in the Karst Maros Region. *Journal of Physics: Conference Series*, 1572(012007), 1–7. https://doi.org/10.1088/1742-6596/1572/1/012007

Bakri, H., Husain, J. R., & Firdaus. (2015). Pendugaan Air Tanah Dengan Metode Geolistrik Tahanan Jenis Di Desa Tellumpanua Kec.Tanete Rilau Kab. Barru Sulawesi-Selatan. *Jurnal Geomine*, 3(1), 165–169. https://doi.org/10.33536/jg.v3i1.19

Bery, A. A. (2014). Depth analysis for sensitivity pattern section in the electrical resistivity using the 2D computerized modeling method. *Electronic Journal of Geotechnical Engineering*, 19, 9389–9400. http://eprints.usm.my/36685/1/Depth_Analysis_19%28Z%29_2014%5B1%5D.pdf

BIG. (2020). Peta Rupa Bumi Indonesia (RBI) dan Peta Kontur. Badan Informasi Geospasial. https://tanahair.indonesia.go.id/portal-web

Darisma, D., Fernanda, F., & Syukri, M. (2020). Investigation of Groundwater Potential using Electrical Resistivity Method and Hydraulic Parameters in Lam Apeng, Aceh Besar, Indonesia. *Journal of Geoscience, Engineering, Environment, and Technology*, 5(4), 185–190. https://doi.org/10.25299/jgeet.2020.5.4.5501

Darsono, D., & Darmanto, D. (2019). Identifikasi Keberadaan Lapisan Akuifer Tertekan (Confined Aquifer) Berdasarkan Data Geolistrik (Studi Kasus: Desa Sambirejo Kecamatan Plupuh Kabupaten Sragen). *Indonesian Journal of Applied Physics*, 9(01), 46–53. https://doi.org/10.13057/ijap.v9i01.30122

Daniswara, A., Dahrin, D., & Setianingsih, S. (2019). Analysis and Modelling of Geoelectric Data Modeling for The Identication of Groundwater Aquifer at Cisarua Area, West Bandung. *Jurnal Geofisika*, 17(2), 22–25. http://dx.doi.org/10.36435/jgf.v17i2.416.

Fadli, A. I., Yuwanto, S. H., & Bahar, H. (2020). Hidrogeologi dan Kualitas Air Tanah Desa Sumber Banteng, Kecamatan Kejayan, Kabupaten Pasuruan, Jawa Timur. *Jurnal Sumberdaya Bumi Berkelanjutan (SEMITAN)*, 2(1), 367–379. http://ejurnal.itats.ac.id/semitan/article/view/1030

Flaño, O., Ayesta, I., Izquierdo, B., Sánchez, J. A., & Ramos, J. M. (2018). Experimental study on the influence of electrode geometry and electrode path on wear pattern in EDM. *Procedia*

*CIRP*, 68, 405–410. https://doi.org/10.1016/j.procir.2017.12.103

González, J. A. M., Comte, J. C., Legchenko, A., Ofterdinger, U., & Healy, D. (2021). Quantification of groundwater storage heterogeneity in weathered/fractured basement rock aquifers using electrical resistivity tomography: Sensitivity and uncertainty associated with petrophysical modelling. *Journal of Hydrology*, 593, 125637. https://doi.org/10.1016/j.jhydrol.2020.125637

Google Earth. (2022). *Explore, Search and Discover*. http://www.earthgoogle.com.

Heryani, N. (2014). Penilaian kesesuaian pembangunan dam parit bertingkat untuk antisipasi kekeringan: studi kasus di Kecamatan Cenrana, Kabupaten Maros, Provinsi Sulawesi Selatan. *Jurnal Sumber Daya Air*, 10(2), 113–124. https://jurnalsda.pusair-pu.go.id/index.php/JSDA/article/view/129

Jamaluddin, & Umar, E. P. (2018). Identification of subsurface layer with Wenner-Schlumberger arrays configuration geoelectrical method. *IOP Conference Series: Earth and Environmental Science*, 118(012006), 1–7. https://doi.org/10.1088/1755-1315/118/1/012006

Larson, S., Kirono, D. G. C., Tjandraatmadja, G., & Barkey, R. (2016). Monitoring and evaluation approaches in water resources project design: experiences from an urban water system climate change adaptation project in Indonesia. *Water Policy*, 18(3), 708–726. https://doi.org/10.2166/wp.2015.144

Maria, R., Rusydi, A. F., Lestiana, H., & Wibawa, S. (2018). Hidrogeologi Dan Potensi Cadangan Airtanah Di Dataran Rendah Indramayu. *Jurnal Riset Geologi dan Pertambangan*, 28(2), 181–192. https://jrisetgeotam.lipi.go.id/index.php/jrisgeotam/article/view/803

Miftahurrosyada., Zakiyyah, A. R., Salsabiila, F., Putrianti, R. A., Wibowo, R. C., & Zaenudin, A. (2022). The Effectiveness of Using the Damped Least Squares Inversion Method on the Schlumberger Configuration Curve in Determining Underground Structures. *Jurnal Ilmu Fisika dan Pembelajarannya (JIFP)*, 6(1), 28–33. https://doi.org/10.19109/jifp.v6i1.10624

Minanda, A., & Ardi, N. D., & Waslaluddin (2021). Uji Sensitivitas Metode Geolistrik Resistivitas Konfigurasi Wenner Alpha Pada Model Silinder. *Prosiding Seminar Nasional Fisika*, 1(1), 385–389. http://proceedings.upi.edu/index.php/sinafi/article/view/1862

Nurfalaq, A., Jumardi, A., Manrulu, R. H., Nawir, A., & Umar, E. M. (2021). Geoelectric Sounding for Identification of Aquifer Layer in East Turatea Village South Sulawesi Province. *Journal of Physics: Conference Series*, 1940(012028), 1–11. https://doi.org/10.1088/1742-6596/1940/1/012028

Oyeyemi, K. D., Aizebeokhai, A. P., Metwaly, M., Omobulejo, O., Sanuade, O. A., & Okon, E. E. (2022). Assessing the suitable electrical resistivity arrays for characterization of basement aquifers using numerical modeling. *Heliyon*, 8(5), e09427. https://doi.org/10.1016/j.heliyon.2022.e09427

Rizal, N. S. (2021) *Teknik Pendugaan & Eksploitasi Air Tanah*. LPPM Unmuh Jember.

SNI. (2012). *SNI 2528:2012 Tata cara pengukuran geolistrik Wenner untuk eksplorasi air tanah*. Badan Standarisasi Nasional.

SNI. (2012) *SNI2818:2012 Tata cara pengukuran geolistrik Schlumberger*

*untuk eksplorasi air tanah*. Badan Standarisasi Nasional.

Sunarya, W., Hasanuddin, H., Syamsuddin, S., Maria, M., & Syamsuddin, E. (2017). Identifikasi Bijih Besi (Fe) Menggunakan Metoda Geolistrik Resistivitas Konfigurasi Wenner-Schlumberger di Kabupaten Luwu. *Jurnal Geocelebes*, 1(2), 72–81. https://doi.org/10.20956/geocelebes.v1i2.2793

Wahdaniyah, N., Kartini, K., Rahayu, I. P., Asman, A. I., & Annisa, D. N. (2017). Mitigasi Bencana Kekeringan di Kawasan Daerah Aliran Sungai Maros Kabupaten Maros Provinsi Sulawesi Selatan. *Seminar Nasional Geomatika*, 2, 361–370.


**Indexing and Abstracting**

# GEOFISIKA
UNIVERSITAS HASANUDDIN

ISSN 2579-5546